FACULTY
OF MATHEMATICS
AND PHYSICS
Charles University

DOCTORAL THESIS

Mariia Zimina

Microstructure and mechanical properties of lightweight structural AZ31 alloy prepared by twin-roll casting method

Department of Physics of Materials

Supervisor of the doctoral thesis:	doc. RNDr. Miroslav Cieslar, CSc.
Study programme:	Physics
Study branch:	Physics of Condensed Matter and Material Research

Prague 2016

First of all, I would like to dedicate this work to my supervisor Miroslav Cieslar without whom it would not be possible neither to start to work on this subject nor to finish this work. Many thanks go to him and his family for invaluable patience and help.

I would like also to acknowledge Stefan Zaunschrimt from the University of Applied Science Upper Austria for the very innovative approach and providing of X-ray computed tomography studies of the segregation.

Many thanks go to Dr. Anna Zimina from Karlsruhe Institute of Technology, my dear sister, for being always a scientific and personal example and for providing X-ray diffraction measurements for this study.

All colleagues from Charles University in Prague for their help, professionalism and a lot of nice lunches, dinners, evenings and mornings spent together trying to find the truth and make this World better and materials lighter. Specially, I would like to thank Petr Harcuba for practical hours of microscopy, Peter Minárik for the nice classes of AFM, Marta Čepová and Jana Kalalová for their help in learning basic laboratory skills and sample preparation. Special thanks go to Pavel Zháňal for his patience and love, to Michaela Šlapáková for her extraordinary responsiveness and will to help, to Michal Knapek for his department-famous skills and to Michail Paukov for his friendship all these years.

...also to my dear family and friends from Russia, Czech Republic and all over the World for a support and being happy for me and with me. And last but not the least I would like to thank my floorball family without which this work would never be done and which made my life in Czech Republic so colorful.

I declare that I carried out this doctoral thesis independently, and only with the cited sources, literature and other professional sources.

I understand that my work relates to the rights and obligations under the Act No. 121/2000 Coll., the Copyright Act, as amended, in particular the fact that the Charles University in Prague has the right to conclude a license agreement on the use of this work as a school work pursuant to Section 60 paragraph 1 of the Copyright Act.

In .... date .... Mgr. Mariia Zimina

"Exactly!" said Deep Thought. "So once you do know what the question actually is, you'll know what the answer means."

- Douglas Adams, The Hitchhiker's Guide to the Galaxy

Název práce: Mikrostruktura a vlastnosti lehké slitiny AZ31 připravené plynulým odléváním mezi válce

Autor: Mariia Zimina

Katedra: Katedra Fyziky Materiálů

Vedoucí disertační práce: doc. RNDr. Miroslav Cieslar, CSc., KFM

Abstrakt: Mikrostruktura hořčíkové slitiny AZ31 připravené metodou plynulého odlévání mezi válce byla studována pomocí světelné a elektronové mikroskopie a mikroskopie atomárních sil a byl testován vliv zvýšené teploty na výslednou mikrostrukturu materiálu. Mechanické vlastnosti byly zkoumány měřením mikrotvrdosti a tahovými zkouškami při relativně nízké rychlosti deformace 10^{-3} s^{-1}. Výsledky ukazují, že tažnost studovaného materiálu roste s rostoucí teplotou deformace, avšak v okolí 200 °C se tažnost plynule odlévaného materiálu značně snížila. Tento efekt byl pozorován i u konvenčně odlitého materiálu a je pravděpodobně způsoben změnou deformačního mechanismu indikovaného při této teplotě. Dále byly studovány změny mikrostruktury a mechanických vlastností způsobené intenzivní plastickou deformací. Materiál byl deformován metodou pravoúhlého protlačování rovnostrannými kanály, což vedlo ke značnému zjemnění velikosti zrn a zvýraznění počáteční bazální textury, která je však při následném žíhání téměř zcela potlačena. Poprvé byla také úspěšně použita metoda lisování asymetrickou rýhovanou matricí na stejné slitině. Výsledkem bylo opět zjemnění velikosti zrn, výrazný nárůst mikrotvrdosti oproti původnímu stavu a také zesílení bazální textury, kterou však následným žíháním nelze odstranit. Výslekdy dále ukázaly, že finální vlastnosti materiálu po intenzivní deformaci jsou významně ovlivněny předdeformací vloženou do materiálu již při plynulém odlévání.

Klíčová slova: hořčíková slitina; twin-roll casting; intenzivní deformace

Title: Microstructure and mechanical properties of lightweight structural AZ31 alloy prepared by twin-roll casting method

Author: Mariia Zimina

Department: Department of Physics of Materials

Supervisor: doc. RNDr. Miroslav Cieslar, CSc., KFM

Abstract: Microstructure of AZ31 twin-roll cast magnesium alloy was studied using light optical, electron and atomic force microscopy. The effect of annealing temperature on the microstructure was tested. Mechanical properties of a thin magnesium strip were investigated by means of microhardness tests and tensile tests at a relatively low strain rate 10^{-3} s^{-1}. Results show that the ductility of the twin roll cast strip increases with increasing deformation temperature, however, a remarkable decrease was observed at about 200 °C. This effect appears also in a conventionally cast ingot of a master alloy and is caused by a change of a deformation mode occurring at this temperature. Moreover, the effect of severe plastic deformation on the microstructure and mechanical properties was studied. Equal channel angular pressing was applied on magnesium strip samples and lead to a significant grain refinement accompanied by an unfavorable strengthening of the initial basal texture, which is effectively suppressed by a subsequent annealing. A constrained groove pressing was for the first time successfully applied on AZ31 twin-roll cast strip leading to an increase of microhardness and grain refinement. Also this technique strengthens the basal texture, which, however persists even after subsequent annealing. The results also showed that an initial microstructure and a predeformation imposed into samples during casting remarkably influences their final properties after intensive plastic deformation.

Keywords: magnesium alloy; twin-roll casting; severe plastic deformation.

Contents

Introduction **3**

1 Magnesium and magnesium alloys **5**
- 1.1 Crystallographic structure . . . 5
- 1.2 Designation of magnesium alloys . . . 6
- 1.3 Microstructure and mechanical properties . . . 7
  - 1.3.1 Effect of alloying elements . . . 7
  - 1.3.2 Effect of grain size . . . 11
  - 1.3.3 Effect of dendrite arm spacing . . . 11
  - 1.3.4 Effect of segregation and porosity . . . 12
  - 1.3.5 Effect of texture . . . 13
- 1.4 Strengthening mechanism of metals and plastic deformation . . . 15
  - 1.4.1 Grain boundary strengthening . . . 16
  - 1.4.2 Precipitation strengthening . . . 17
  - 1.4.3 Solid solution strengthening . . . 18
  - 1.4.4 Deformation strengthening . . . 18
- 1.5 Heat treatment . . . 19
- 1.6 Dynamic recrystallization . . . 19
- 1.7 Casting of magnesium alloys . . . 20
  - 1.7.1 Twin-roll casting . . . 21
- 1.8 Equal-Channel Angular Pressing . . . 21
- 1.9 Constrained Groove Pressing . . . 23

2 Aims of the study **25**

3 Experimental part **26**
- 3.1 Materials preparation . . . 26
- 3.2 Heat treatment . . . 26
- 3.3 Electrical resistivity measurements . . . 27
- 3.4 Microstructural characterization . . . 28
  - 3.4.1 Light optical microscopy . . . 28
  - 3.4.2 Scanning electron microscopy . . . 29
- 3.5 Atomic force microscopy . . . 31
- 3.6 X-ray diffraction . . . 32
- 3.7 X-ray computed tomography . . . 32
- 3.8 Mechanical properties characterization . . . 34
  - 3.8.1 Microhardness measurements . . . 34
  - 3.8.2 Tensile tests . . . 35
- 3.9 Thermo-mechanical processing . . . 35
  - 3.9.1 Equal-Channel Angular Pressing . . . 35
  - 3.9.2 Constrained Groove Pressing . . . 36

4 Results 38
4.1 As-cast materials 38
4.1.1 Light optical microscopy 38
4.1.2 Scanning electron microscopy 40
4.1.3 X-ray microtomography 42
4.1.4 Electron back scatter diffraction 43
4.1.5 Microhardness testing 45
4.2 Annealed materials 45
4.2.1 Electrical resistivity 45
4.2.2 Light optical microscopy 46
4.2.3 Scanning electron microscopy 52
4.2.4 Electron back scatter diffraction 53
4.2.5 X-ray diffraction 53
4.2.6 Microhardness testing 54
4.2.7 Tensile tests 57
4.2.8 Additional measurements 60
4.3 Severe plastic deformation 67
4.3.1 Equal channel angular pressing 67
4.3.2 Constrained groove pressing 76

5 Discussion 85

Conclusion 99

Bibliography 101

List of Figures 115

List of Tables 120

List of Abbreviations 121

Introduction

In 1618 one English farmer at a city of Epsom wanted to give his cows water from a well. They refused to drink it because of the taste of water. The farmer also noticed that this water had some useful properties and healed scratches and rashes. Later it was found that it was magnesium sulfate ($MgSO_4$), which was soluted in the water. In 1755 magnesium was recognized as an element by Black. Later in 1808 it was isolated by Sir H. Davy. He electrolysed a mixture of magnesia (magnesium oxide, MgO) and mercuric oxide (HgO). Davy's first suggestion for a name was "magnium" but the name "magnesium" is now used instead. This name is derived from the Greek word "Magnesia", a district of Thessaly. The Epsom salt is still used today to treat minor skin abrasions [1]. The most significant application of magnesium is a use as a component of aluminium alloys used mainly for beverage cans, sports equipment such as components for golf-clubs, fishing reels, archery bows and arrows, bicycles etc. Alloyed with zinc magnesium is used in die-casting for a production of sheets used in photoengraving plates in the printing industry, dry-cell battery walls, and roofing [2]. It is also used to remove sulfur in the production of iron and steel [3] and as a precursor in the production of titanium in the Kroll process [4]. Due to the flammability and high burning temperature (3100 °C) magnesium is good as a starting emergency fire and pyrotechnics firework sparklers and is also used in a flash photography. There are some more application of pure magnesium:

- In the form of turnings or ribbons in organic synthesis.
- As a reducing agent for the production of uranium and other metals from their salts.
- As a galvanic anode to protect underground tanks, pipelines and water heaters.

Nowadays, magnesium is the third most commonly used structural metal, following iron and aluminium. It is the lightest structural metal in the periodic table of elements with an atomic number twelve. Magnesium is a non-toxic metal and has a density of 1.738 $g{\cdot}cm^{-3}$, which is about five times lower than for steel and about one and a half times less than for aluminium, and thus makes magnesium competitive with steels and aluminium alloys. The melting point is 650 °C. Due to the low weight and several unique properties such as high specific strength and stiffness, high dimensional stability and good thermal and electrical conductivities magnesium alloys can be used for a wide variety of commercial applications [5, 6]. Automotive, aerospace, sports and computer industries where the weight reduction is critical [7–9] are main areas of magnesium alloys utilizations. Moreover, Mg-based alloys are used as materials for reversible hydrogen storage in the form of metallic hydrides [10]. An earlier Mercedes-Benz 300 SLR race car had a body made from a magnesium alloy called Elektron. In 1955 these cars ran at Le Mans, the Mille Miglia and other world-class race events. Porsche used magnesium alloy frames in the famous 917/053 model that won Le Mans in 1971 and still holds the absolute distance record. Volkswagen Group and Porsche have used magnesium in their engine components for many years. BMW 325i and

330i models were featured by a high-temperature magnesium alloy AJ62A engine blocks compounds in 2006. Together with AE44 both these alloys are recent developments in high-temperature low creep magnesium alloys [2]. Mitsubishi Motors also uses magnesium (branded magnesium alloy) for paddle shifters. A general strategy for such alloys is to form intermetallic precipitates at grain boundaries, for example by adding mischmetal or calcium [11]. Magnesium alloys are widely used for manufacturing of mobile phones, laptops, cameras and other electronic components. Electron alloy was one of the main aerospace construction metal used by Germany in World War I and later for German aircrafts in World War II. A use of magnesium alloys in the aerospace industry is increasing, mostly driven by an increasing importance of a fuel economy and a need to reduce weight [12].

In order to achieve a material with required mechanical properties application of appropriate casting and further thermomechanical treatment are necessary. The microstructure and local mechanical properties of an original ingot of a master AZ31 alloy and a strip continuously cast from these ingots by twin-roll casting (TRC) were established and compared in the present study. However, the deformation imposed into the material during casting and rolling usually leads to the formation of a strong basal texture with c-axis parallel to the materials surface. It can limit a ductility as well as other mechanical properties [13–15].
On the other hand, grain refinement leads to a significant improvement of mechanical properties, namely, hardness and tensile properties. Therefore, further treatment is needed to weaken or eliminate the original texture. Selected severe plastic deformation (SPD) techniques were used to reduce the grain size and to prepare magnesium alloys appropriate for eventual further industrial applications. For this aim an equal channel angular pressing (ECAP) and constrained groove pressing (CGP) were applied to AZ31 magnesium alloys.
ECAP is a most commonly used SPD techhnique which allows to obtain magnesium alloys with an ultra-fine grained (UFG) structure already after several processing cycles [16]. The CGP technique was primary established for aluminium alloys and appeared to be an effective tool for the grain refinement of thin metal plates and strips. During this process as well as during ECAP the large amount of energy is introduced into the material without any significant dimensional changes. Nevertheless, ECAP is not designed to be used on continuously cast strips and sheets, whereas CGP can be easily used for these aims.

An influence of heat treatment on a texture of the TRC alloy before and after SPD was studied using annealing at temperatures up to 560 °C. A comparison of two SPD methods applied on a magnesium alloy strip was done in this work. Results describe the evolution of microstructure and mechanical properties of as-cast magnesium alloys after the combination of heat treatment and SPD. Changes in a microstructure and mechanical properties were observed using light optical, atomic force and electron microscopy techniques, microhardness testing, measuring of electrical resistivity and tensile/compression tests.

The work was performed with the financial support of the Grant Agency of Czech Republic under the project P107-12-0921.

1. Magnesium and magnesium alloys

1.1 Crystallographic structure

Magnesium has hexagonal close packed (hcp) crystallographic structure, where the only closed-packed plane is the basal plane. For pure magnesium at room temperature (RT), unit cell dimensions are a = 0.32092 nm and c = 0.52105 nm. An axial ratio of c/a = 1.6236 makes it nearly close packed structure [17]. Magnesium deforms plastically by slip and twinning. Figure 1.1 shows possible slip and twinning systems in magnesium. At room temperature (RT) slip can be realized only in basal plains (0001) in the most occupied direction $\langle 11\bar{2}0\rangle$. Secondary slip can occur along the prismatic planes $\{10\bar{1}0\}$ in the same directions as in the basal plane. Twinning occurs on the $\{10\bar{1}2\}$ plane in the $[11\bar{2}0]$ direction just below 225 °C [18]. At higher temperatures pyramidal slip can be activated along $\{11\bar{2}2\}$ planes. The basal $(0001)[2\bar{1}\bar{1}0]$ and prismatic $(01\bar{1}0)[2\bar{1}\bar{1}0]$ slip systems initiate deformations with Burgers vectors $< a >$ perpendicular to the c-axis. Therefore, no plastic strain parallel to the c-axis is produced by those systems. Non-basal slip systems such as $< c + a >$-pyramidal and twinning modes can be activated and accommodate c-axis strains. Generally, a poor ductility of magnesium and magnesium alloys at RT is ascribed to the activation of only basal slip systems. In this case the von Mises criterion for five slip systems required for a grain to undergo an imposed deformation cannot be met. Thus, non-basal slip systems should be activated. It can be achieved by increasing deformation temperatures, formation of materials with fine grain structure [19] or by the addition of alloying elements [20]. It was shown [19] that the activation of non-basal slip systems can significantly improve ductility of magnesium alloys.

Due to their hexagonal structure, magnesium alloys exhibit mechanical properties such as strong anisotropy, which is more pronounced than for construction metals with cubic crystal structure, and tension-compression asymmetry. Deformation mechanisms in hcp metals, dislocation motion on specific slip system and activation of twinning, are not yet fully understood [21].

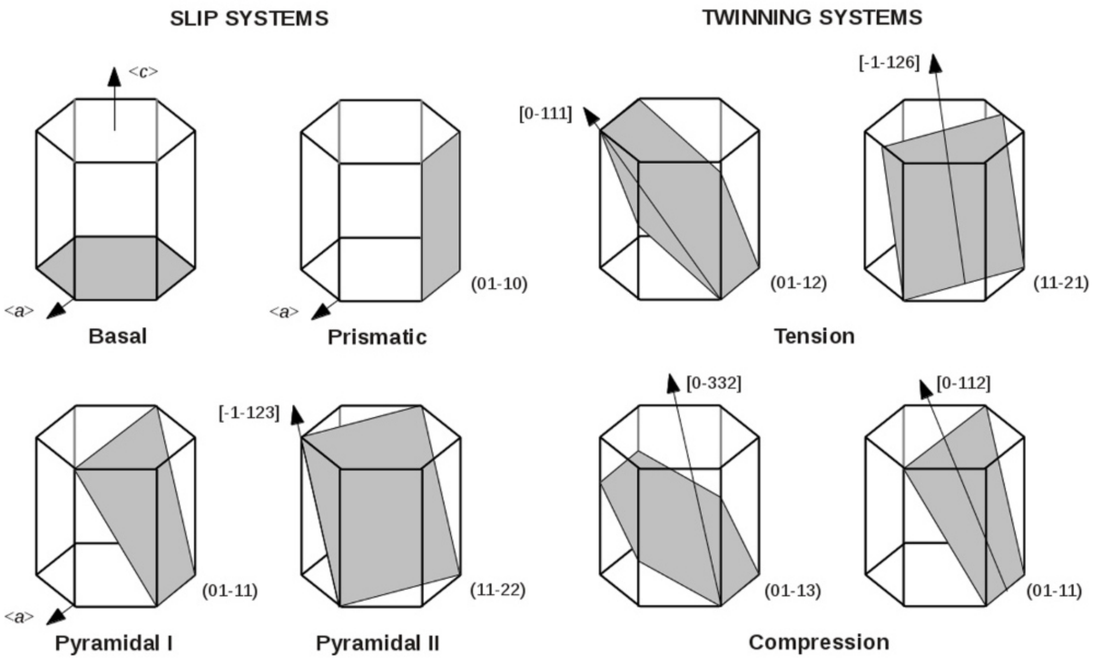

Figure 1.1: Slip and twinning systems in magnesium [22].

1.2 Designation of magnesium alloys

Magnesium alloys are designated by short codes defined by either American Society for Testing and Materials (ASTM) in B275 standard or by European Standard (EN). The first one is used more frequently. The ASTM code includes letters denoting alloying elements and numbers, which stand for approximate chemical compositions in wt.%. Table 1.1 summarizes some of elements in ASTM specification B275. Thus, marking AZ31 represents magnesium alloy with 3 weight percent of aluminium and 1 weight percent of zinc. According to EN the same alloy is marked as $MgAl_3Zn_1$.

Table 1.1: ASTM designation of some alloying elements (RE - rear earth).

ASTM	A	C	E	F	K	L	M	Q	S	T	W	X	Z
Element	Al	Cu	RE	Fe	Zr	Li	Mn	Ag	Si	Sn	Y	Ca	Zn

Since mechanical properties of a majority of magnesium alloys can be changed using heat treatment, different types of characters are used to describe this treatment during fabrication as well as after it. Basic temper designations are listed in Table 1.2.

Table 1.2: Basic heat treatment designation of magnesium alloys [5].

Designation	**Treatment**
F	As-fabricated
O	Annealed, recrystallized (wrought products only)
T2	Annealed (cast products only)
T3	Solution heat treated and cold worked
T4	Solution heat treated
T5	Artificially aged only
T6	Solution heat treated and artificially aged
T7	Solution heat treated and stabilized
T8	Solution heat treated, cold worked and artificially aged
T9	Solution heat treated, artificially aged and cold worked
T10	Artificially aged and cold worked

1.3 Microstructure and mechanical properties

1.3.1 Effect of alloying elements

Magnesium is widely used for many construction applications. However, its low formability is a crucial problem of castings. Therefore, different alloying elements are used to improve formability and other mechanical properties of magnesium. A small addition of zinc, manganese, silicon and rear earth (RE) elements plays an important role in the formation of secondary phases in magnesium alloys and thus influence their mechanical properties [23–26].

Nowadays, popular commercial alloys are based mainly on magnesium - aluminium - zinc system. Table 1.2 shows the nominal chemical composition of commonly used commercial alloys. Among cast Mg alloys, the most usable are AZ91, AZ61 and AZ31. The latter has the highest corrosion resistance [27] and could be also easily recycled [28]. AZ91 is still the most widely used die casting alloy with a good corrosion resistance and a good die castability, but cannot be used at temperatures higher than 120 °C due to a poor creep resistance [29]. Alloys based on Mg-Al-Zn-Mn systems such as AZ91 (contains 0.2 wt.% of manganese) and AM60 (does not contain zinc) are used mainly for RT applications and cannot be used above 150 °C because their strength rapidly decreases at this temperature [30]. Manganese is generally used as a grain refiner for high purity Mg-3,6,9%Al and commercial AZ31 alloy [31]. Added to magnesium it increases the corrosion resistance and also reduces the effect of iron which is always present as an impurity [32, 33].

Zirconium has a significant effect on a grain refinement of magnesium alloys [35]. In EZ33 (3.3 wt.% RE, 2.7 wt.% Zn, 0.6 wt.% Zr) and ZE41 (4.2 wt.% Zn, 1.2 wt.% RE, 0.7 wt.% Zr) magnesium alloys with the zinc addition up to 4 wt.% increases the RT tensile properties without significant affect on properties at elevated temperatures. EZ33 alloy exhibits long-term stable properties at tem-

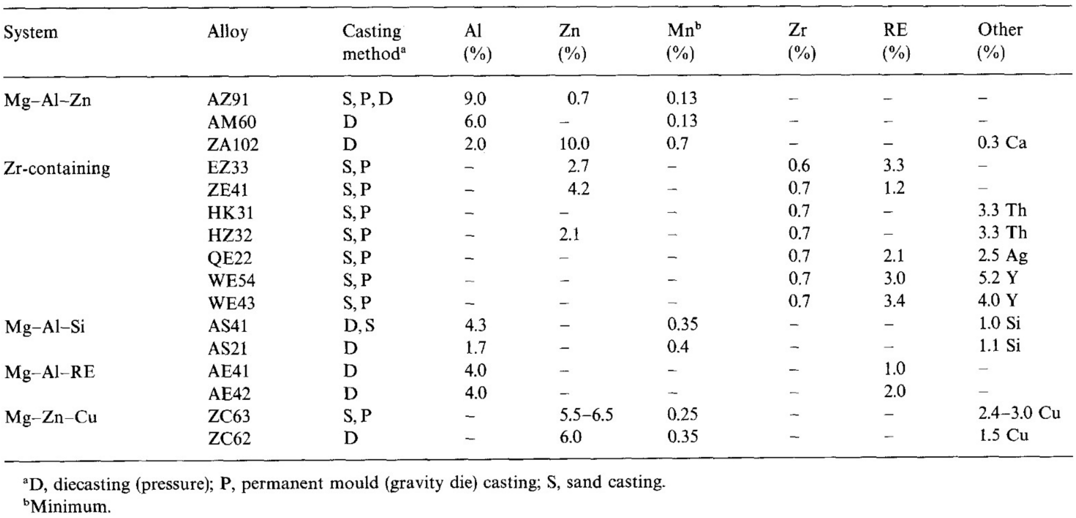

System	Alloy	Casting method[a]	Al (%)	Zn (%)	Mn[b] (%)	Zr (%)	RE (%)	Other (%)
Mg–Al–Zn	AZ91	S, P, D	9.0	0.7	0.13	–	–	–
	AM60	D	6.0	–	0.13	–	–	–
	ZA102	D	2.0	10.0	0.7	–	–	0.3 Ca
Zr-containing	EZ33	S, P	–	2.7	–	0.6	3.3	–
	ZE41	S, P	–	4.2	–	0.7	1.2	–
	HK31	S, P	–	–	–	0.7	–	3.3 Th
	HZ32	S, P	–	2.1	–	0.7	–	3.3 Th
	QE22	S, P	–	–	–	0.7	2.1	2.5 Ag
	WE54	S, P	–	–	–	0.7	3.0	5.2 Y
	WE43	S, P	–	–	–	0.7	3.4	4.0 Y
Mg–Al–Si	AS41	D, S	4.3	–	0.35	–	–	1.0 Si
	AS21	D	1.7	–	0.4	–	–	1.1 Si
Mg–Al–RE	AE41	D	4.0	–	–	–	1.0	–
	AE42	D	4.0	–	–	–	2.0	–
Mg–Zn–Cu	ZC63	S, P	–	5.5–6.5	0.25	–	–	2.4–3.0 Cu
	ZC62	D	–	6.0	0.35	–	–	1.5 Cu

[a] D, diecasting (pressure); P, permanent mould (gravity die) casting; S, sand casting.

[b] Minimum.

Figure 1.2: Nominal chemical composition of certain important cast magnesium alloys [34].

peratures up to 250 °C. Moreover, it can be successfully used for RT applications where a pressure tightness is required [30].

Silicon containing die cast magnesium alloys, such as AS21 (1.7 wt.% Al, 1.1 wt.% Si, 0.4 wt.% Mn) and AS41 (4.3 wt.% Al, 1 wt.% Si, 0.35 wt.% Mn), can be used in automotive applications as reported by Foerster [36]. These alloys contain Mg_2Si intermetallic compound which has high melting temperature, high hardness, low density and low thermal expansion [37, 38]. However, increasing the liquidus temperature can be a disadvantage for casting procedure. It was also shown that AS21 alloy exhibits better creep strength than AS41. However, it is more difficult to cast and it has poor corrosion resistance [36].

Effect of aluminium and zinc

Aluminium can be used as an alloying element for magnesium both for solid solution strengthening and for precipitation hardening in order to improve the yield strength (YS) [5, 30]. On the other hand, the phase diagram in Fig. 1.3a shows that it lowers the melting temperature of Mg-Al alloys. Dahle et al. [39] showed that the addition of aluminium to pure magnesium leads to the formation of a dendrite microstructure instead of a cellular. When the aluminium content reaches 5 wt.% dendrites with pools of an eutectic phase between dendrite arms appear and develop.

According to the Mg-Al equilibrium phase diagram in Fig. 1.3a, the eutectic β-phase ($Mg_{17}Al_{12}$) is formed at 437 °C when the aluminium content reaches approximately 13 wt.%. However, it was shown that the eutectic phase appears already in alloys containing only 2 wt.% Al for non-equilibrium cooling conditions, which are generally present during castings [40].

The β-phase is formed during the cooling of the casting precipitating preferably at grain boundaries [39]. A poor thermal stability of $Mg_{17}Al_{12}$ phase and its discontinuous precipitation can lead to a significant grain boundary sliding at elevated temperatures. Because the aluminium content in regions near grain boundaries increases with increasing temperature, the solidus temperature decreases and creep properties are weakened. It was shown by several authors [41, 42] that higher creep deformations occur at the grain boundaries than inside dendrites. The accelerated diffusion of aluminium in Mg matrix and a self-diffusion of magnesium at elevated temperatures result in a poor creep deformation of magnesium alloys [43].

Zinc forms several stable intermetallics with magnesium as it is shown in Fig. 1.3b. Zinc is used in a majority of conventional magnesium alloys because of an improved corrosion resistance [44] and a strengthening of magnesium using solution hardening mechanism [45]. Strength of Mg-Zn alloys can be increased also by heat treatment. Age-hardening is a mechanism used for cast and wrought alloys to increase stability of these materials. Moreover, it was shown [46] that zinc improves biocompatibility both in vitro and in vivo in Mg-Zn and Mg-Mn-Zn alloys.

Since as-cast Mg alloys contain α-Mg and β-$Mg_{17}Al_{12}$ and formation of new β-$Mg_{17}Al_{12}$ phases during heat treatment requires huge concentration of Al, the Zn/Al ratio increases. An extra β-$Mg_{21}(Zn,Al)_{17}$ phase could be formed at 364 °C if Zn/Al ratio is 0.68-0.99 [47].

On the other hand, the variation of zinc content in the alloy can significantly change alloys properties. A refinement of the structure is observed by increasing the zinc content [50]. However, Zhang et al. [51] showed that in alloys with a content of zinc above 4 wt.% the formation of eutectic structure and micropores during solidification occurs and can result in a coarsening of the microstructure and a degradation of mechanical properties.

Effect of rare earth elements

The effect of RE elements on strengthening of magnesium was for the first time reported in 1930s. Nowadays, the RE elements are widely used in practice as hardeners and refiners. Basically, master alloys with an amount of RE elements up to 25 wt.% are produced [52]. Cerium, thorium, lanthanum, neodymium, yttrium and gadolinium are the most commonly added elements. It was shown by Gao et al. [53] that comparing with the effect of Al and Zn, the solid solution strengthening by Gd and Y is much higher. The hardness increases with the increasing Gd content in Mg solute solutions. Wei et al. [54] show that the addition of Ce, Nd and Y to AZ91 can significantly refine the microstructure and improve mechanical properties at RT and elevated temperatures.

The solubility of Ce in a solid magnesium is significantly lower than of Y. Ce can form a semi- or incoherent precipitates since there is no incubation time before a formation of Guiner-Preston (G-P) zones during decomposition of a supersaturated solution. On the other hand, in alloys with Y content the G-P zones has not been distinguished and metastable coherent precipitates are formed instead. Thus, in Ce containing alloys rapid solid solution hardening takes place, while in Y containing alloys age hardening is prevalent [55]. Furthermore, it was shown [34] that the presence of RE elements in the alloy involves both solid solution and precipitation hardening and their intermetallic phases exhibit low diffusivity and a good coherence to a matrix.

Lu et al. [56] show that addition of RE to Mg–Al alloys leads to the decrease of a volume fraction and size of β-$Mg_{17}Al_{12}$ phase as a result of a precipitation of $Al_{11}RE_3$. Formation temperature of $Al_{11}RE_3$ is by about 150 °C higher than

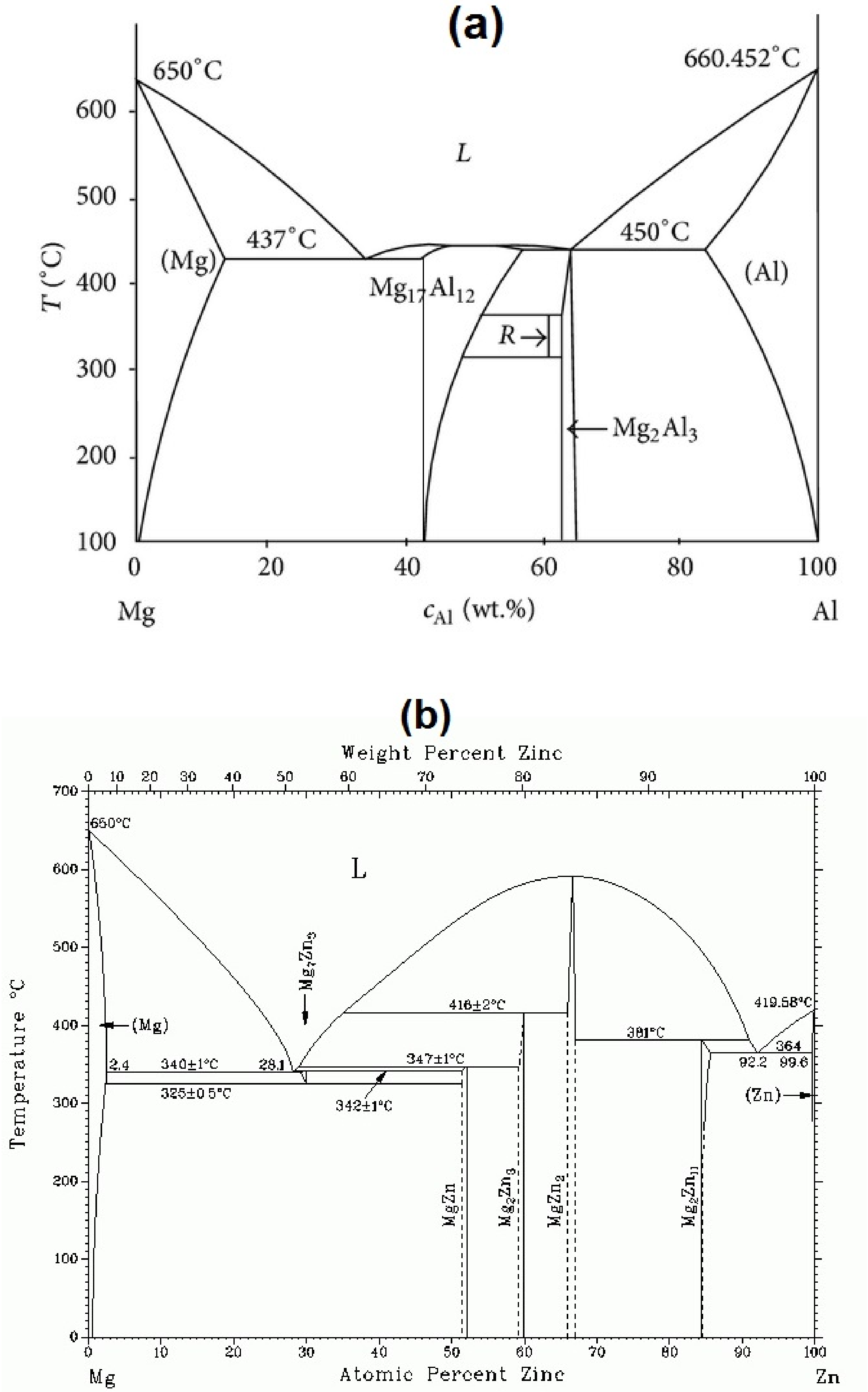

Figure 1.3: Phase diagrams of (a) Mg-Al [48] and (b) Mg-Zn systems [49].

for $Mg_{17}Al_{12}$ phase [57]. Therefore, along with the high stability of $Al_{11}RE_3$, the formation of $Al_{11}RE_3$ starts earlier than that of β-phase.

1.3.2 Effect of grain size

An influence of the grain size on tensile properties, corrosion behavior and deformation mechanisms of polycrystalline materials including magnesium alloys was described by numerous authors [58–64]. The relationship between grain size and mechanical properties is represented by a Hall-Petch relation, which is further described in the next section. Del Valle et al. [64] showed a significant enhancement of ductility of AZ31 and AM60 magnesium alloys at RT after processing by ECAP. On the other hand, it was shown that corrosion resistance can be both decreased [65] and increased [66] by ECAP processing.

Watanabe et al. [67] has shown that at lower strain rates the dislocation creep behavior of AZ31 magnesium alloy is strongly influenced by the grain size. However, at higher strains, with stress exponents larger than n = 5, diffusion-controlled dislocation climb and cross-slip controlled slip take place and no grain size effect is observed.

Nevertheless, measurement of the grain size is associated with a number of difficulties, especially in as-cast magnesium alloys. As the primary α-Mg dendrites are formed during solidification it is difficult to reveal grain boundaries overlapped by dendrite arms. In addition, a presence of non-uniformly distributed β-$Mg_{17}Al_{12}$ precipitates makes the evaluation of the grain size more complicated [68]. Generally, two methods are used to eliminate these complications. Firstly, slight heat treatment can be used to dissolve α-$Mg_{17}Al_{12}$ phases, so suitable etching can reveal grain boundaries. However, annealing leads to a grain growth, therefore, grain size measurements can be unreliable. The second method is an electron back scatter diffraction (EBSD). Since this technique requires more time for both the specimen preparation and the data collection, it has been suggested to use a dendrite arm spacing (DAS) instead of grain size for the description of the microstructure of magnesium alloys.

1.3.3 Effect of dendrite arm spacing

DAS is a microstructural characteristic of as-cast alloys, where the grain size can not be distinguished properly. Similarly as the grain size, DAS is correlated with mechanical properties of metals and alloys. The effect of DAS on mechanical properties of Al-Mg containing alloys have been often reported [69–72]. In the study of Lee and Shin [73] it was shown that the YS of the as-cast AZ91 magnesium alloy has a Hall-Petch relationship with DAS as well as a grain size, and it is described by following equations (1.1),(1.2):

$$\sigma_y = 62.6 + 305.5 \cdot (DAS)^{-1/2} \tag{1.1}$$

and

$$\sigma_y = 74.9 + 317.7 \cdot d^{-1/2}, \tag{1.2}$$

where d is a grain size.

It was also found, that decreasing of DAS leads to an increase of ultimate tensile strength (UTS) and ductility. Radhakrishna et al. [74] derived an empirical relationship between DAS and mechanical properties by Eq. (1.3):

$$Y = A + BX + CX^2, \tag{1.3}$$

where Y is the value of UTS, YS or elongation; X is DAS; A, B and C are constants, where B has a negative value. Thus, in MgSn alloys with the tin addition lower than 5 wt.% the tensile strength and the elongation are improved as a result of a decreasing DAS. Also Mizuno et al. [69] has reported that YS is strongly influenced by DAS.

1.3.4 Effect of segregation and porosity

Another factor affecting mechanical properties of metals and alloys is a presence of bulk defects, such as pores, cracks and segregation bands [75]. These defects are usually formed during casting and lead to significant changes of mechanical properties of materials, such as a premature fracture as well as a reduced strength [25, 76]. These defects can also influence the fatigue behavior [77].

A formation of porosity bands or segregation are often observed under certain casting conditions. Thompson et al. [78] has observed the formation of defect bands in magnesium during high pressure die castings. Dahle et al. [79] has shown that these bands of segregation or porosity follow a contour parallel to the casting surface. A width, location and structure of these bands depend on the aluminium content of alloys. Thus, it is more frequent in AM50 magnesium alloy than in AM60 and AZ91.

During the sheet production where an elevated pressure is used in order to increase effectivity, similar segregation zones are formed. So e.g. during TRC the molten metal solidifies firstly at surfaces close to the rolls and then the heat is transferred by conduction. An existence of non-contact points due to the solidification shrinkage and entrapped gas leads to the heat transfer via a gas layer between metal and rolls. Deformation induced during the ongoing solidification process leads to the excess of defects mainly in the center of the strip [80].

Hereby, the influence of the casting speed, cooling rate, temperature of the melt and other parameters on the final microstructure and a presence of a center line segregation (CLS) is very significant in the sheet production. It was shown by several authors [81, 82] that conventional TRC AZ31 Mg alloy exhibits severe inverse and central segregation of Al and Zn due to its rather wide solidification range. Thus, a characterization of the segregation of secondary-phase particles arising during casting is very important for the improvement of alloys properties and can help to optimize casting conditions.

The formation of CLS was also observed in Al-Mg alloys produced by TRC [76, 83, 84]. Higher cooling rate might cause the formation of a brittle secondary phase distributed on grain boudaries. Its further propagation along the boundaries into the center line segregation might cause cracks and ductile mechanical behavior of the material as well as the initial distortion of the lattice during the segregation of the aloying elements in the center might be the reason of the fracture toughness decrease. It was also shown by Das et al. [76] that tensile strength and microhardness can decrease with increasing cooling speed.

A model describing the formation of various defects during casting has been partially developed by Dahle and St. John [85]. It involves solidification processes and formation of mushy zones, which appear during solidification. Stresses and pressure in this zone can be significant and lead to the formation of defects, such as segregation and tearing. Segregation channels and zones are formed when a fracture of already solidified melt occur at low solid fractions in the melt, whereas their fracture at high solid fractions, when feeding is more difficult, results in porosity and tearing. At medium solid fractions porosity in segregated regions can appear.

It was also shown by Dahle [86] that the location of casting defects caused by shear stresses depends on the relationship between solidification, applied stresses generated from the certain casting process, and liquid flow and feeding mechanisms.

Oxides and porosity can also have a significant effect on the fracture behaviour of the material. A higher stress is concentrated around the pores acting as crack initiation sites causing a premature failure. Thus, the size and distribution of porosity defines a local fracture toughness of alloys [87]. The effect of porosity on strength and ductility of alloys was studied by different authors [88–90]. Surrapa et al. [89] reported that the strength and ductility of Al-7%Si-0.4%Mg depends on the size of macro-pores rather than on a volume fraction of pores in the specimen. Gokhale and Patel [91] have found the areal fraction of porosity on a fracture plane and not average porosity content directly influence the variability of mechanical properties, namely the elongation and ultimate tensile strength in AM60 die cast specimens. They also clarified that variation of mechanical properties of AM50 alloy depends on the amount of porosity on the tensile fracture surface [92].

Lee [88] has studied the effect of microporosity and grain size on tensile properties of an AM60 alloy. In this investigation the ultimate tensile strength and elongation of as-cast AM60 alloy exhibited a significant dependence on the variation of microporosity with an inverse parabolic relationship. UTS and elongation dependence on microporosity increased with increasing grain size, which was explained by the role of grain boundaries in the dislocation motion. Another defects affecting mechanical properties of magnesium alloys are hot cracks, oxide skins and flux inclusions (Fig. 1.4) [93–95].

1.3.5 Effect of texture

Polycrystals consist of grains which are differently oriented toward each other, however, often the most preferable orientation can be distinguished. The texture can be caused both by deformation or recrystallization and can evolve during casting, deformation and heat treatment. In hcp materials with a limited number of available slip systems the texture has usually anisotropic character. At RT basal slip system is dominant. At higher temperatures prismatic and pyramidal slip systems start to develop. This anisotropy leads to the strengthening of texture components.

Primary alloy processing, such as rolling and extrusion, result in a formation of a strong basal texture in magnesium alloys [13, 14]. Kim et al. [97] showed that after hot rolling the AZ31 magnesium alloy exhibit heterogeneous texture along the sheet width. The weakening of basal components from upper layers

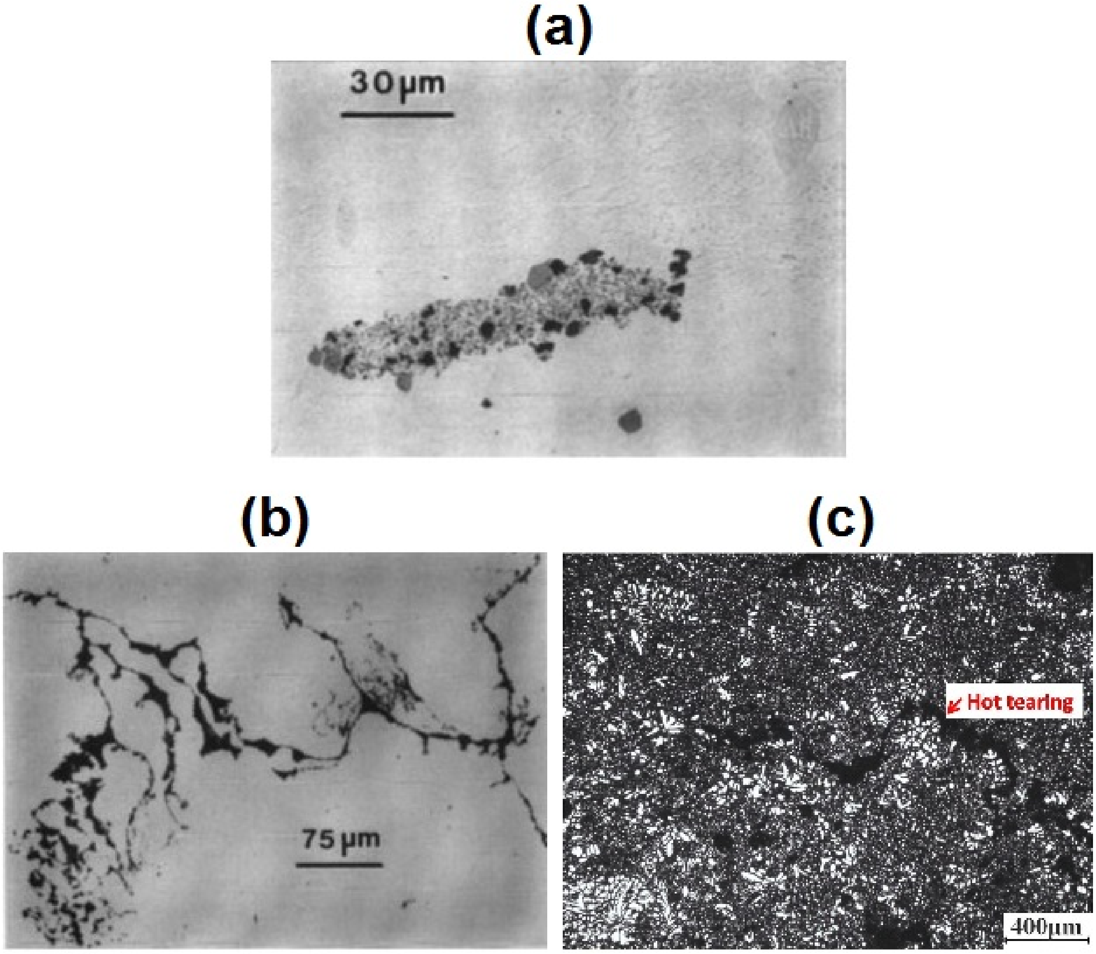

Figure 1.4: Optical micrographs of a) an oxide cluster in AZ91 alloy, b) a "snaky" oxide in AM50 alloy [75] and c) SEM image of hot tearing in AM60 alloy produced by liquid die casting [96].

towards the center and the lower surface was observed. Also after annealing the intensity of {0002} peaks decreases. Perez-Prado [98] showed that in AZ31B the basal texture strengthens significantly during the grain growth.

Texture evolution of AZ31B magnesium sheet produced by ingot casting and subsequent billet rolling during the warm rolling was studied by Jeong et al. [99]. The specimens were pre-heated at 200 °C before the warm rolling. Fig. 1.5 shows pole figures of AZ31 Mg alloy sheets produced by hot rolling and subsequent warm rolling. The texture of hot rolled AZ31 Mg alloy sheets showed ideal normal direction (ND) (0001) fiber texture, while those of warm rolled specimens show that the basal pole spread out to TD. The texture analysis were compared with tensile tests results. It was shown that tensile elongation increases with the decrease of intensity of basal fiber texture. A fraction of basal planes that can be activated for the slip increases with the decrease of the basal fiber texture component intensity. It results in an improvement of a tensile elongation. Thus, the increase of rolling reduction in warm rolling was found to weaken the basal fiber texture and improve tensile elongation.

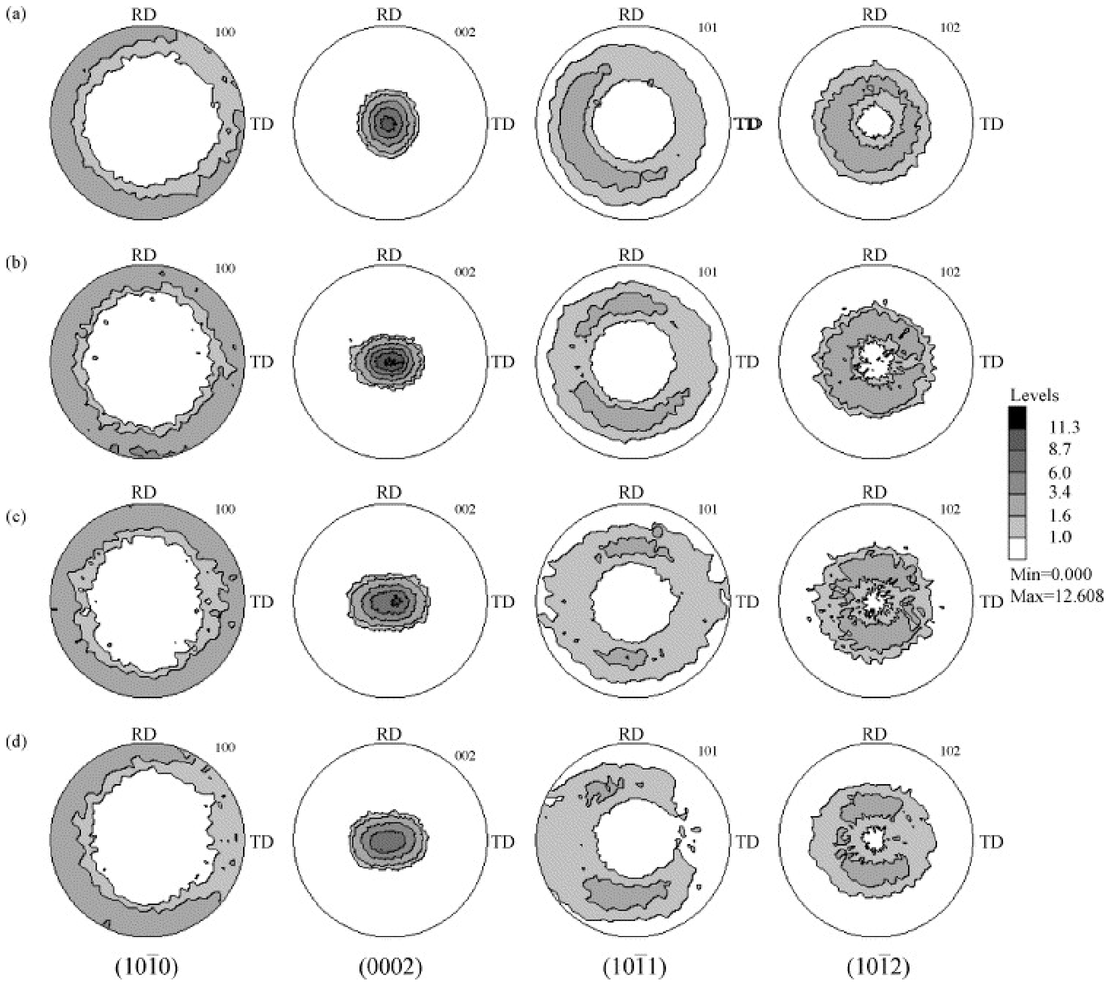

Figure 1.5: The $(10\bar{1}0)$, (0002), $(10\bar{1}1)$ and $(10\bar{1}2)$ pole figures of AZ31 magnesium alloy sheets produced by a) hot rolling and b)18 %, c) 30 %, d) 50 % warm rolling [99].

At larger strains the texture of magnesium alloys is more random because of a grain boundary sliding (GBS), which progressively removes the texture. It was also shown, that grain boundary structure changes affect the texture and the GBS is enhanced by high angle misorientations in Zn-Al alloys [100].

1.4 Strengthening mechanism of metals and plastic deformation

In order to improve hardness and strength of a metal, different ways of changing the structure are used, depending on the material. The high value of strength means high YS and high work hardening coefficient values. A study of processes of the strengthening plays a crucial role in the material science. In sixties of the last century several mechanisms of strengthening of metals were suggested and described. Thus, the grain refinement of the structure leads both to the increase of hardness and improvement of plastic properties of the material. Nowadays, a huge attention is paid to this strengthening method. However, also other methods can contribute to the final mechanical properties. The improvement of the hardness can, however, be accompanied by a decrease of stiffness. Therefore, such a combination of strengthening methods should be found, which suits certain application demands.

In the following chapters basic strengthening mechanisms taking place in magnesium and other light weight alloys will be described. They are listed below.

- Grain boundary strengthening
- Precipitation strengthening
- Solid solution strengthening by substitutional and intersticial atoms
- Dislocation or deformation strengthening

1.4.1 Grain boundary strengthening

Since ancient times the principle "the finer grains the harder is metal" was used in metalworking. However, the first relation between the grain size and the mechanical properties of the polycrystalline metals and alloys was suggested independently by Hall [101] and Petch [102]. The yield stress σ_y is related to the grain size by Eq. (1.4):

$$\sigma_y = \sigma_0 + k \cdot d^{-1/2}, \tag{1.4}$$

where σ_y is a YS, σ_0 is a friction stress, which includes contributions from solutes and particles but not from dislocations, i.e. σ_0 is the flow stress of an undeformed single crystal oriented for multiple slip or approximately the yield stress of a very coarse-grained, untextured polycrystal. k is a constant, which defines the strength contribution due the additional resistance to dislocation motion caused by the presence of grain boundaries [103]. d is a grain size.

From Eq. (1.4) it follows that the yield strength increases with decreasing grain size. Hall-Petch relation is thus one of the most important relations of physical metallurgy. However, some limitations were found in materials with large grain sizes (100 µm and larger) and UFG materials (less than 1 µm), namely, deformed materials where grains do not have a regular shape. Hall-Petch (H-P) relation is valid for different materials with grain size exceeding 20-30 nm [104]. In nanomaterials with smaller grain size the strength does not change or even decreases with decreasing grain size. The explanation of H-P relation by several mechanisms was suggested.

- Dislocation pile-up [105].

  Dislocations interact through their associated stress fields. During plastic deformation a Frank-Reed source generates many dislocations in the same slip plane. A grain boundary is a barrier for the dislocation motion, so the leading dislocation from the source is stopped and other dislocation from the same source will form a pile up. Thus, the leading dislocation experiences a stress τ

  $$\tau = n\tau_0, \tag{1.5}$$

where n is the number of dislocations in the pile-up τ_0 is external resolved shear stress. The pile ups interact with the Frank-Reed source through a back stress which increases as n increases. Therefore, no new dislocation loops are formed by the source and existing loops do not expand.

- Formation of dislocations from steps and ledges on grain boundaries generated during deformation [106].
- Formation of dislocations networks within grain boundary regions [107].

In Eq. (1.4) σ_0 and k depend on a chemical composition and thermo-mechanical treatments, k does not change with deformation temperature, whereas σ_0 significantly increases with decreasing deformation temperature. If the value of σ_y is higher than the grain boundaries strengthening contribution $k \cdot d^{-1/2}$ further strengthening mechanisms must be involved.

1.4.2 Precipitation strengthening

Precipitation strengthening (or hardening) is based on the presence of particles of different phases in the matrix, which serve as obstacles for the dislocation motion [108] and, thus, lead to the hardening of the material. The distribution of this particles in the matrix should be homogeneous. Eq. (1.6) shows the relation between the distance L between particles in the glide plane, the average particle radius $\langle r \rangle$ and their volume fraction f:

$$L = \left(\frac{2\pi}{3f}\right)^{\frac{1}{2}} \langle r \rangle. \tag{1.6}$$

Three types of the particles (coherent, semicoherent and incoherent) might be present in the material. Depending on the type of the dislocation motion dislocations can cut through or by-pass these obstacles. Coherent particles are usually cut through by mobile dislocations and deformed, while incoherent ones are bypassed. The latter process was described by Orowan [109].

Elastic deformation caused by the shift between the matrix and precipitates and different shear elastic moduli of the precipitate and a matrix also contribute to the resulting hardening. The precipitation hardening contribution σ_p is as follows:

$$\sigma_p = \alpha \cdot G \cdot b \cdot L^{-1} \approx \alpha \cdot G \cdot b \cdot f^{1/3} \cdot \frac{1}{r}, \tag{1.7}$$

where α is a constant, G is an shear elastic modulus, b is a Burgers vector.

Also the precipitate morphology and distribution have an influence on the material strengths. It was shown [110] that in randomly textured AZ magnesium alloys, where the basal plates are formed, a lower strengthenning effect was achieved in comparison with the contribution of prismatic plates formed in WE54 alloys. Jain et al. [111] have found that the precipitation on the basal plane can reduce the tension-compression yield asymmetry. Different authors have indicated the important role of the precipitation strengthening in numerous non-ferrous materials [112–115].

1.4.3 Solid solution strengthening

Solid solution strengthening is a very effective strengthening mechanism in magnesium alloys [116]. If prevalent diameters of two atoms differ by less than 15 % the solid solution can be formed. The relative valence, strong chemical affinity and similarity of crystal structures affect the strengthening. It was shown that larger atoms can generate higher strengthening than the smaller ones. However, a low solubility of these elements limits the potential strengthening effect.

Zinc has a significant role in the solid solution strengthening of magnesium alloys. When the content of Zn in Mg-Zn system is below 0.5 at.% the hardening of basal planes and softening of prismatic and pyramidal planes occur. Thus, the ductility is highest at low and medium Zn contents when the strain hardening is reduced. Strain hardening rate increases and the tensile elongation decreases when the concentration of Zn is above 1 at.%. The explanation is based on a gradual compensation of the solid solution softening of the secondary slip system by a solid solution hardening at high solute concentrations [117].

The solution strengthening σ_{ss} for AZ91D commercial alloy was calculated [118]:

$$\sigma_{ss} = k_s C^{2/3}, \tag{1.8}$$

where k_s is a constant and C is an atom concentration. According to Eq. (1.8) the solid solution contribution to the total strength of high pressure die cast AZ91D alloy is about 60 MPa.

In Mg-Al-Zn systems, where α-Mg solid solution is the major hardened phase, the hardness H can be described by Eq. (1.9) [116]:

$$H = H_0 + K\left(X_{Zn} + \frac{1}{2}X_{Al}\right), \tag{1.9}$$

where H_0 is a constant with a value of approximately 50 kg/mm^2, K is a constant with a value 10 kg/mm^2, X_{Zn} and X_{Al} are contents of Zn and Al, respectively, in atomic percent.

1.4.4 Deformation strengthening

Not only the grain size and precipitates can influence the hardening process of alloys. Since hardening requires the presence of obstacles for the dislocation motion, immobile dislocations found in matrix can be considered as effective sources of strains. Therefore, the deformation (dislocation) strengthening is the strengthening caused by the dislocations substructure appearing during plastic deformation or phase transformation [119]. Mobile dislocation can interact with the locked ones, with dislocation networks or with other mobile dislocations. The value of dislocation strengthening σ_{ds}, thus, depends on the energy necessary to pass through the dislocation network, which is usually described by parameter ρ, the dislocation density. Therefore, the contribution of the dislocation strengthening can be expressed by Eq. (1.10):

$$\sigma_{ds} = \alpha \cdot G \cdot b \cdot \rho^{1/2}, \tag{1.10}$$

where α is a constant.

1.5 Heat treatment

Most of the magnesium processing operations are made at high temperatures because only the $\langle a \rangle$ basal slip and tensile twinning can be activated at RT. Heat treatment is a method of the ductility improvement of magnesium alloys, and significantly influences the activity of non-basal slip systems.

The effect of heat treatments on the deformation behavior and their influence on the deformation modes in magnesium were often studied [120–122]. These works indicate the athermal behavior of the $\langle a \rangle$ basal slip and twinning. It means that they are the easiest activated deformation modes at both RT and ambient temperatures. The value of critical resolved shear stress (CRSS) decreases with increasing temperature. CRSS is a shear stress on slip planes needed to realize the dislocation slip. CRSS for $\langle a \rangle$ non-basal slip systems is lower than for the $\langle c + a \rangle$ pyramidal ones. In addition, at the temperature range 100 - 300 °C a compression twinning has the highest CRSS for all deformation modes.

The effect of heat treatment on the microstructure of Mg-Al based alloys, the solutioning processes and precipitation manner of $Mg_{17}Al_{12}$ phase were often investigated [123–126]. Generally, both tensile strength and elongation can be substantially raised or the YS and hardness can be significantly increased but with appreciable loss of ductility. During the solutioning or stabilizing heat treatment the stresses produced by the original casting are removed. However, the following quenching can newly introduce internal stresses into the material. It was shown by Liu et al. [127, 128] that the ductility decreases after annealing due to the precipitation at grain boundaries.

In AZ31 alloy the presence of the γ-liquid phase formed at temperatures higher than 460 °C can remarkably influence the deformation behavior [129]. Abedi et al. [130] has observed high ductility values above the melting point of β-$Mg_{17}Al_{12}$ intermetallic phase ($\approx$ 462 °C). This improvement has been attributed to the effect of the liquid phase on stress relaxation, cavities retardation and grain boundary sliding.

It should be noted that magnesium alloys tend to age-harden very slowly at ambient temperatures. Nevertheless, alloys in the T4 temper are susceptible to RT aging. Thus, the aging of AZ63-T4 for five years at 297 K to 305 K caused an increase of tensile strength by about 14 %, of YS 68 %, and of Brinell hardness by 22 %. In the same period, the ductility was reduced by about 32 % and the resistance to impact by 57 % [116].

1.6 Dynamic recrystallization

In wrought magnesium alloys, such as AZ and WE [131], the probability of a recrystallization nucleation can be increased during annealing by means of intermetallic precipitates, which refine the microstructure and inhibit the grain growth through pinning or Zener drag mechanism. The investigation of AZ91 alloy showed that a very fine grain structure can be produced by, so called, dynamic recrystallization (DRX) during high temperature extrusion [132]. Similar results were reported by other research groups on different magnesium alloys [129, 133–135]. During the recrystallization of the material deformed grains with a large portion of stored energy are replaced by new ones. The recrystallization is defined as a static if occurs during annealing of the cold worked alloy [136–138]. On the other hand, the DRX takes place during a deformation at elevated temperatures. The rearrangement or annihilation of dislocation structure after annealing is defined as a recovery process (or dynamic recovery (DRV)). The recovery can also run statically or dynamically depending on whether the annealing was applied after or simultaneously with the deformation. Previous studies indicate that in materials with hcp structure both DRX and DRV can play a significant role. Namely, in α-Ti and α-Zr, where the temperature limit of DRX is higher, DRV has a dominant role, whereas Mg and Zn undergo DRX [139, 140].

Thus, for AZ31 several microstructural observations have been made to define the heterogeneous combination of twinning, multiple slip, DRV and DRX. Vagarali et al. [141] have studied the creep behavior of the polycrystalline magnesium over the temperature range from 473 to 820 K. Depending on the temperature and stress level three different mechanisms were defined. At lower temperatures up to 600-750 K the extensive basal slip was observed. This process is controlled by dislocation climb. At temperatures above 600-750 K an extensive non-basal slip occurs. Under these conditions the dislocation cross-slip from basal to prismatic planes takes place. Finally, at higher temperatures and stresses below 2.5 MPa no visible surface slip lines were present. This behavior is attributed to a transition to a lattice diffusion creep at these very low stress levels.

The DRX is very important for magnesium alloys and other non-ferrous materials allowing to control the grain size and, thus, final mechanical properties. Most common conventional methods of thermomechanical treatments used for the grain refinement of magnesium alloys are extrusion and forging [142, 143].

1.7 Casting of magnesium alloys

Nowadays, die casting is still one of the most commonly used techniques in magnesium industry. However, there are other techniques used for the high-quality alloys production including high-pressure die casting, permanent mold casting, sand casting, semi-solid and squeeze casting [2, 144–147]. Properties of the final product depend on the composition and methods used. Moreover, the properties of alloys with the same composition can differ depending on a casting method and selected casting conditions.

Magnesium sheets produced by direct-chill (DC) casting exhibit coarse grained structure (150-500 μm) [148] and are expensive due to the repetitive heating and large number of rolling passes [149].

The use of a new generation of continuous casting techniques, such as strip casting especially TRC [147, 150, 151], which allow to get more homogeneous structure with eqiuaxed grains, is now under an intensive investigation. Moreover, sheet production is retarded because of a limited formability of magnesium alloys at RT. Since rolling forms strong basal texture in magnesium sheets with c-axis parallel to the ND of the sheet [15], the activation of non-basal slip systems is restricted. Therefore, the semi-solid continuous techniques, where elevated temperatures are used during the sheet forming, are preferred for magnesium alloys casting.

1.7.1 Twin-roll casting

TRC can be used for casting of thinner materials with high quality surfaces and, thus, better mechanical properties. It belongs to continuous casting methods using spinning "endless" rolls. The principle of TRC is described in Fig. 1.6. A melt is fed through a nozzle into the gap between two rotating water-cooled rolls and then cools down and solidifies between the rolls.

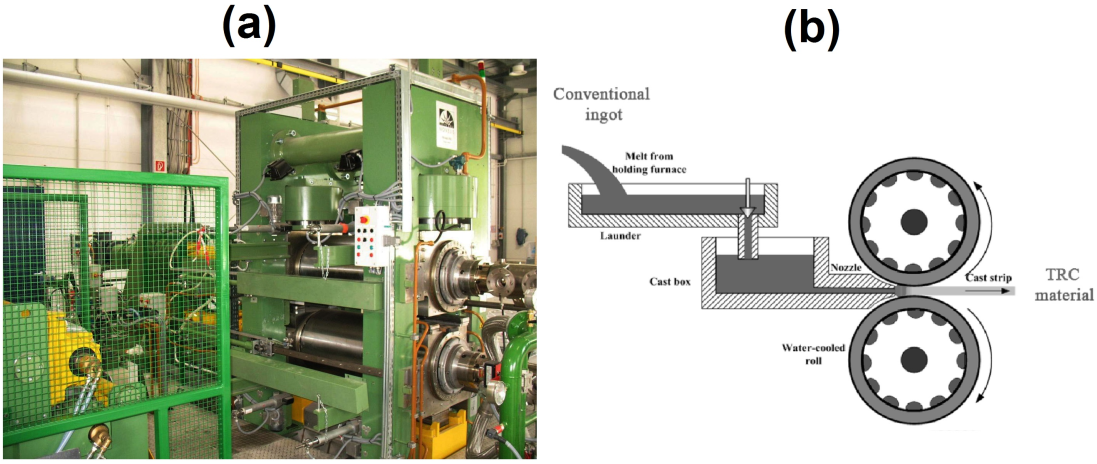

Figure 1.6: Illustration of twin-roll casting process [151]: a) twin-roll caster and b) scheme of the twin-roll casting process.

TRC has been successfully applied on aluminium [152, 153], steels [154, 155] and magnesium alloys. It also allows to produce magnesium alloy strips of the 4-6 mm thickness with high solid solution supersaturation and relatively large elongated grains [150, 151]. The effectiveness of TRC for magnesium alloys was shown by several research groups [147,156,157]. In contrast to conventionally cast alloys TRC strips have heterogeneous structure but much finer grain structure (50-100 µm). This process incorporates casting and hot rolling into one step and, therefore, is assumed to be more efficient. Since TRC strip thickness is only about 5-6 mm, this process is characterized by extremely high production rate due to the possibility of fast-cooling of the melt down to 550 °C. Therefore, non-intermittent withdrawal regime is reached, which leads to the absence of cracks in the surface layer, non-homogeneous structure, and can lead to the fine grained structure. High cooling rate also reduces the manufacturing cost. At the same time, high solidification rate enables to produce strips with refined grain structure, which is also characterized by refined dendritic cells, fine intermetallic particles and an increase in a solid solubility and a presence of metastable phases.

Strips produced by this technique can be easily used for further processing by heat treatment or plastic deformation including SPD.

1.8 Equal-Channel Angular Pressing

ECAP is a processing method in which a metal is subjected to an intense plastic straining through simple shear without any corresponding change in the cross-sectional dimensions of the sample [16]. It allows to reduce the grain size of the material and obtain new strong deformation textures.

During the process the sample is pressed through a die consisting of two channels with equal cross-section using a plunger, as it is shown in Fig. 1.7. It is deformed primarily by simple shear along the plane of intersection between the channels. Two angles are associated with the process and can vary: an angle between the channels Φ and an angle Ψ at the outer arc of curvative of the channels intersection. Since dimensions of a sample are not changed, the process may be repeated. Furthermore, the sample may be rotated between passes in order to change the inclination of the shear plane to the existing microstructure. According to the rotation scheme present in Fig. 1.8 possible routes are identified as A, B_a, B_c, and C.

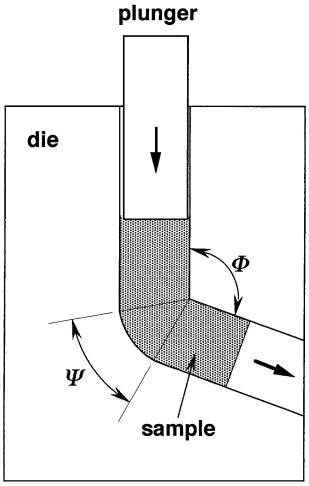

Figure 1.7: Schematic illustration of equal-channel angular pressing [158].

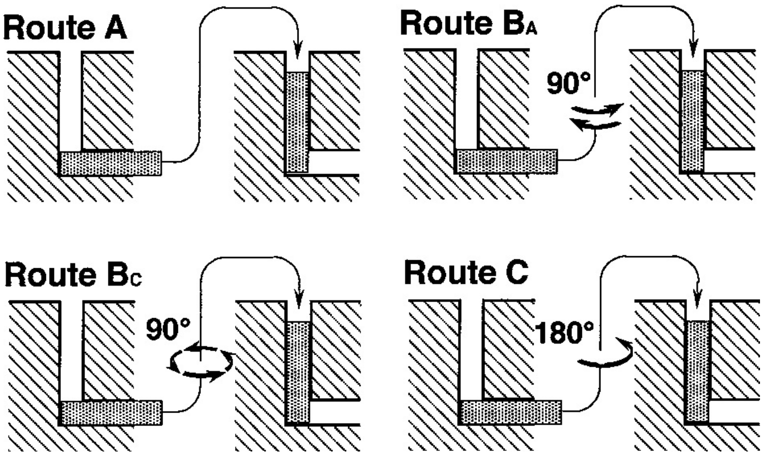

Figure 1.8: Illustration of possible equal-channel angular pressing routes [159].

ECAP has been often suggested as a method for changing the texture or microstructure of Mg alloys [62, 160–162]. This process can induce severe shear deformation of materials, which can weaken the basal texture or reduce the grain size, and thus, enhance the room temperature ductility.

Mukai et al. [163] compared the texture and resulting mechanical properties for AZ31 billet material obtained via both direct extrusion and equal channel angular extrusion (ECAE). They found that the strong preferred alignment of basal planes parallel to the extrusion axis, that is characteristic of the direct extrusion of magnesium, was absent in the material subjected to ECAE and that it led to a significant enhancement of elongation to failure for specimens tested in the extrusion direction. However, this is not the entire picture. A similar investigation conducted by Agnew et al. [161] found that although the texture in the ECAE material was oriented differently to that for direct extrusion, it was nonetheless just as strong, and mechanical properties were anisotropic in both cases. This has similar implications in the design and fabrication of components. Matsubara et al. [164] found that a combination of direct extrusion followed by ECAE was the most effective in achieving a grain size < 2 μm in dilute magnesium alloys. Conform has recently been adapted for the continuous ECAE processing of long lengths aluminum rods [104] and it appears to be an optimal combination of these two processes.

During ECAP of magnesium alloys very fine grained structures are formed via DRX [165,166]. It is based on the same principle of DRX as was described in Section 1.6 except for larger strains introduced into the material during ECAP. Figureido and Langdon [167] have suggested a model of grain refinement of magnesium alloys during ECAP. According to this model the formation of new grains along the original grain boundaries of initial coarse grained structure occurs when the grain size d is larger than the critical size d_c. If magnesium with the initial grain size d lower than d_c is deformed, the resulting structure is homogeneous. In the opposite case the necklace structure of smaller grains is formed at grain boundaries. Since the grain boundaries length in the materials with coarser grains is higher than in the fine grained materials, more new grains can be nucleated at these grain boundaries.

However, this model provide just a simplified view on these processes. The development of the general theory of the grain refinement mechanism is difficult because the ECAP is a complex process which depends on the initial texture, grain size and temperature.

1.9 Constrained Groove Pressing

UFG materials with the grain size of less than 10 μm can be produced using a variety of SPD techniques. For magnesium ECAP and high pressure torsion (HPT) are the most popular procedures [168–170]. However, these methods are non-continuous, use relatively small samples and can be hardly applied to magnesium strips. For plates and sheets production the accumulative roll bonding (ARB) [171–173], repetitive corrugation and straightening (RCS) [174,175], CGP [176] and constrained groove rolling (CGR) [177] are used. ARB process consists of repetitive bonding between two rolled plates, but a perfect bonding is required to achieve improved mechanical properties. Thus, ARB is less feasible for SPD of sheet metals. Discontinuous RCS can reduce the grain size of a cooper bar to several hundred nanometers [175]. However, using the continuous RCS method 18 cycles are necessary to achieve nanostructured material since not a sufficient amount of plastic strain is provided by existing RCS facilities.

On the other hand, groove pressing (GP) and CGP were successfully used to deform aluminium [178], aluminum alloys sheets [179,180], copper and their alloys [181] and low carbon steels [182,183]. It was reported that due to UFG structure induced by GP mechanical properties of metals, such as formability, were enhanced. For example, the effective grain refinement and submicron features achieved by GP improve mechanical properties and bioactivity of pure titanium which has similar hcp structure as magnesium [184].

However, the information on GP magnesium alloys is limited. Ratna Sunil et al. [185] studied the wetability and corrosion resistance of GP AZ31 magnesium alloy and showed the prospects in its application as implants. The AZ31 alloys sheet were heated up to 537 K before the pressing between the grooved dies, which are designed with a groove angle of 45°. The CGP steps are shown in Fig. 1.9: (a) – a specimen is placed in the grooved die, (b) – groove pressing, (c) – flat pressing, (d) – the specimen is rotated by 180° along the pressing direction and (e) – the groove pressing stage is repeated, (f) – specimen is flattened again. Thus, a single pressing by grooved dies yields a shear strain of 1 at deformed regions, which is equal to the 0.58 of an effective true strain [186]. After the flattering the cumulative effective strain in the deformed regions become 1.16, which is comparable to the strain after one ECAP pass, which is equal to 1.

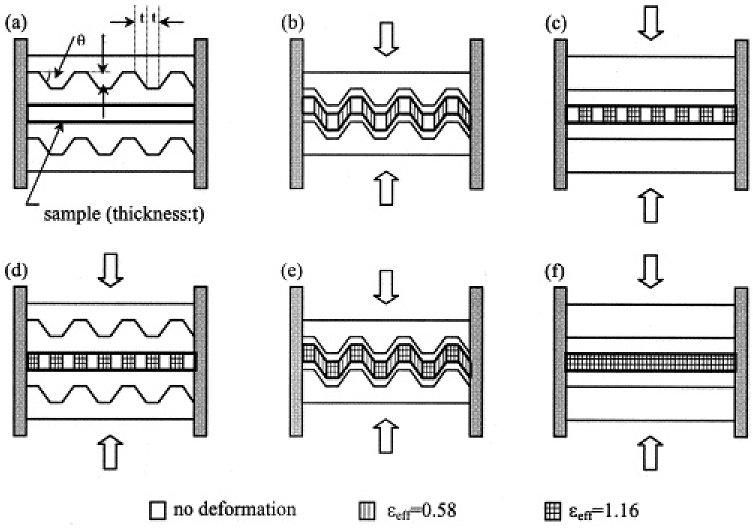

Figure 1.9: Illustration of constrained groove pressing process: a) grooved die, b) groove pressing, c) flat pressing, d) the specimen is rotated by 180° along the pressing direction and (e) the groove pressing stage is repeated, (f) specimen is flattened again [186].

It was also shown by Shantharaja et al. [178] on aluminium alloys that the pressing parameters, such as the number of passes and deformation speed have significant influence on mechanical properties. Due to the grain refinement the ductility of pure Al increases in terms of tensile strength. An effect of precipitation during CGP of AA3003 aluminium alloy was considered by Apps et al. [187]. It was shown that Mn increases work hardening rate because of the formation of Al_6Mn fine dispersoids in the solid solution. Thus, the presence of such particles can accelerate the improvement of mechanical properties and grain refinement. However, no data on Mg-based alloys are available.

2. Aims of the study

It the previous chapter the TRC process was described as an effective method to produce high quality thin magnesium strips. The main aim of this study is to investigate microstructure and mechanical properties of a model AZ31 TRC magnesium strip. Generally, TRC magnesium strips exhibit strong basal texture and heterogeneous grain size distribution. In order to fully exploit a potential of TRC thin strip and to suppress some unfavorable features of the initial microstructure attempts to modify properties of the TRC material were done. SPD techniques were used as an effective tool. First, well-established ECAP technique was used as a model SPD treatment serving as a precursor for investigation of materials prepared by a relatively new, unexplored and more complex CGP method.

In order to achieve the above mentioned aims the present work focuses in particular on following tasks:

- The study of the microstructure and mechanical properties of light weight AZ31 structural magnesium alloy prepared by TRC and their comparison with conventionally cast ingot of a master alloy (AC)
- The detailed study of a center line segregation in TRC alloy using different imaging methods and analyses
- The effect of the annealing temperature on a stability of AC and TRC materials
- The effect of ECAP on the initial AC and TRC microstructure
- Application of CGP as a novel continuous SPD technique for a modification of microstructure of magnesium alloys strips prepared by TRC

3. Experimental part

3.1 Materials preparation

Two types of magnesium alloy with nominal chemical compositions of Mg-3.3Al-0.9Zn were studied in this work (Fig. 3.1). Detailed chemical composition of the alloys is shown in Table 3.1. Specimens for all measurements were cut from original ingots of master alloys or from strips prepared by TRC. The thickness of strips after TRC was 5.6 mm.

Table 3.1: Chemical composition of AZ31 alloy, wt.%.

Al	Zn	Mn	Na	Ca	Fe	Mg
3.3	0.91	0.34	0.20	0.034	0.020	Rest

The temperature of the melt before processing was 650 °C and casting rate was 1.8 m/min. Recently Kurz et al. [151] has shown that only at these casting parameters the strip exhibits the most homogeneous structure and contains no cracks at the surface layer and no cavities in the bulk of the strip. Three main casting directions denoted as rolling (RD), transverse (TD) and normal (ND) are marked in Fig. 3.1.

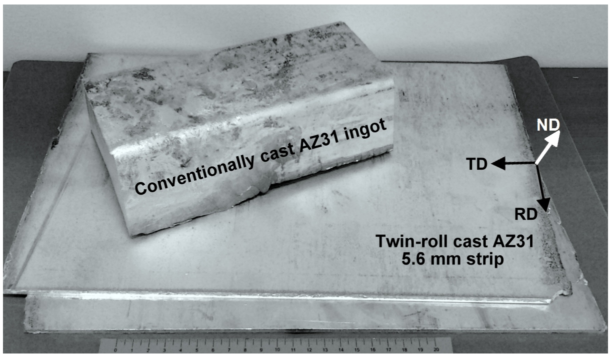

Figure 3.1: Picture of the AZ31 AC ingot of the master alloy and strip produced by TRC.

3.2 Heat treatment

Specimens of 10 mm x 10 mm x 10 mm for structural and hardness studies were cut from the AC ingots. Similar specimens were cut from TRC strips with dimensions 10 mm x 10 mm x 5.6 mm. To study the influence of annealing on a microstructure in a temperature range from RT to 400 °C a linear annealing scheme in an air furnace with 1 °C/min heating rate followed by a quenching into an oil bath was performed. A thermal stability of primary phases in AZ31 was tested at 300 and 500 °C.

3.3 Electrical resistivity measurements

In order to establish temperature intervals in which phase transformations occur in the material the electrical resistivity measurements were performed. This technique also allows to detect structural changes and phase transformations in materials. For better understanding of processes occurring in material the definition of resistivity should be stated. The resistivity ρ is a material property which is defined using Eq. 3.1:

$$\rho = \frac{S}{l} R, \tag{3.1}$$

where S is a cross-section area, l is length and R is a resistance of the sample.

In metals the current is carried by electrons. According to the Pauli's exclusion principle no two electrons in one atom can have the same set of four quantum numbers. At absolute zero electrons stay at the lowest energy states. At ambient temperatures a certain fraction described by Fermi function $f(E)$ (Eq. 3.2) will exist above the energy of the highest occupied single particle state at 0 K, or so-called Fermi energy [188].

$$f(E) = \frac{1}{e^{(E-E_F)/kT} + 1}, \tag{3.2}$$

where E is energy, k is a Boltzmann's constant, T is an absolute temperature and E_F is the Fermi level, e.g. an energy level with an occupation probability of 50 % at a finite temperature. In the band theory of solids Fermi level defines bands. For conduction process the presence of electrons in a conduction band is very important. In conductors a conduction band is overlapped with a valence band, so the electrons can easily move. However, in a real solid the electrons scatter by collisions with defects and atomic thermal vibrations. Thus, the resulting resistivity ρ_{total} is defined by Mathiessen rule (Eq. 3.3) as a sum of resistivity caused by scattering on thermal vibrations ($\rho_{thermal}$), impurities ($\rho_{impurity}$) and deformation-induced defects ($\rho_{deformation}$):

$$\rho_{total} = \rho_{thermal} + \rho_{impurity} + \rho_{deformation}. \tag{3.3}$$

Generally, electrical resistivity of metals increases with temperature due to increasing thermal vibrations and density of vacancies. Electron-phonon interactions can play an important role affecting the resulting resistivity. It was described mathematically by Bloch-Grueneisen formula [189]:

$$\rho_{thermal}(T) = \rho_0 + A \left(\frac{T}{\Phi_R} \right)^n \int_0^{\frac{\Phi_R}{T}} \frac{x^n}{(e^x - 1)(1 - e^{-n})}, \tag{3.4}$$

where ρ_0 is a residual resistivity due to defect scattering, A is a constant, Φ_R is the Debye temperature and n is an integer depending on the interaction (5 for electron-phonon scattering, 3 for s-d electrons scattering, 2 for electron-electron interaction).

Metal lattices are not pure and contain defects such as dislocation, vacancies and impurities. Eq. 3.5 describes the relation between resistivity and impurities concentration ($c_{impurity}$).

$$\rho_{impurity} = A_i c_{impurity}, \tag{3.5}$$

where A_i is a constant independent on the concentration and temperature and differs for each impurity.

In addition the resulting resistivity of an alloy consisted of two phases ($\rho_{\alpha+\beta}$) can be calculated as follows:

$$\rho_{\alpha+\beta} = \rho_\alpha V_\alpha + \rho_\beta V_\beta, \tag{3.6}$$

where ρ_α, ρ_β are the resistivities of certain phases and V_α, V_β - volumes of these phases.

In this study a four-point resistance measurement method was used for sensitive measurements of low resistance changes [190]. For that purpose H-shape specimens with dimensions 60 mm x 5mm x 1mm were prepared (Figure 3.2). Voltage is measured between two inner contacts. Commutated direct current is used to eliminate transient and thermoelectric effects. Annealing below 240 °C was performed in an oil bath with a step-by-step annealing regime 20 °C/20 min. Annealing at higher temperatures was performed with the same heating rate in an air furnace. A residual resistance in a liquid nitrogen (LN) using a Keithley based measurement devices with an operating current $I = 0.2$ A were used. Because of the accuracy of samples dimensions measurements (about 2 % limit), instead of the absolute resistivity measurements relative resistivity changes $(\rho - \rho_0)/\rho_0$, where ρ_0 is the initial value of resistivity measured in LN, and a residual resistivity ratio $RRR = \rho_A/\rho_0$, where ρ_A is a resistivity measured in an ethanol bath at RT, were used for further data processing.

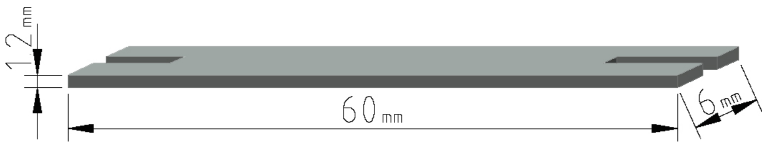

Figure 3.2: Illustration of the H-shape sample used for resistivity measurements.

3.4 Microstructural characterization

3.4.1 Light optical microscopy

Microstructure characteristics of studied alloys were obtained using Olympus GX51 light optical microscope. Standard metallographic magnesium sample preparation techniques were used. Firstly, mechanical grinding on SiC abrasive papers (800 to 4000 grits), polishing with diamond pastes (1 and 3 μm) and with a colloidal silica polishing suspension OP-S were performed. For the final etching of AZ31 alloy a 5 % acetic picral solution was applied at RT for about 5 - 10 s.

Images from light optical microscopy (LOM) were processed using NIS-Elements AR 3.0 software. The grain size evaluation of coarse grained materials was made on cross-sections of samples. A linear intercept method was used for this aim. For materials after thermomechanical treatment containing much finer grains the images were processed by an automated grain boundaries identification procedure which is a part of the AR 3.0 software and further calculating of an equivalent diameter of grains using special software functions. The advantage of this method is the ability to get a distribution of grain sizes (see Fig. 3.3) instead of an average grain size that can be received by the linear intercept method. It is very useful tool for the investigation of materials with heterogeneous distribution of grain sizes after processing, which are used in this work, e.g. Fig. 3.3. Moreover, it allows more accurate determination of the grain size changes along the material width during thermo-mechanical treatment of the strips.

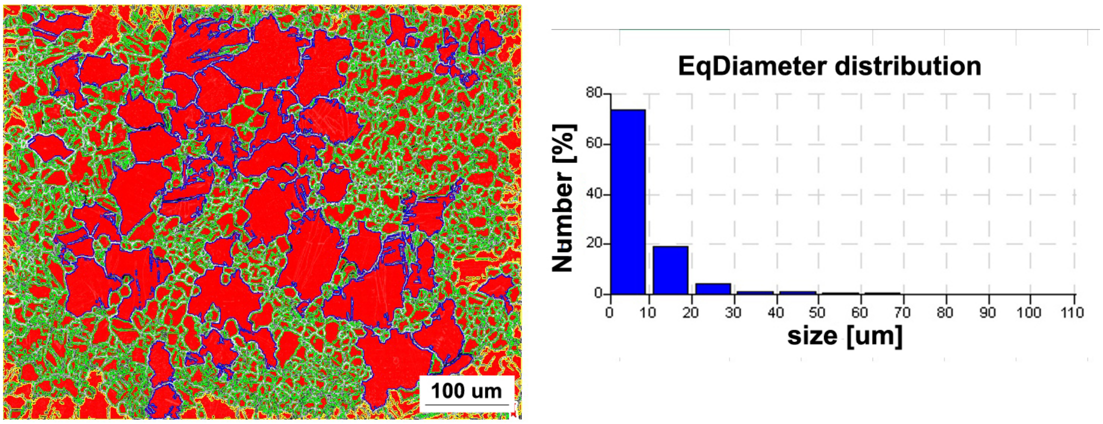

Figure 3.3: Heterogeneous distribution of grain sizes in AZ31 magnesium alloy after CGP evaluated using the equivalent diameter method via NIS-lements AR 3.0 software.

In alloys with developed dendritic structure the determination of an average grain size is more complicated. Therefore, the DAS was used instead of the grain size for such samples.

3.4.2 Scanning electron microscopy

Scanning electron microscopy (SEM) was also used to study the microstructure of selected alloys. An electron beam of an energy of 10-20 keV is focused to a spot of about 4 - 5 nm in diameter. The electromagnetic lenses deflect the beam and provide a raster scanning over a selected area of the specimen. Resulting image is produced by a secondary signal of back-scattered (BSE) or secondary electrons (SE). BSE are elastically scattered primary electrons which do not lose their energy during the interaction with the surface but only change their direction. Mainly, atomic number Z is responsible for the intensity of BSE. The higher is the atomic number, the higher is the intensity. Therefore, areas with higher Z are brighter on images obtained by BSE. This type of signal is used for the elementary and phase distribution analysis.

The primary electrons can lose some energy after scattering, which is transmitted to atoms in the surface layer. These atoms are excited and the emission of the secondary electrons from an inner shell occurs. If the excited electron has sufficient energy after inelastic and elastic collisions it can escape from the surface. Since it lose its energy during this movement the final energies are low (about 50 eV). However, it allows to obtain an information about a topography of the sample because rough and bumpy surfaces emit more SE and has lighter tone on the SE image than the smooth ones.

Energy-dispersive X-ray spectroscopy (EDX) is a very powerful tool for the materials characterization. Interaction of the primary electrons with the surface excites atoms in the surface layer which must return to the ground state. So an electron hole is left after the ejection of the core electron. Electrons fall down to the lower orbitals and leave the excited state, so the energy is emitted in the form of photons. They form the spectrum of the element (X-ray). An energy of X-rays is determined as the energy difference between two shells. It allows to establish the atomic structure of the element and to investigate the chemical composition of materials. In contrast to LOM, SEM has significantly larger depth of focus so more information about the microstructure can be obtained.

SEM observations were realized on a FEI Quanta FEG and Zeiss Auriga electron microscopes. These microscopes are equipped with BSE and SE detectors, detectors for energy dispersive spectroscopy (EDS) and EBSD detectors. The sample preparation for SEM observation was the same as for samples observed by LOM.

EBSD and texture measurements

EBSD measurements [191] are held in SEM, where a stable electron beam is focused on the sample tilted 70° towards the diffraction camera in order to increase the contrast in the resultant EBSD pattern. Electrons elastically scattered on the (hkl) plains which fulfill the Bragg's criterion (Eq. 3.7) are the BSE.

$$2d_{hkl} \sin \Phi = n\lambda, \tag{3.7}$$

where d_{hkl} is an interplannar distance in a crystal lattice, Φ is a scattering angle, n is a positive integer and λ is the wavelength of incident wave.

They are moving along the pair of pyramidal cones with the top angle $\pi - 2\Theta$ and the main axis formed by the normal of (hkl) plains. Escaping electrons may exit near to the Bragg angle and diffract to form Kikuchi bands which correspond to each of the lattice diffracting crystal planes. The middle of the each Kikuchi band corresponds to the intersection of the plain on which the Kikuchi band was formed with the plain of the screen.

Relative position, direction, thickness and a position of the intersections of the Kikuchi lines is an important information obtained from the diffraction pattern. Crystallographic orientation map of the scanned area is calculated from the position of Kikuchi bands by the computation processing of diffraction patterns collected by CCD camera.

Precise position of Kikuchi lines is found using polar Hough transformation from which the orientation of the exact part of the sample is determined. The transformation between the coordinates (x, y) of the diffraction trace and coordinates Haugh space is given by the Eq. 3.8.

$$\rho = x \cos \Theta + y \sin \Theta, \tag{3.8}$$

where (ρ,Θ) are the coordinated in the Haugh space.

When the relative angles between the plains are calculated using the calibration system, the relevant Miller's indexes are determined. After that the orientation of the crystal lattice with the respect to the sample orientation can be defined.

Specimens for EBSD were prepared by two methods depending on the composition and grain size after processing. For as-cast TRC and AC AZ31 alloys an electropolishing using a Struers AC2 solution (10 ml of nitric acid, 30 ml of acetic acid, 40 ml of distilled water and 120 ml of ethanol) was performed at 20 V and -30 °C. For alloys after intensive plastic deformation with much finer grains the mechanical polishing was followed by an ion argon milling at 3 keV for 3 h using Gatan PIPS equipment.

EBSD data were collected in Quanta FEG scanning electron microscope and were handled using OIM Analysis 6 software. Observations of as-cast samples were made in the section perpendicular to the transverse direction of the TRC strip. The materials after the ECAP processing were observed in the cross-section of the specimens. The direction perpendicular to grooves in specimens after constrained groove pressing was used for EBSD study.

The EBSD maps were obtained by scanning areas of selected dimensions but at least 150 μm × 150 μm. In addition, depending on the grain size different steps from 0.1 to 3 μm were used. The correlated data were used also for texture analyses of materials. Texture studies were provided by the means of (0002) and $\{10\bar{1}0\}$ pole figures calculated from the EBSD orientation maps. In some cases EBSD maps of smaller areas were used for the texture studies. The dimensions are given in the text if needed.

In order to analyze local strains inside the material, Kernel Average Misorientation maps (KAM) were used. This method allows to distinguish small differences in crystallographic orientations (angular misorientations) between neighboring points in the specimens. These maps are used to reveal internal strains caused by a presence of dislocation structure, which leads to crystal rotations and a higher value of the KAM [191].

3.5 Atomic force microscopy

The investigation of changes in the surface topography after tensile test were performed using atomic force microscopy (AFM). The principle of AFM is a measuring of a force between a probe and the sample. A sharp tip is usually used as the probe. The lateral resolution of AFM is low (about 30 nm). However, the vertical resolution can be up to 0.1 nm. Fig. 3.4 illustrates an AFM imaging scheme. An optical level is used to measure the vertical and lateral deflections of the cantilever. It is operated by reflecting a laser beam off the cantilever. The beam interacts with a position-sensitive photodetector. The differences between segments of the photodetector and signals indicate the position of the laser spot on the detector and thus the angular deflections of the cantilever. Piezoceramics allow high resolution positioning of the tip.

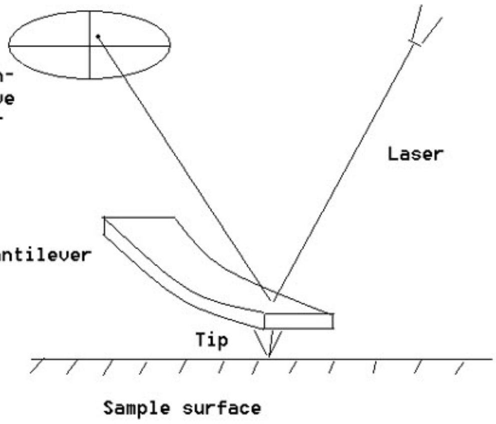

Figure 3.4: Illustration of an operating scheme of atomic force microscope [192].

The samples for AFM observations were prepared using the same way as LOM specimens. The areas of 100 µm × 100 µm were scanned using the AFM tapping mode. In this mode the cantilever oscillates at its resonant frequency. The probe lightly "taps" on the surface of the sample during scanning, contacting the surface at the bottom of its swing. By maintaining a constant oscillation amplitude a constant tip-sample interaction is retained and the image of the surface is captured.

3.6 X-ray diffraction

Texture X-Ray diffraction (XRD) measurements were done on AZ31 alloy in order to statistically strengthen EBSD data. XRD data were obtained on Rigaku Smart Lab 9kW Thin-Film In-Plane X-ray Diffractometer at a voltage 8 keV using Shultz reflection method with a spot size 0.4 mm × 0.5 mm. Specimens were tilted from 0 to 90°, azimuthal rotations were made from 0 to 350°, both with a step of 10°. Texture was measured using XRD by systematically changing the angular orientation of the sample and measuring diffraction peaks. The intensity of Bragg reflection was measured for pairs of Ψ and Φ at fixed $\Theta - 2\Theta$ position and is presented as pole figures (PF). Fig. 3.5 shows the scheme of the XRD and orientation of the sample during the experiment. These investigations were held in a collaboration with Karlsruhe Institute of Technology.

3.7 X-ray computed tomography

LOM and electron microscopy can provide very proper microstructural information. However, they are limited to small-scale regions of samples and they are not suitable for receiving general information about the whole volume of the material. Thus, the penetration into the middle of the strip in order to study the defects, such as CLS in TRC materials, needs novel 3D approaches. In cooperation with University of Applied Sciences Upper Austria the study of CLS using X-ray computed tomography (CT) were done.

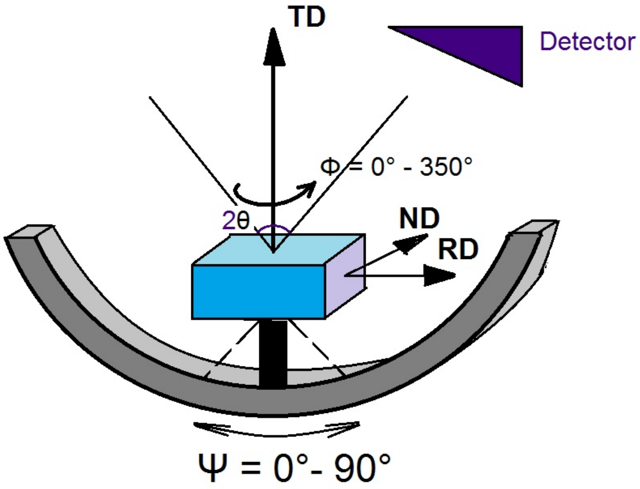

Figure 3.5: Illustration of X-ray diffraction measurements using Shultz reflection method.

X-ray microtomography belongs to the class of nondestructive 3D material characterization techniques at a micron level spatial resolution [193, 194]. This method does not require any time-consuming specimen preparation and allows many scans of the same specimen under different conditions to be made. The technique is complementary to higher resolution 2D microscopy and lower resolution 3D ultrasonic imaging. Primarily, X-ray tomography is commonly used for medical application but in the recent decade it was employed as a tool for the microstructural studies of ceramics [195], foams [196] and alloys [197].

Specimens for CT were directly cut from the strip without any additional preparation. Series of 2D X-ray absorption images were recorded during rotation of the object with small angular steps. Projection images were captured and used for the generation of a three-dimensional digital image where each voxel (volume element) represents the X-ray absorption in this point [198]. Because of a relationship between X-ray absorption and material composition and density, the 3D internal structure can be derived and the resulting 3D images can be displayed as series of 2D 'slices' (Fig. 3.6).

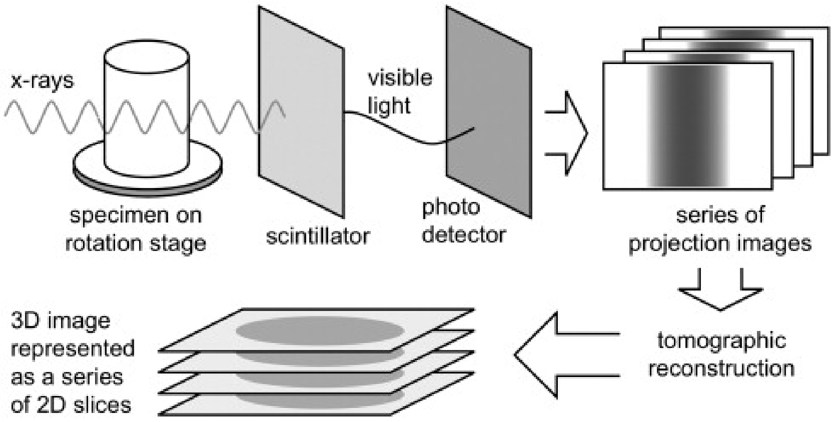

Figure 3.6: Schematic illustration of X-ray CT acquisition and reconstruction processes. The 3D map is typically presented as a series of 2D slice images [193].

For CT investigations [199] a Nanotom 180NF desktop device from General Electric with a 180 keV nano-focus tube with transmission target and external liquid cooling system for measurement stabilization and 2316 pixel × 2316 pixel Hamamatsu flat panel detector were used. Scan parameters were 95 keV with a 0.1 mm copper pre-filter and 223 μA. The achieved voxel size was 0.68 μm^3. For the image reconstruction the software Datos×2 reconstruction 2.2.1 was used in a combination with a 3×3 inline median filter and a beam hardening correction. VGStudio MAX 2.2 was used for visualization and evaluation. A 9 × 9 × 9 median filter was applied for the noise elimination. The surface near the examined region was excluded from evaluation in order to reduce the influence of artefacts. The advanced surface determination was used for the detection of particles with higher absorption, whereby the starting value of the surface determination was chosen to be $\mu + 3.5\sigma$. μ is an expected value of the Gaussian distribution from the material matrix and σ is the standard deviation.

3.8 Mechanical properties characterization

3.8.1 Microhardness measurements

Local mechanical properties of studied alloys were investigated using hardness measurements. Hardness is denoted as a resistance of the material to plastic deformation caused by indentation. Vickers hardness number (HV) was used in this study and was calculated according to Eq. (3.9):

$$HV = \frac{1.854 \times F}{D^2}, \tag{3.9}$$

where D is a length of the impression diagonal and F is a load in kilogram-force (kgf), which is a gravitational metric unit of force. During the Vickers microhardness testing a diamond indenter is impressed into the surface of the specimen. The indenter has a pyramidal shape with an angle between opposite sides of 136°. The indenter is pressed to the specimen with defined force and held for a certain time at this load. After this procedure a small square hole is left in the material. Dimensions of the indentation were measured as is shown in Fig. 3.7 by a LOM, which is an integral part of the QNess Q10A+ machine used for the testing.

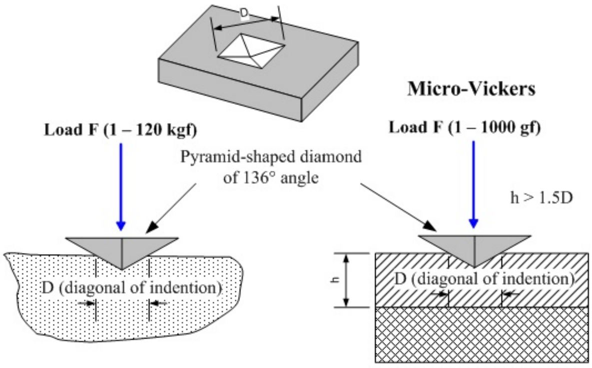

Figure 3.7: Illustration of the Vickers hardness method [200].

The microhardness testing allows quick and easy estimation of local mechanical properties of the material, e.g. ultimate tensile strength which linearly correlates with the HV value [201].

This method was applied to AZ31 magnesium alloys with the loading of 100 g and the load time of 10 s. Further in this work it is denoted as HV0.1. The same sample preparation as for LOM and SEM was used. Statistical measurements using at least ten indents were done. However, microhardness maps of the samples with heterogeneous microstructure were obtained with at least 300 points for areas with dimensions 5 mm × 8 mm. The accuracy of these measurements is approximately 5 HV0.1 depending mainly on the heterogeneity of the studied material. All measurements performed on TRC specimens were done in the TD.

3.8.2 Tensile tests

In order to investigate dynamic mechanical properties of as-cast samples and samples after heat and thermo-mechanical treatment tensile tests were performed.

One millimeter thick dog-bone shaped coupons were machined from both AC ingot and TRC strip for tensile tests. The TRC specimens had their tensile axes parallel to the RD and had a length of 5 cm as is shown in Fig. 3.8.

Influence of the strain rate on fracture was investigated during tensile tests with constants rates 10^{-1}, 10^{-2}, 10^{-3}, 10^{-4} s^{-1}. Moreover, effect of the annealing temperature on tensile properties was studied. The samples were annealed at 100, 150, 200, 250 and 300 °C before testing and held for 10 min at the given temperature. All deformation tests were conducted on INSTRON 5228 machine. At least 3 specimens of the same type were used for deformation to get appropriate statistics. Measured strain-stress curves were used do distinguish the 0.2 % yield stress and ultimate stresses.

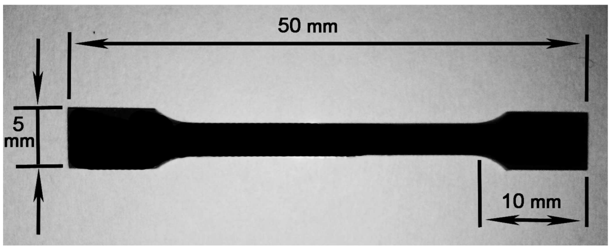

Figure 3.8: Dog-bone shaped specimen for tensile tests.

3.9 Thermo-mechanical processing

3.9.1 Equal-Channel Angular Pressing

ECAP was applied to AZ31 alloys in both ingot and TRC forms. Samples with dimensions 4.9 mm x 4.9 mm x 40 mm were cut from ingots and TRC strips. The TRC ones have their longer side parallel to the RD and TD as is shown in the Fig. 3.9, so that the pressing direction is perpendicular to the ND of the sample. The directions after ECAP are indicated as X, Y and Z. Two sets of samples were used for the ECAP processing: as-cast samples and samples pre-aged at 450 °C for 10 h in an air furnace and then quenched. Samples were deformed at 230 °C with a processing speed of 7 mm/min. The specimens were held at the processing temperature for 3 min before each pass. The angle of intersection between two channels was 90° and the route B_c was chosen for the deformation as it is shown in Fig. 1.8. It means, that the specimens were rotated by 90° along the X-axis before each pass [16]. Up to eight ECAP passes were used in order to achieve significant grain refinement. Each ECAP pass corresponds to an equivalent strain $\epsilon \approx 1$.

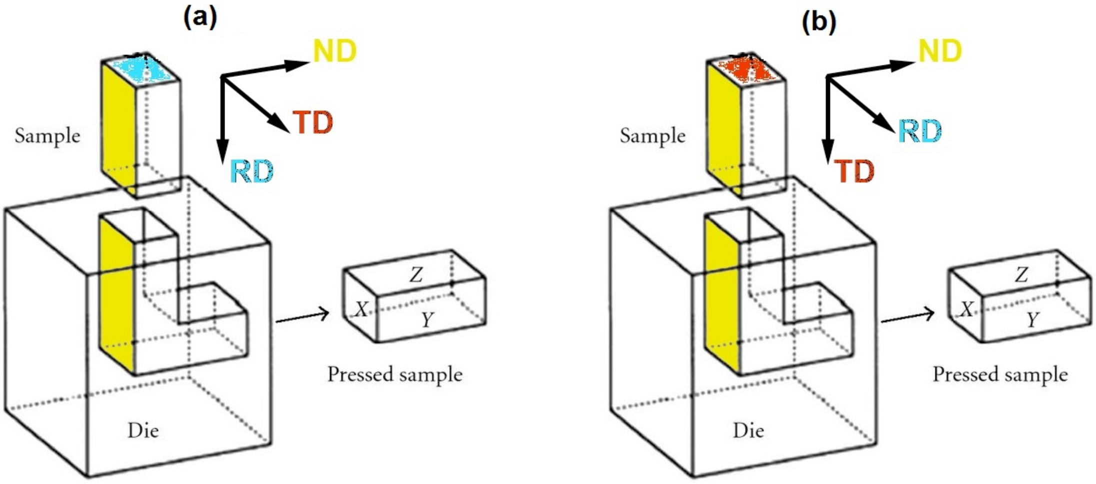

Figure 3.9: Illustration of the sample orientation during ECAP.

3.9.2 Constrained Groove Pressing

Constrained groove pressing (CGP) was applied to AZ31 thin plate cut from ingot and TRC strip. The plate had dimensions 70 mm × 50 mm × 5.6 mm. The CGP steps are shown in Fig. 1.9 and are as follows: (a) – a specimen is placed in the grooved die, (b) – groove pressing, (c) – flat pressing, (d) – the specimen is rotated by 180° along the pressing direction and (e) – the groove pressing stage is repeated, (f) – specimen is flattened again. Geometry of the die and grooves is illustrated in Fig. 3.10. During pressing the maximum load was 60 tons.

Pressings were held at RT with specimens preheated for 10 min at selected temperature. Specimens with rolling direction parallel to the grooves and preheated at 400 °C and 450 °C had visible cracks already after 1/4 of the CGP cycle (Fig. 3.11). On the other hand, specimens with TD parallel to grooves had satisfactory formability at 450 °C. Therefore, only these specimens at 450 °C were used for further CGP forming. Equivalent strain after one CGP cycle is equal to 1.16, which is slightly higher than the one after one ECAP pass.

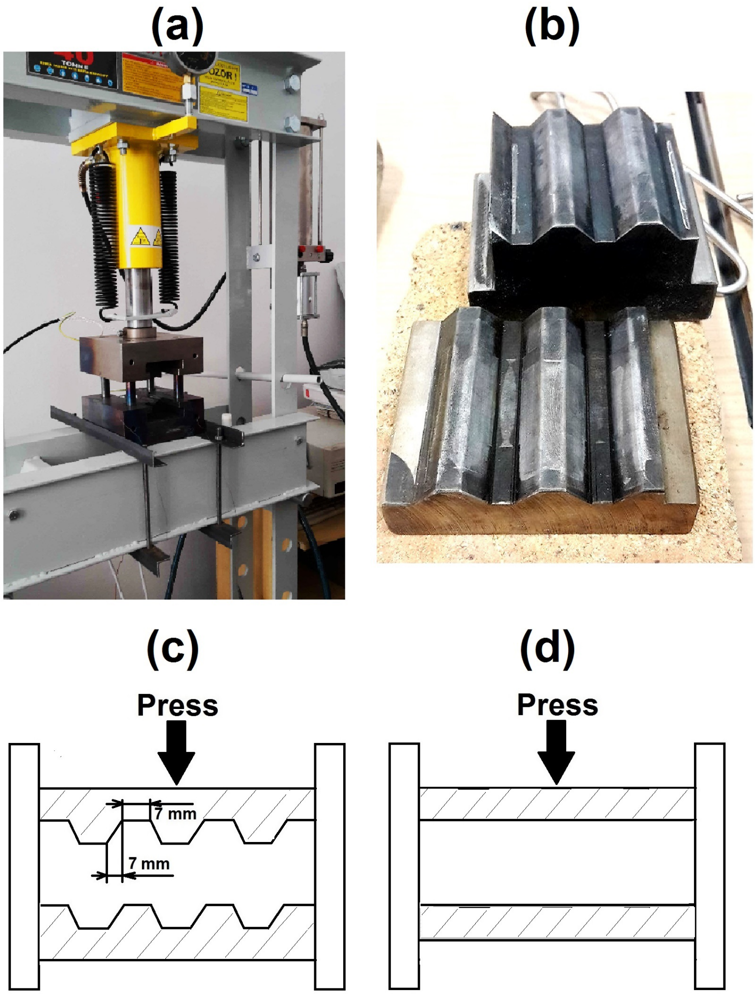

Figure 3.10: Illustration of the constrained groove pressing facility: a) pressing machine, b)grooves, c), d) geometry of the die and grooves.

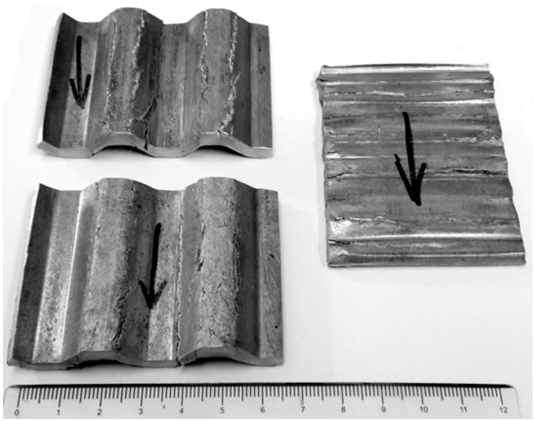

Figure 3.11: TRC samples subjected to 1/4 of CGP cycle, an arrow indicates the RD of the strip.

4. Results

Two sets of AZ31 samples prepared by conventional casting into an original ingot of the master alloy and by TRC were studied. The microstructure and local mechanical properties, such as microhardness, were defined using LOM, SEM, EBSD and Vickers microhardness testing. The effect of annealing and thermomechanical treatment on the microstructure was also studied. Texture and microstructural evolution during the processing were described.

4.1 As-cast materials

4.1.1 Light optical microscopy

The microstructure of AC and TRC AZ31 magnesium alloys are shown in Fig. 4.1 and Fig. 4.2 and 4.3, respectively. In the micrographs the lighter part represents the α-Mg matrix and the darker one corresponds to β-$Mg_{17}Al_{12}$ phase, which is usually present in AZ31 alloys.

The AC ingot of AZ31 alloy exhibits homogeneous microstructure with coarse grains of about 200 µm. Relatively large β-$Mg_{17}Al_{12}$ phases are located mainly inside the grains (Fig. 4.1).

Figures 4.2 and 4.3 show the microstructure of the TRC alloy. Casting leads to the formation of heterogeneous microstructure, so that the grain size varies from tens to hundreds micrometers. The observation of the surface microstructure and cross-sections of the samples in TD and RD was made. Fig. 4.2c shows well-developed dendrite structure on the surface of the strip. In the RD particular grains can be distinguished. An inhomogeneous distribution of grain size along the width of the strip is observed. Average grain size is 150 µm in the bulk of the material, 25 µm in the central part of the strip and about 60 µm near the surface of the strip. Nevertheless, strains induced during TRC lead to the formation of fine grains which are observed at the grain boundaries of the coarser grains (dark areas in Fig. 4.3c).

On the other hand, in the TD the microstructure reflects casting conditions

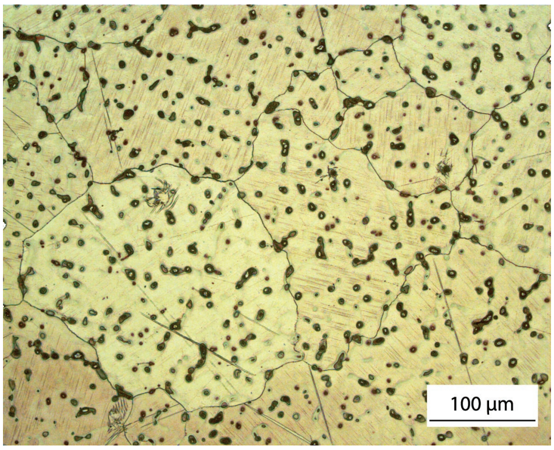

Figure 4.1: LOM image of the as-cast ingot of master AZ31 Mg alloy.

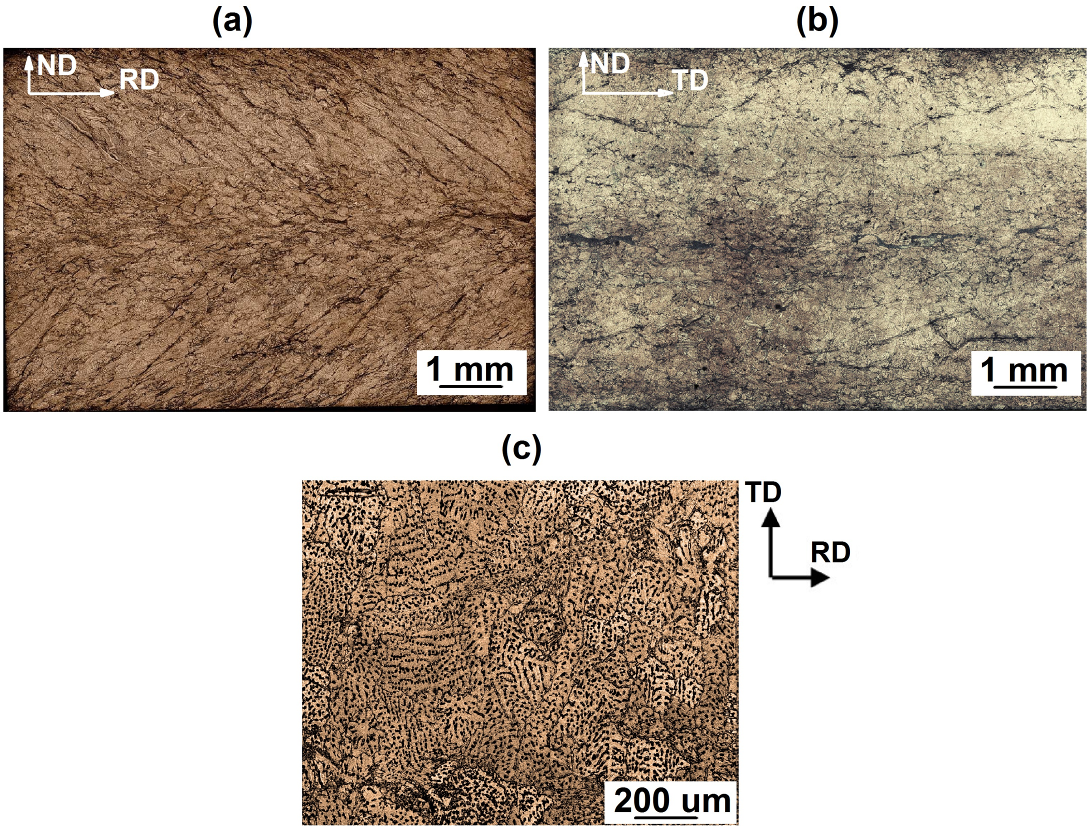

Figure 4.2: Light optical microscopy imaging of cross-sections of TRC strip in a) TD, b) RD and c) the surface of twin-roll cast AZ31 Mg alloy in ND.

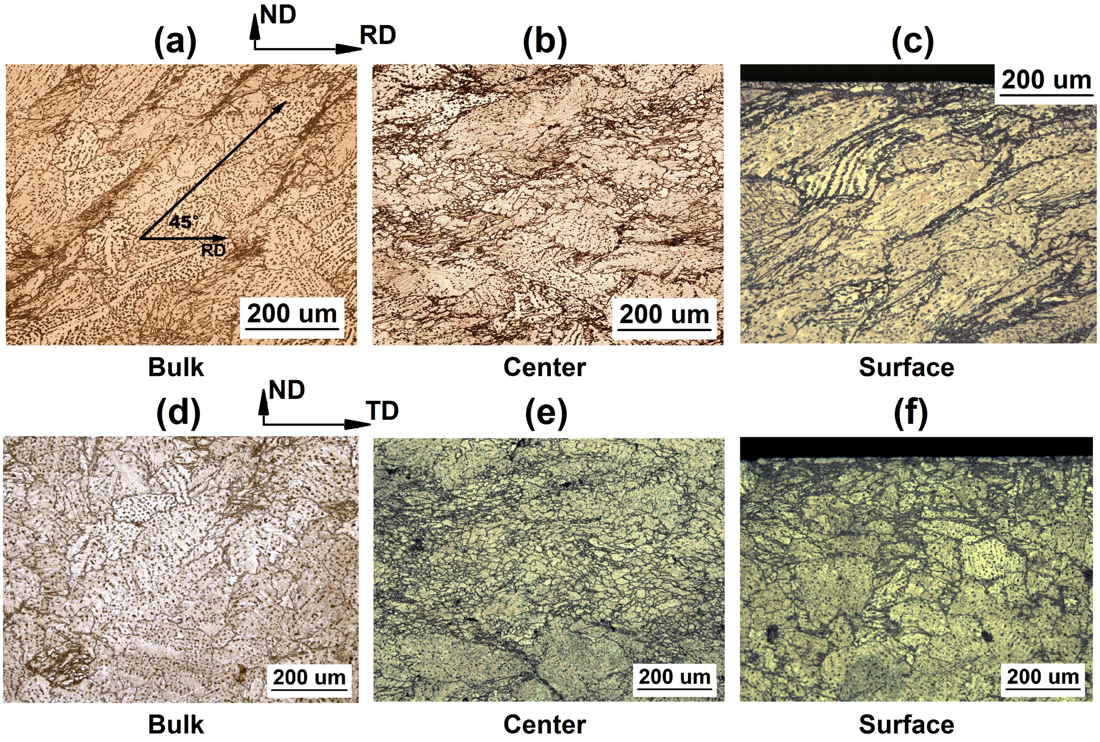

Figure 4.3: Light optical microscopy images of indicated parts of TRC AZ31 magnesium strip in a-c) TD and d-e) in RD.

more apparently. Large elongated grains with the grain size of about 200 µm are observed in the bulk of the strip as it is shown in Fig. 4.3a. Much finer grains of about 50 µm are formed in the middle of the strip and near its surface (Fig. 4.3b,c). In addition, the presence of grains of about 5 µm at the grain boundaries of coarser grains reveals visible bands tilted 45° towards the RD.

The β-particles are also distributed within the whole α-Mg matrix as in the conventionally cast alloy, however, they are much finer. Micrographs of polished surfaces displayed in three main directions are shown in Fig. 4.4. Coarse particles (marked by circles (a) and rectangle (b)) are distributed inside the Mg matrix with higher density in the central zone of the cross-section of the strip, spaced nearly equidistantly in the section perpendicular to RD with a distance of about 2 mm (Fig.4.4a). In sections perpendicular to TD (Fig.4.4b) no periodicity of the primary particle distribution is observed. Attempts to visualize segregated zones in sections perpendicular to ND failed because a well-developed dendrite structure typical for these types of alloys reduces the visibility of segregated particles on sections prepared from the central area of the strip (Fig.4.4c). Thus, the shape and distribution of these particles in this direction is not clear.

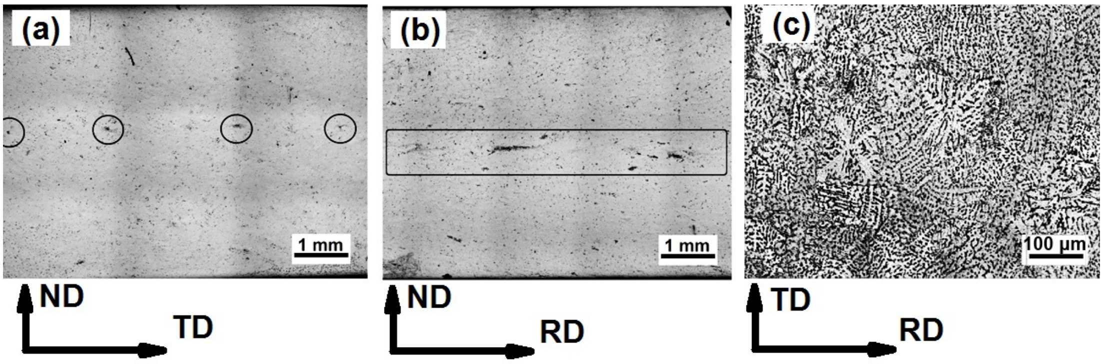

Figure 4.4: Micrographs of the TRC alloy showing the distribution of primary particles along the strip in a) RD, b) TD and c) ND.

4.1.2 Scanning electron microscopy

Fig. 4.5 shows BSE images of the TRC sample in sections perpendicular to three casting directions. In RD (Fig. 4.5a) the periodicity of coarser primary particles in the center of the strip found by LOM is confirmed, while in TD and ND sections (Fig. 4.5b,c) segregated channels elongated in the RD appear.

A more complex sample preparation, namely removing of the upper half of the strip and imaging of only a central part of the strip in the ND results in an incomplete mapping of the segregation inside the specimen (Fig. 4.5c) because the thickness of the center line segregation does not exceed 50 µm and, therefore, is often removed during polishing. Moreover, as it is shown in Fig. 4.4a,b segregated particles are located not exactly at the center of the strip but their position varies along the strip length which makes the observations in ND statistically less compliant.

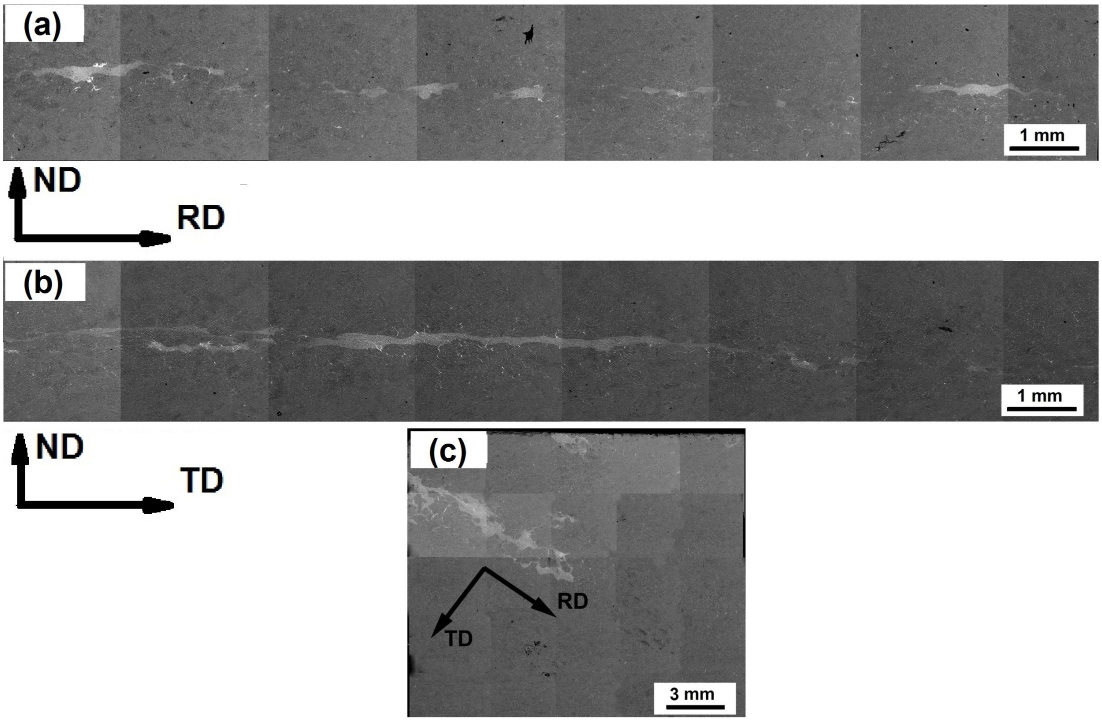

Figure 4.5: Back scatter electron images of the central region of the TRC strip in a) TD, b) RD and c) ND.

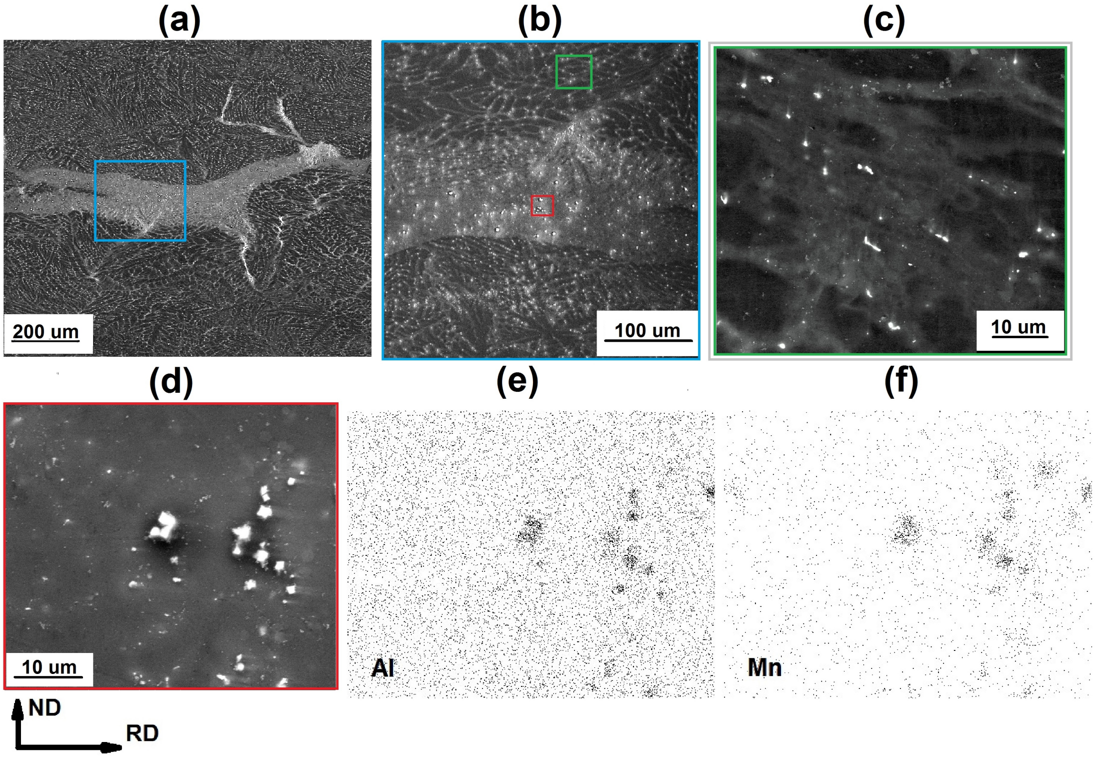

Figure 4.6: SEM images of the central region of the as-cast AZ31 magnesium alloy: a), b) BSE image of a "deer-shaped" segregation in the center of the strip, c) BSE imaging of dendrite arms and Al-Mn intermetallic particles, d), e) SE maps of Al and Mn collected from the region from Fig. d).

Nevertheless, SEM allows the identification of the composition of secondary particles using EDS. Fig. 4.6 shows SEM images of the central zone viewed in TD. A "deer-shaped" area of the CLS is illustrated in Fig. 4.6a. A detailed view of the CLS and analysis of a dendrite structure are shown in Fig. 4.6b,c. EDS of an area marked by a green box shows that it consists mainly of β-$Mg_{17}Al_{12}$ primary particles that can be dissolved during annealing at temperatures above 440 °C [5]. An image of the area marked by a red box is shown as Fig. 4.6d and contains coarser particles. Figures 4.6e,f show that mainly aluminum and manganese from thermally very stable intermetallic compounds Al_8Mn_5 and $Al_{11}Mn_4$ [202] are present in this region.

The SEM technique is irreplaceable for the identification of the composition of primary phase particles, however the collected information does not provide a 3D insight of the distribution of particles in the volume of the strip after casting.

4.1.3 X-ray microtomography

Since it is known from the literature [25, 81] that the CLS can affect mechanical properties of the Al containing Mg alloys, the more detailed investigation of the formation geometry of CLS was performed using X-ray tomography. The size and composition of the segregated particles can influence the mechanical behavior during the deformation and lead to a poor ductility. In this study X-ray tomography was for the first time used for the investigation of the CLS in a TRC AZ31 magnesium alloy strip. Results in a form of 3D reconstructed patterns of secondary phase particles in the central region are shown in Fig. 4.7.

The information about the distribution of primary particles is more complex than the data obtained by LOM and SEM. Much larger area of the specimen is scanned by this method (10 mm × 10 mm × 5.6 mm). The periodicity of segregation lines is clearly visible in Fig. 4.7a,c,d while this information is missing in SEM and LOM. The distribution in TD is homogeneous along the strip (Fig. 4.7b). The passes of primary particles in the center of the strip are formed after the TRC in the direction of rolling. The distance between these segregation lines is about 2 mm and corresponds to LOM observations. Fig. 4.7d shows that the distribution of primary intermetallic particles is not homogeneous along the RD and the width of the passes varies from one to five millimeters.

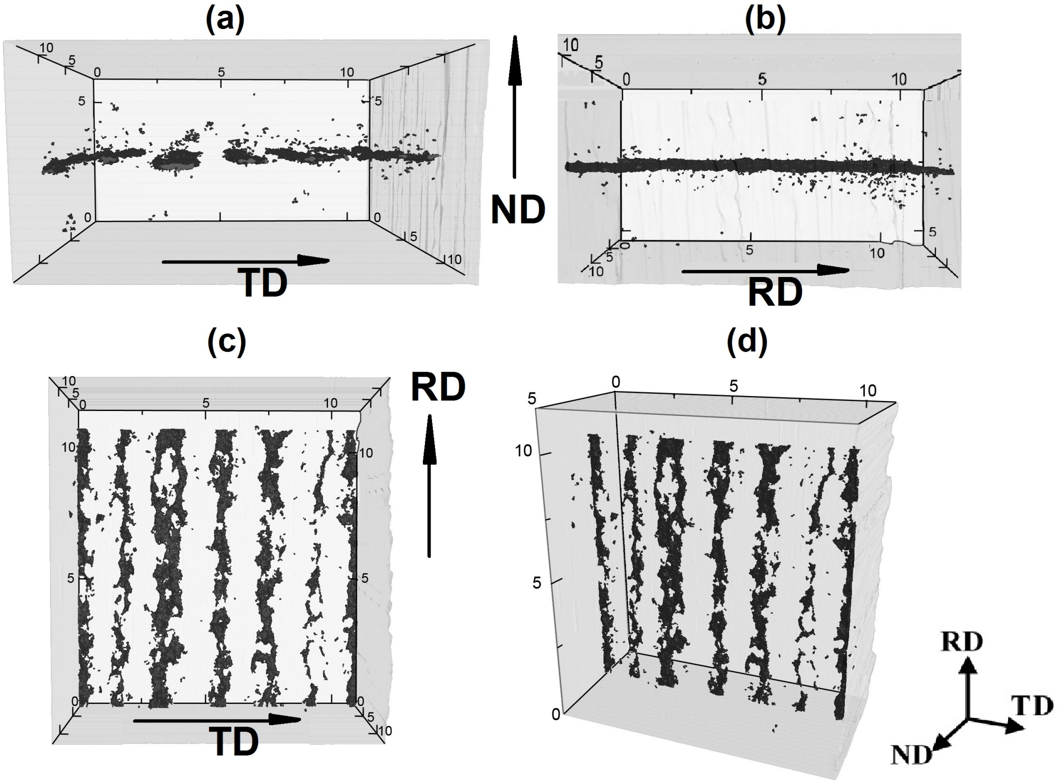

Figure 4.7: X-Ray microtomography 3D reconstructed patterns of central segregation in TRC AZ31 magnesium alloy in different perspectives: a) RD, b) TD, c) ND and d) general view. Scale is represented in millimeters.

4.1.4 Electron back scatter diffraction

Heterogeneous microstructure of TRC strip was also studied using EBSD mapping of an 1000 µm × 1200 µm area. The microstructure varies along the strips width in ND, therefore, selected 150 µm × 150 µm areas marked in Fig. 4.8a were subjected to a detailed scanning. These areas are designated as follows: 1 – upper part of the bulk of the sample, 2 – center of the strip, 3 – lower part of the bulk. Such designations will be used in the following text. Corresponding PF are present in Fig. 4.8b. The average texture of the strip in TD direction exhibits strong basal nature. However, a rotation of the most intensive peaks in regions (1) and (3) by about 30° from the ideal orientation is observed (Fig. 4.9a,b). Elongated grains are observed in these areas. Central region (2) with smaller grains is characterized by a strong basal texture similar to the average one in the the whole TRC sample. EBSD analysis show that grains have two prevailing orientations, namely, $\{0001\}\langle 11\bar{2}0\rangle$ and $\{2\bar{1}\bar{1}0\}\langle 10\bar{1}0\rangle$ seem to be preferable textures after TRC. The maximum intensity of the texture components in the cross-section region is no more than 3 r.u.(relative units) as indicated in Fig. 4.8.

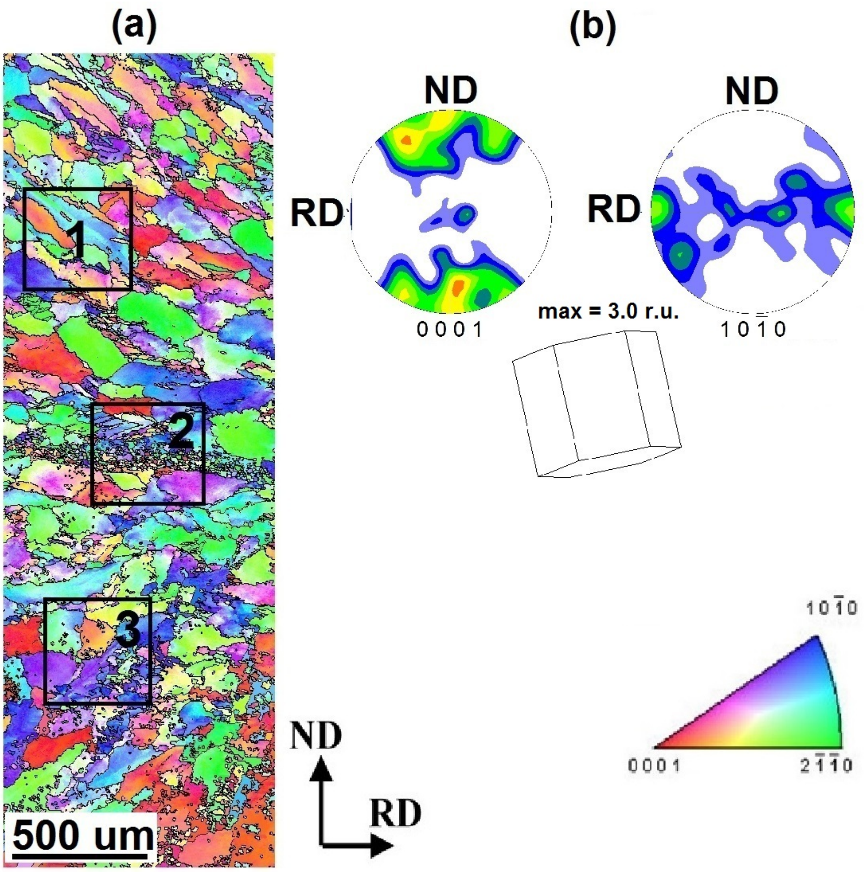

Figure 4.8: EBSD map (a) and 0001 and $10\bar{1}0$ pole figures of TRC strip (b) (schematic drawing shows a prevailing crystal orientation).

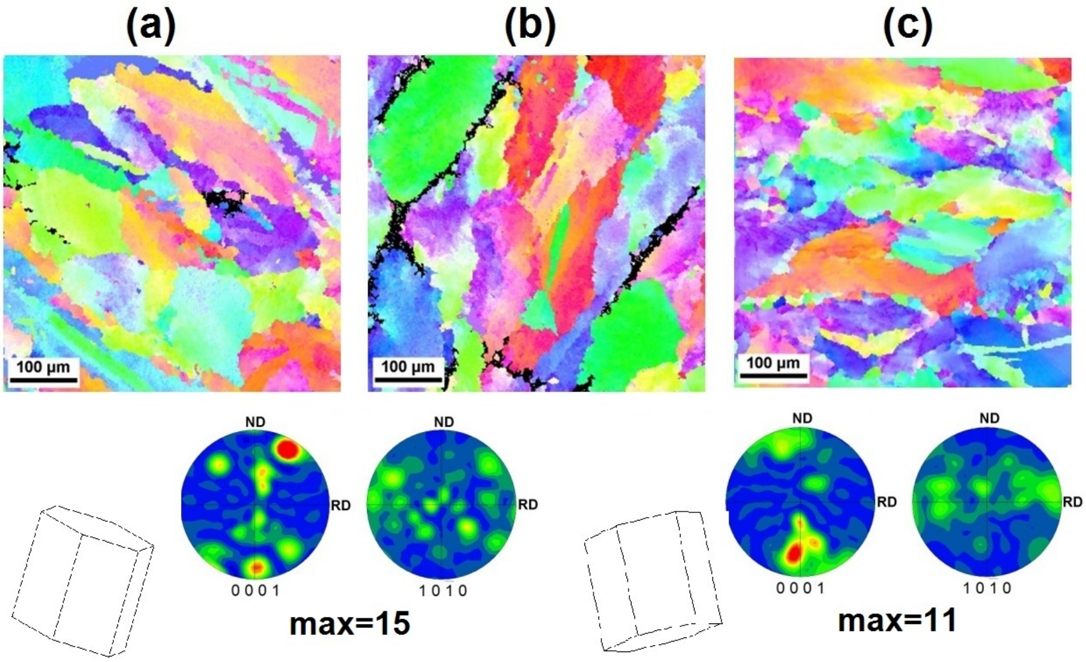

Figure 4.9: EBSD orientation maps and 0001 and $10\bar{1}0$ pole figures of the selected regions of TRC strip: a) 1 - upper part of the bulk of the sample, b) 3 - lower part of the bulk, c) 2 - center of the strip in the TRC alloy (schematic drawing shows a prevailing crystal orientation).

4.1.5 Microhardness testing

Microhardness mapping of the AC AZ31 magnesium alloy shows a more-or-less homogeneous distribution of the hardness along the specimen cross-section (Fig. 4.10a). The average value of the microhardness in the as-cast ingot is 50 HV0.1.

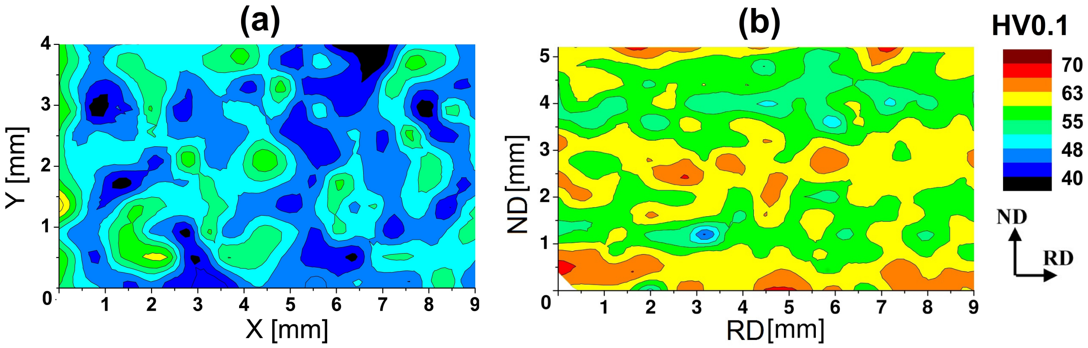

Figure 4.10: Vickers microardness maps of a) AC and b) TRC alloys.

On the other hand, the specific microstructure of TRC alloy with different sizes and orientations of grains affects the local mechanical properties. Vickers testing has revealed a heterogeneous distribution of the microhardness along the ND section of the TRC specimen. Different microhardness values in the center of the strip and near the surface are detected as it is shown on the map in Fig. 4.10b. The material is harder near the surface and in the central zone of the strip (63 HV0.1) and is slightly softer in the bulk of the specimen(58 HV0.1).

4.2 Annealed materials

4.2.1 Electrical resistivity

The resistivity of the samples was measured in a liquid nitrogen during step-by-step annealing with a step of 20 °C up to 560 °C. The results are shown in Fig. 4.11. At about 150 °C the drop of the resistivity is observed in both AC and TRC samples. In the AC specimen the electrical resistivity decreases till 380 °C, while in the TRC material a first increase of resistivity is observed already at 280 °C. In the TRC material a plateau is observed between 360 °C and 480 °C, followed again by a resistivity growth. On the other hand, only a continuous growth of resistivity is observed in AC specimen above 360 °C.

In order to eliminate the influence of primary β-$Mg_{17}Al_{12}$ particles on resistivity the homogenization annealing was performed at 450 °C for 10 h. The resistivity curves for AC and TRC materials after homogenization are marked in Fig. 4.11 by green and red lines, respectively. No significant changes in resistivity are observed in both materials till 420 °C, except for a slight growth in a temperature range between 280 and 300 °C. However, at 460 °C the resistivity growth is more pronounced.

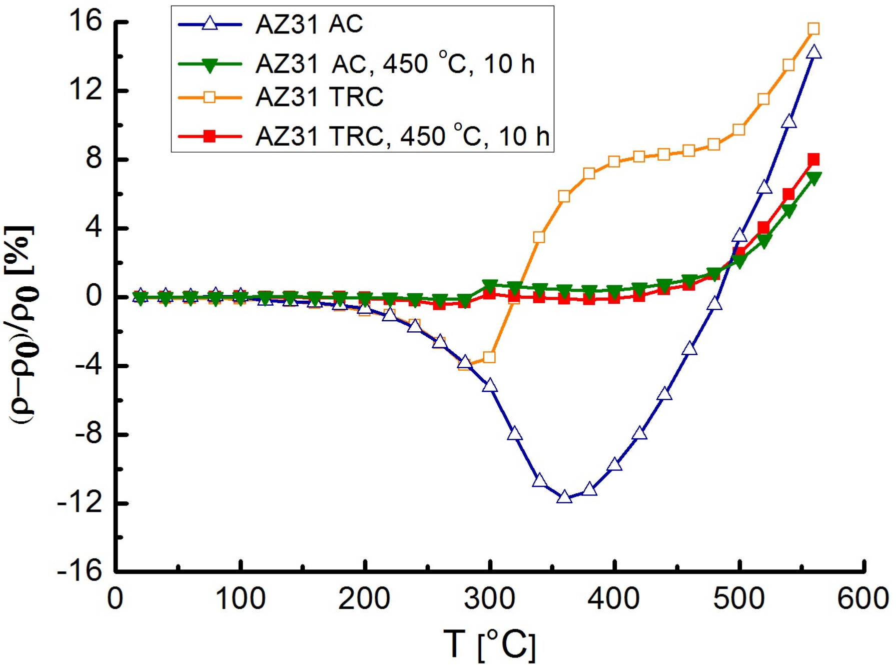

Figure 4.11: Evolution of resistivity during step-by-step annealing.

4.2.2 Light optical microscopy

The microstructural evolution was studied in specimens annealed to temperatures reflecting changes in electrical resistivity. Materials were annealed up to 250, 350, 400 and 450 °C with annealing rate of 1 °C/min. In addition, a thermal stability was studied using aging at 450 °C for time intervals ranging from 10 min to 24 h.

Fig. 4.12 shows the microstructure evolution during annealing. At 250 °C β-$Mg_{17}Al_{12}$ phase particles further grow at grain boundaries (Fig. 4.12a). At higher annealing temperatures, namely, at 350 and 400 °C, the β-phase dissolves and only few β-phase particles were observed after annealing at 450 °C (Fig. 4.12b-g). After aging at 450 °C for 10 h (Fig. 4.12d,g) almost full dissolution of the β-phase particles occurs and aluminium content is distributed throughout the matrix. An initial average grain size of about 200 µm remains almost unchanged after all steps of the heat treatment.

Fig. 4.13, 4.14 show the microstructural evolution of AZ31 TRC magnesium alloy strip observed in TD during annealing. Linear annealing up to 100 °C does not lead to any significant changes in microstructure when compared to TRC alloy. A slight annihilation of shear bands formed during casting is observed. With an increasing temperature up to 250 °C the gradually refining of β-phase particles in TRC material is detected. At 350 °C (Fig. 4.13d) the dissolution occurs, so that almost no β-phase particles are observed either inside grains or at grain boundaries. Moreover, the recrystallization of the material starts at this temperature. New finer grains appear at grain boundaries of the TRC alloy. Further growth of these grains occur at higher temperatures as is shown in the Fig. 4.13e. The homogenization of the structure occurs after 10 h of annealing at 450 °C (Fig. 4.13f). A significant grain refinement is observed. The average grain

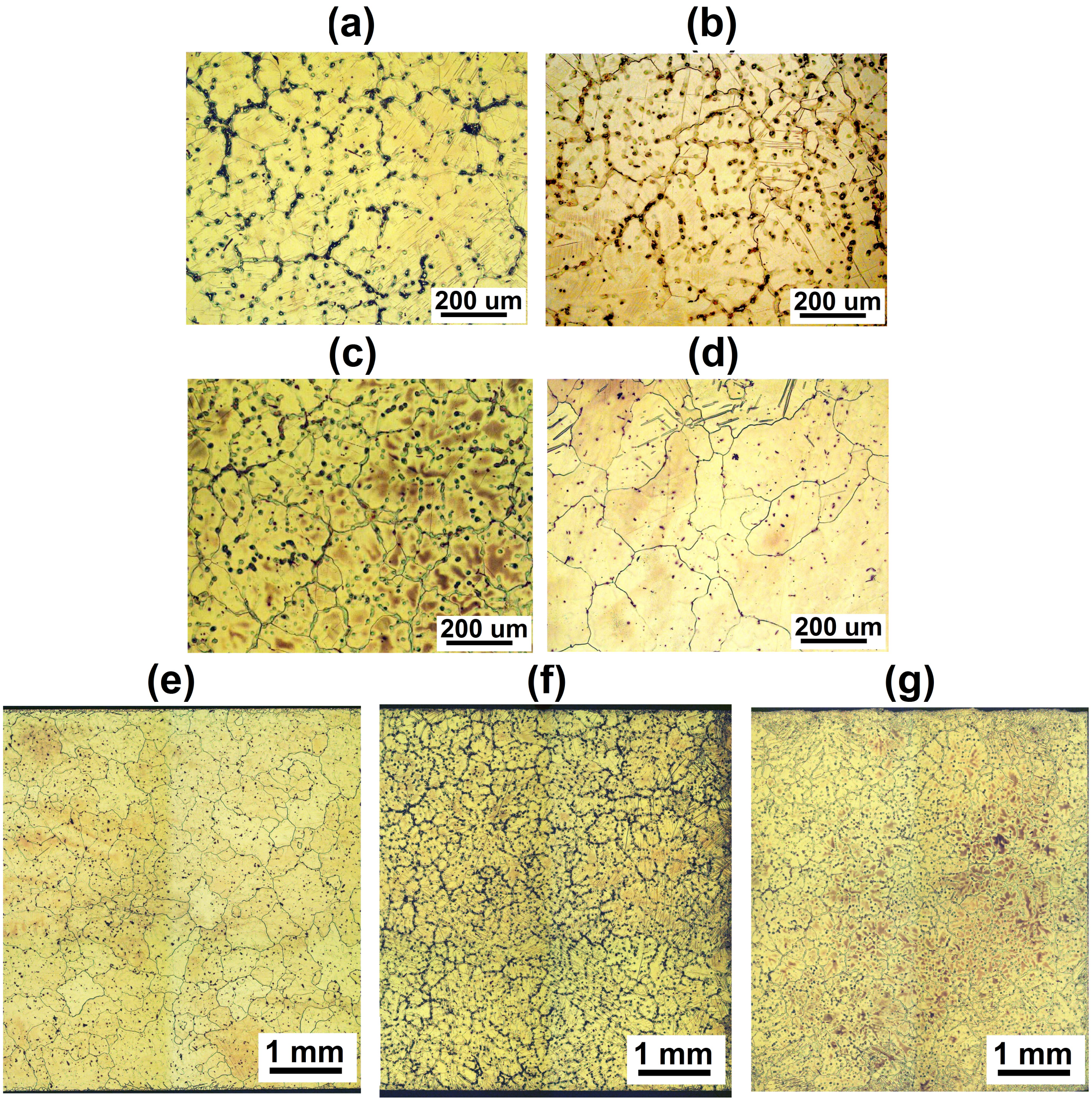

Figure 4.12: Evolution of the microstructure of AC AZ31 magnesium alloy during annealing up to: a) 250 °C, b) 350 °C, c), f) 400 °C, d), g) 450 °C for 10 h and e) cross-section of AC alloy before annealing.

size in the alloy after aging is about 50 µm, which is about four times smaller than the grain size in the TRC strip. When compared to the AC ingot of a master alloy TRC alloy aged at 450 °C for 10 h exhibits more homogeneous structure with finer grains without any presence of β-phase particles.

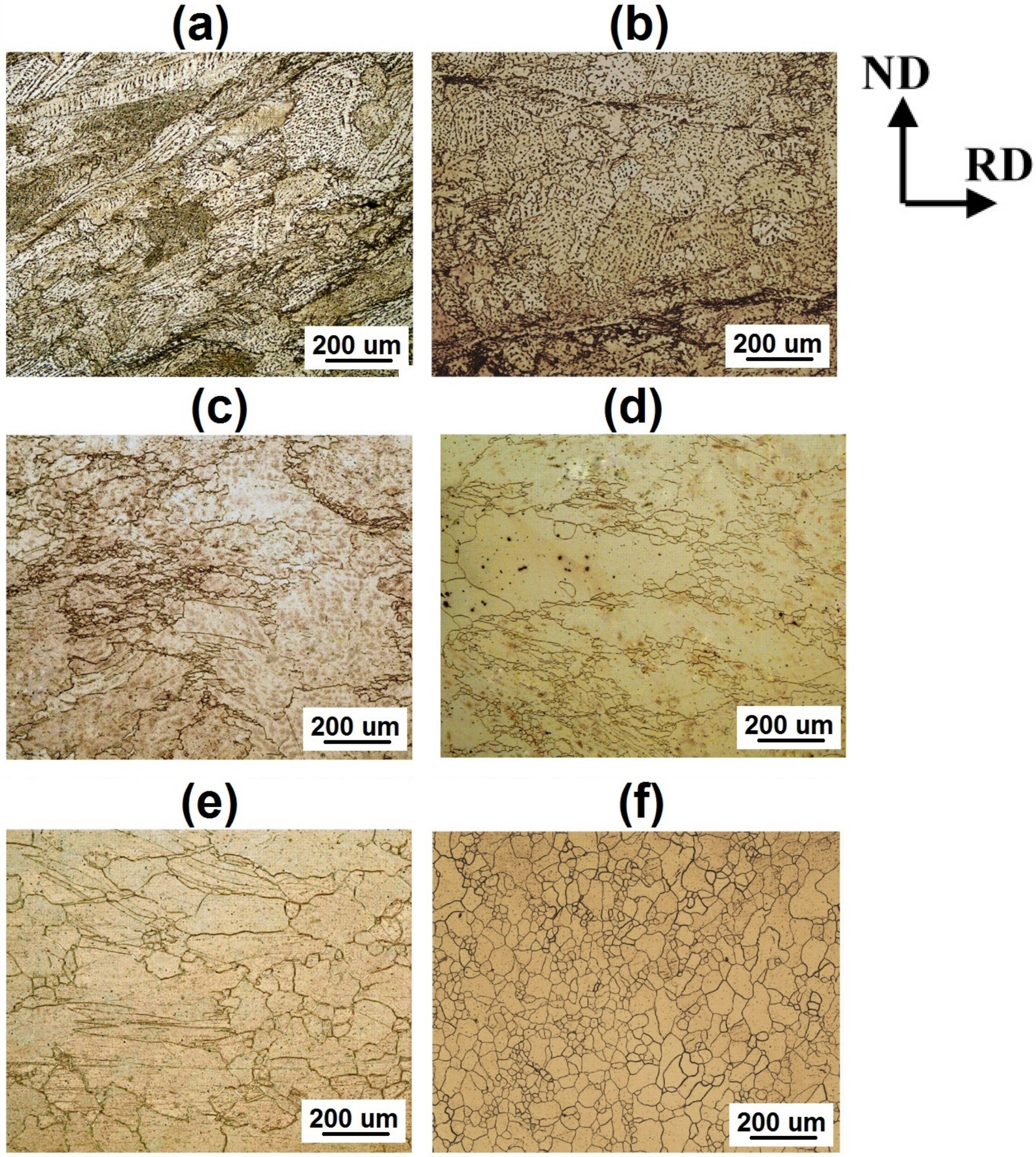

Figure 4.13: LOM micrographs of the bulk region of the TRC AZ31 strip in TD during annealing up to: a) 100 °C, b) 250 °C, c) 300 °C d) 350 °C, e) 400 °C, f) 450 °C for 10 h.

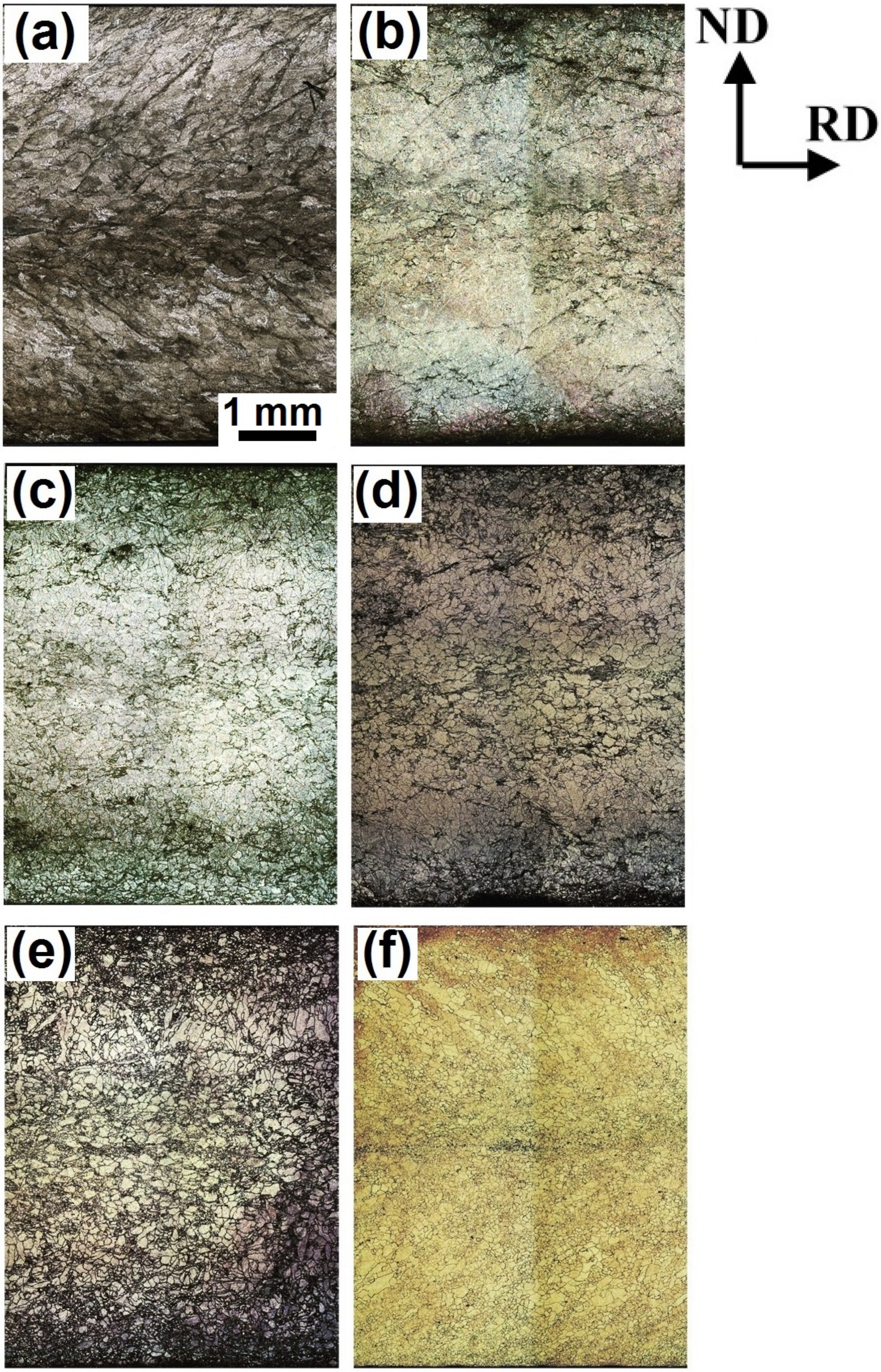

Figure 4.14: Cross-section of the TRC AZ31 strip in TD during annealing up to: a) 100 °C, b) 250 °C, c) 300 °C d) 350 °C, e) 400 °C, f) 450 °C for 10 h.

Thermal stability

Several aging time intervals were chosen to study thermal stability of the TRC strip at relatively high annealing temperature (450 °C). Fig. 4.15 shows the resulting microstructures of the cross-sections of the strip.

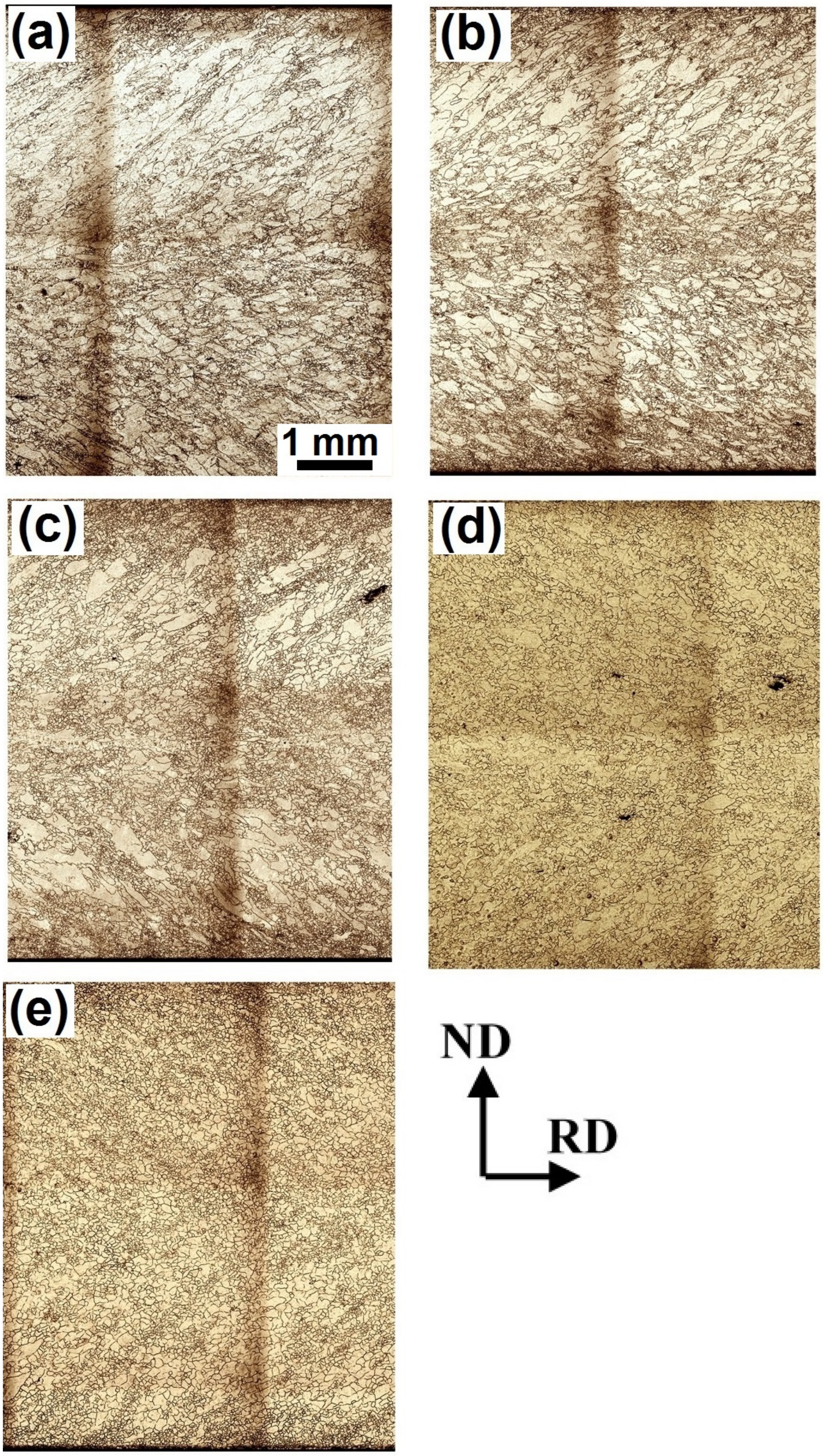

Figure 4.15: Thermal stability of the TRC alloy annealed at 450 °C: a) 10 min, b) 80 min, c) 160 min, d) 6 h and e) 24 h.

Aging for 10 min leads to a nucleation of new fine grains at original grain boundaries (Fig. 4.15a). After annealing for 80 min and 160 min a slight coarsening of nucleated grains is observed (Fig. 4.15b,c). After 6 h of aging the microstructure is almost fully recrystallized with an average grain size of about 70 µm. Full recrystallization of the structure and dissolution of secondary particles occurs after longer aging periods (Fig. 4.14f). No significant grain growth was revealed even after 24 h of aging.

Additional investigation of microstructure changes after aging at lower temperature (300 °C) and at extremely high temperatures (500 °C) was performed. Micrographs of resulting microstructures are shown in Fig. 4.16. Long-term aging at 300 °C results in a formation a a coarse-grained microstructure. Homogeneously distributed elongated grains are observed. Their average grain size is about 300 µm. Moreover, nearly no formation of new grains at grain boundaries is observed.

On the other hand (Fig. 4.16b), short aging at 500 °C creates very small grains (10 µm) with homogeneously randomly distributed coarser grains of the size of 50µm.

It should be also mentioned that the CLS is still present in all samples after heat treatment.

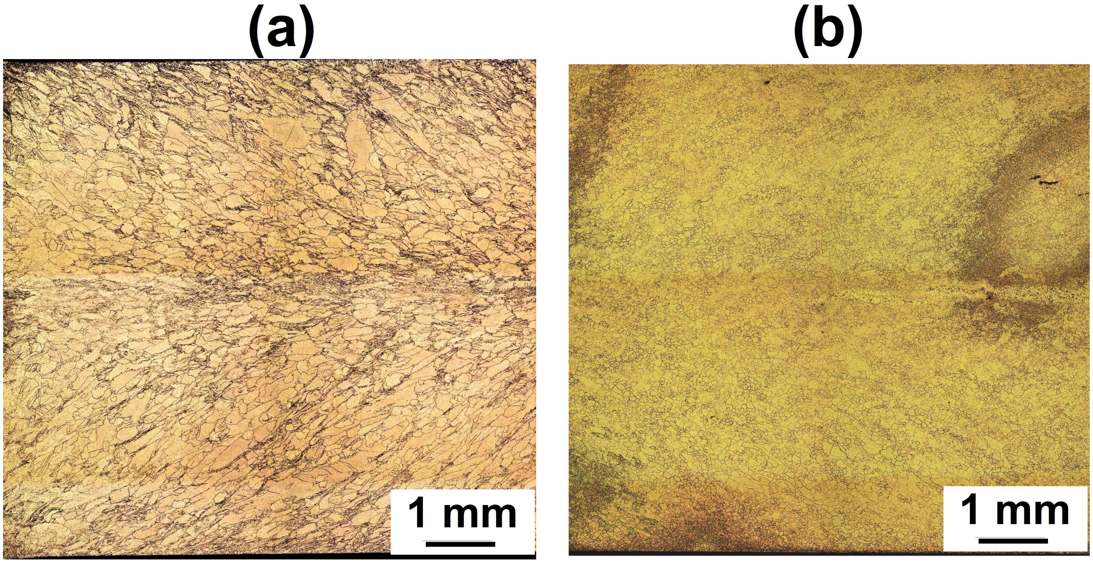

Figure 4.16: Microstructure of TRC alloy aged at: a) 300 °C for 7 days and b) 500 °C for 40 min.

4.2.3 Scanning electron microscopy

Fig. 4.17 shows the BSE images indicating the processes ocurring in TRC sample during annealing. The TRC strip has a strongly developed dendrite structure (dendrite arms are marked by red arrows) and Al-Mn intermetallic particles homogeneously distributed in the α-Mg matrix (marked by yellow arrows). This was also shown previously using SEM studies of TRC samples in Fig. 4.5 and 4.6. After annealing at 250 °C no changes in the microstructure are detected. At 300 °C a broadening of the dendrite arms occurs. Further annealing up to 350 °C leads to a remarkable increase of DAS and further broadening of persisting dendrite arms. At 400 °C β-$Mg_{17}Al_{12}$ phase is fully dissolved and a partial dissolution of Al-Mn particles after aging at 450 °C for 10h is observed.

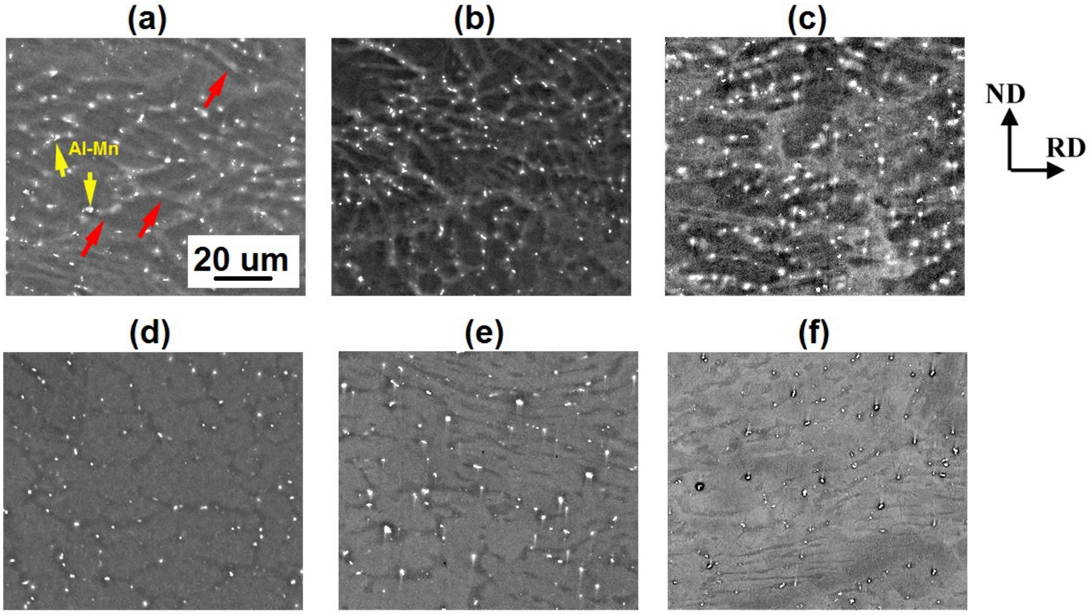

Figure 4.17: Evolution of the microstructure of TRC AZ31 magnesium alloy strip in TD during annealing observed using back scatter electron imaging: a) as-cast, b) 250 °C, c) 300 °C d) 350 °C, e)400 °C, f) 450 °C for 10 h.

4.2.4 Electron back scatter diffraction

EBSD orientation maps were obtained on TRC samples after homogenization at 450 °C for 10 h. Fig. 4.18 shows elimination of strains inside grains and recrystallization. Elongated grains in the regions 1 and 3 observed in as-cast samples (see Fig. 4.8) are no more present after this treatment. Very similar texture was observed in all regions (1-3), thus, homogenization heat treatment leads to the balancing of the texture along the cross-section of the TRC material.

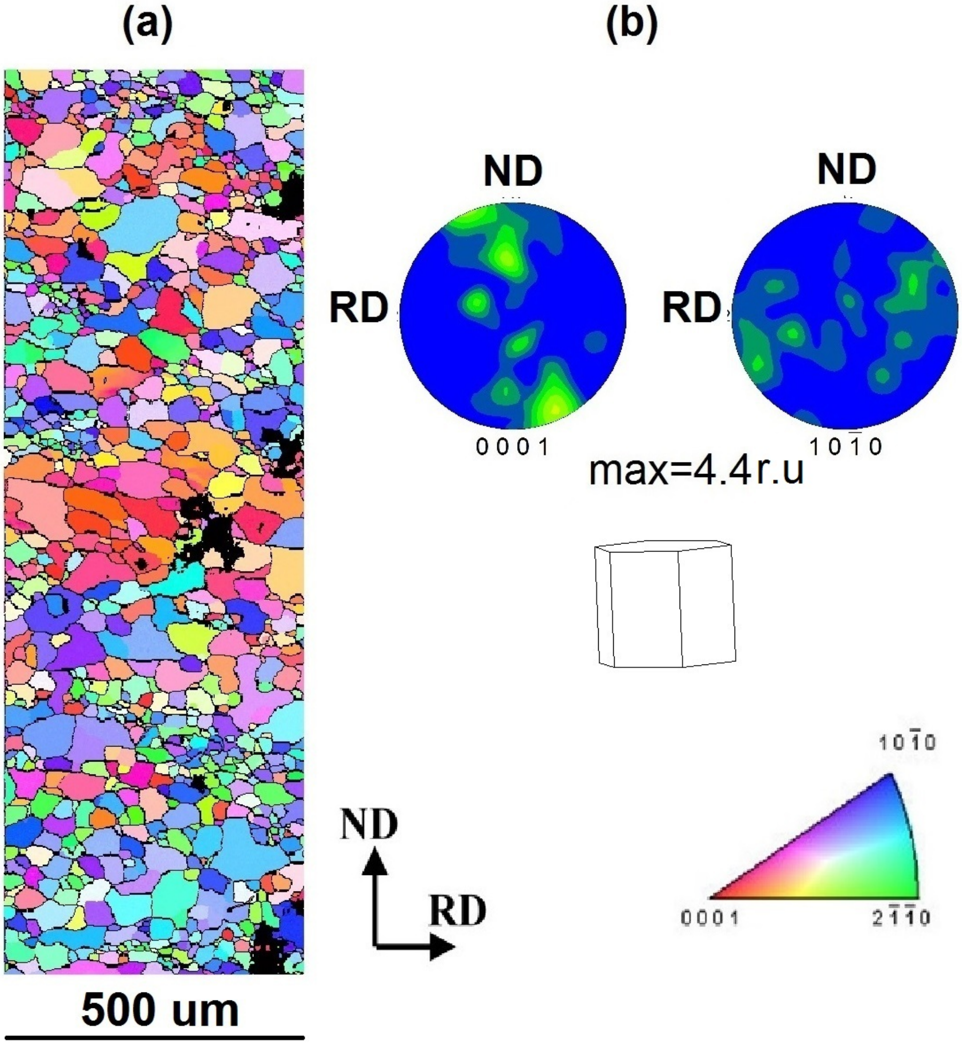

Figure 4.18: EBSD map (a) and 0001 and $10\bar{1}0$ pole figures (b) of TRC strip annealed at 450 °C for 10 h (schematic drawing shows a prevailing crystal orientation).

4.2.5 X-ray diffraction

In order to compare results obtained from EBSD with the ones received from XRD, we used PF measured in the region marked as 1 (see Fig. 4.8). Fig. 4.19 shows the results for the as-cast and homogenized TRC materials, respectively. In the as-cast specimen two intensive areas (Fig.4.19a) in the 0001 XRD PF were observed. They correspond with two possible textures present in this region of the material. The EBSD measurements (Fig. 4.8) showed the same results.

After homogenization the strengthening of the basal $\{0001\}\langle 11\bar{2}0\rangle$ texture occurs (Fig.4.19b). However, grains with $\{1\bar{2}10\}\langle 10\bar{1}0\rangle$ orientation are still present.

Possible local inhomogeneity along the rolling direction which is often observed in TRC materials can cause slight disagreement in results obtained by the EBSD and XRD. The data show that for an improvement a plausibility of results more statistical measurements are necessary.

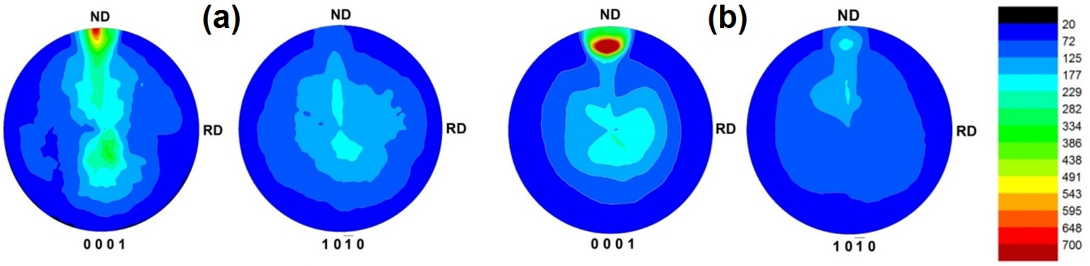

Figure 4.19: 0001 and $10\bar{1}0$ PF of the bulk area of AZ31 TRC strip measured by XRD in: a) as-cast and b) homogenized states.

4.2.6 Microhardness testing

The microhardness mapping was performed on samples after annealing. Results are summarized in Fig. 4.20 and 4.21. In AC alloy a slight decrease of microhardness after homogenization to 45 HV0.1 is observed. However, this decrease is still within the experimental error of this method.

First annealing at 100 °C surprisingly results in a subtle increase of a microhardness (compare with Fig. 4.10) The microhardness mapping of TRC specimens after annealing shows a partial softening of central and surface regions at 250 °C and 300 °C. At 350 °C more homogeneous distribution of HV0.1 values is present, however harder regions still persist. A further annealing up to 400 °C results in a significant softening of the whole material and more homogeneous distribution of microhardness. Thus, HV0.1 value decreases down to 55 HV0.1. Softening at 400 °C will be described in following paragraphs.

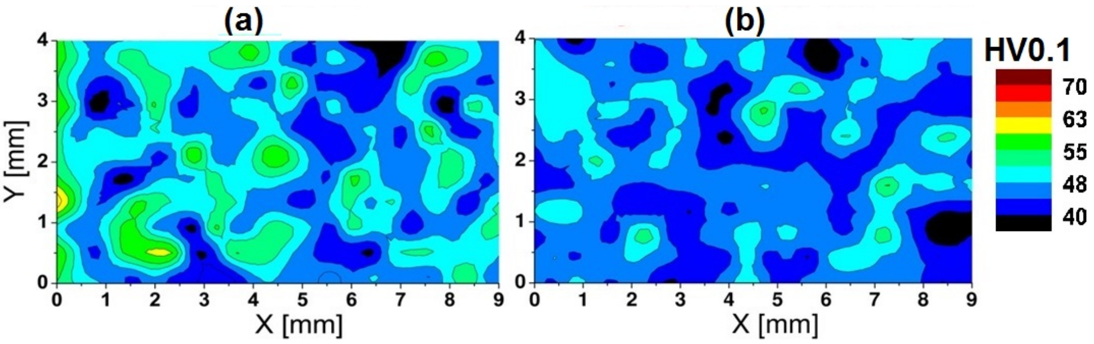

Figure 4.20: Microhardness mapping of AC AZ31 Mg alloy a) before and b) after aging at 450 °C for 10 h.

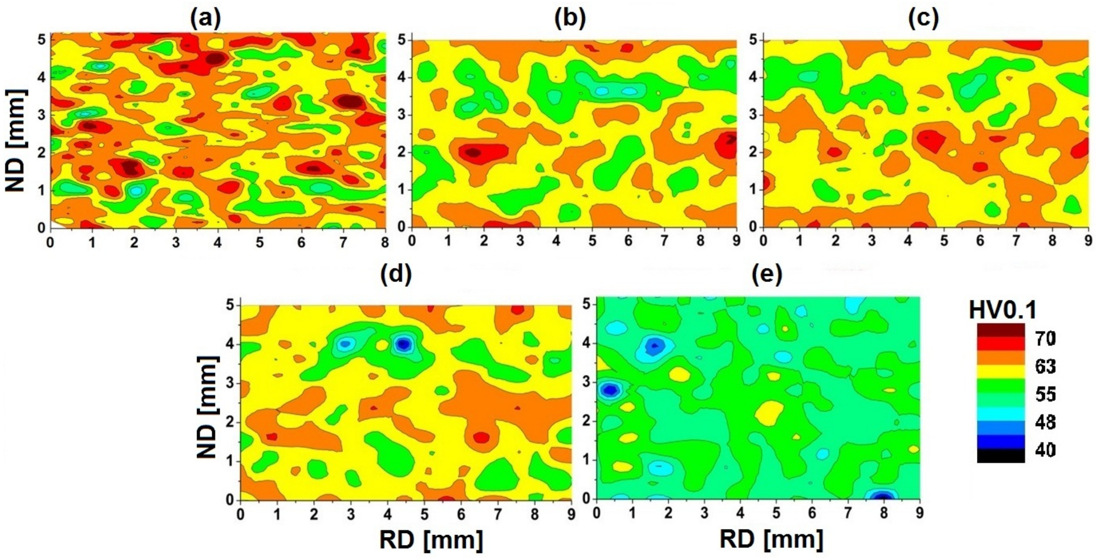

Figure 4.21: Microhardness mapping of TRC AZ31 Mg alloy after annealing at: a) 100 °C, b) 250 °C, c) 300 °C, d) 350 °C and e) 400 °C.

Fig. 4.22 shows the evolution of ingomogeneity along the ND of the TRC material. Obviously, a pronounced inhomogeneity with remarkably higher microhardness values in the center and the surface regions of the strip persists up to 350 °C. Further decrease of the microhardness occurs in two stages at 400 and 450 °C. Relatively large scatters are caused by the inhomogeneity of the TRC material along the RD.

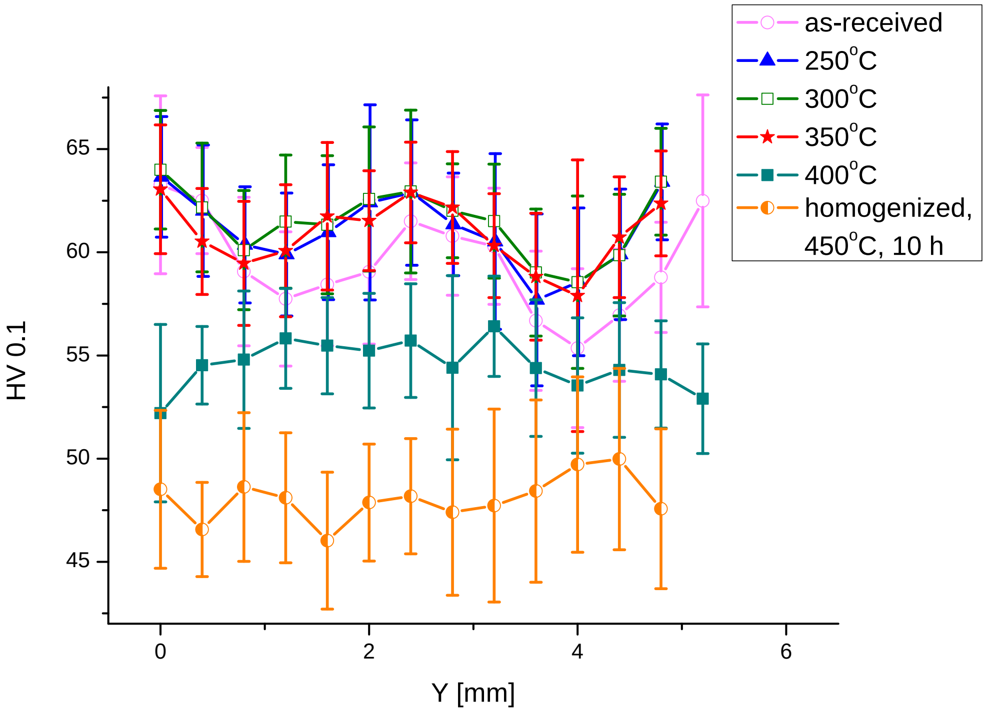

Figure 4.22: Distribution of microhardness of TRC alloy during annealing.

Fig. 4.23 illustrates microhardness changes during aging at 450 °C. A surprisingly significant hardening is observed after 10 min of aging (compare Fig. 4.23a with Fig 4.10). Nevertheless, average microhardness increases from initial 58 HV0.1 up to 65 HV0.1. Further aging results in a softening of the material down to 57 HV0.1 after 80 min and to 54 HV0.1 after 160 min, respectively. No remarkable changes of microhardness were observed after aging for 6 h. Although, a further drop of the microhardness to 47 HV0.1 occurs after 10 h of aging (value is comparable to the one observed in the AC material), after 24 h of aging at 450°C the microhardness again surprisingly increases to 51 HV0.1.

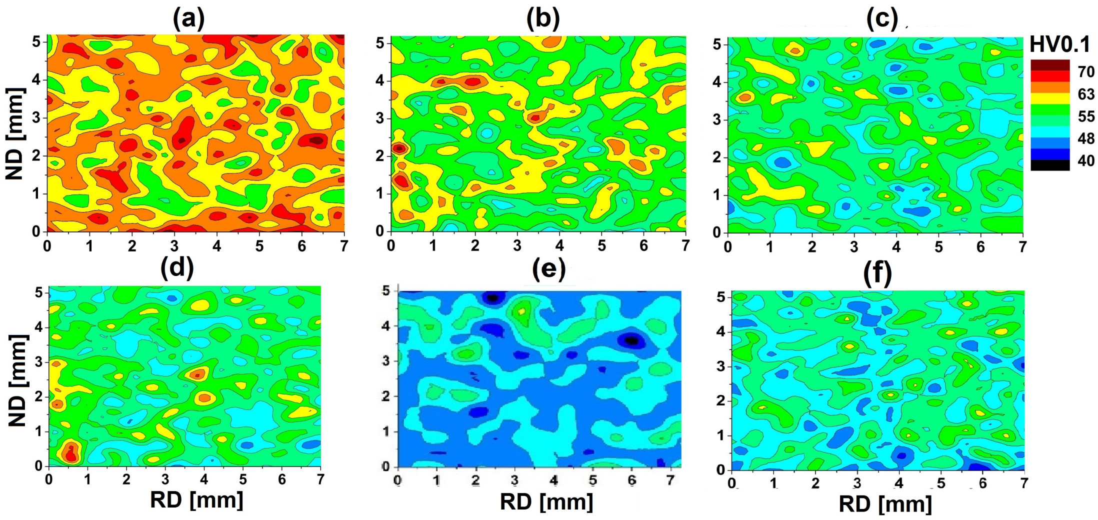

Figure 4.23: Distribution of microhardness of TRC alloy during aging at 450 °C for: a) 10 min, b) 80 min, c) 160 min, d) 6 h, e) 10 h and f) 24 h.

Additional HV mapping of TRC samples aged at 300 °C for 7 days and 500 °C for 40 min are displayed in Fig. 4.24. Long-term annealing at 300 °C increases the average microhardness to 61 HV0.1 while softening of the material to 51 HV0.1 is observed after aging at 500 °C. This value is similar to the one measured in the TRC sample after aging at 450 °C for 24 h.

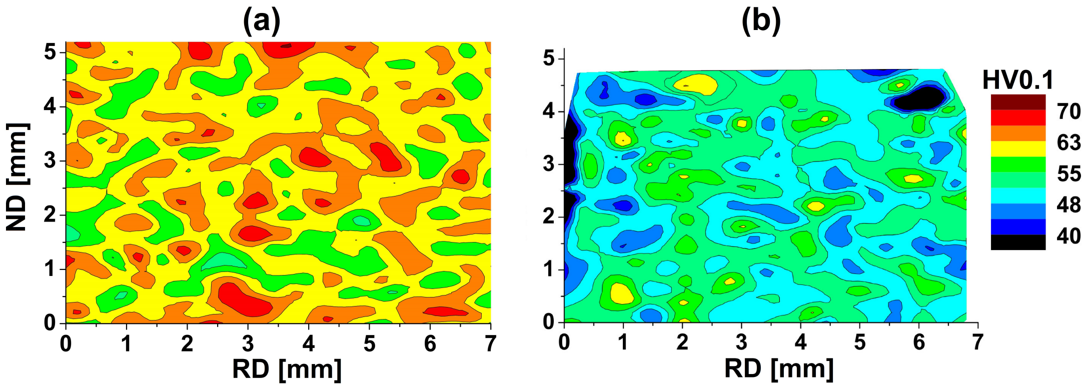

Figure 4.24: Vickers microhardness of TRC samples after annealing at a) 300 °C for 7 days and b) at 500 °C for 40 min.

4.2.7 Tensile tests

Tensile properties of AC and TRC AZ31 magnesium alloy were studied at RT and elevated temperatures. Figures 4.25 shows typical stress-strain curves of AC sample during straining at RT, 50, 100, 150, 200, 250, and 300 °C.

Elongation of AC samples increases with increasing temperature from RT to 150 °C. At 200 and 250 °C a slight decrease of ductility is observed. Further increase of the temperature up to 300 °C improves tensile properties and the ductility growth to 13 %. No improvement of mechanical properties after homogenization at 450 °C for 10 h are observed (Fig. 4.25b). On the contrary, a slight decrease od ductility is observed at all deformation temperatures. Similarly, as in as-cast material a decrease of ductility is observed at 150 °C and 200 °C. Also repeated experiments at 300 °C did not reveal the increase of the ductility. Also YS remains unaffected by the homogenization annealing.

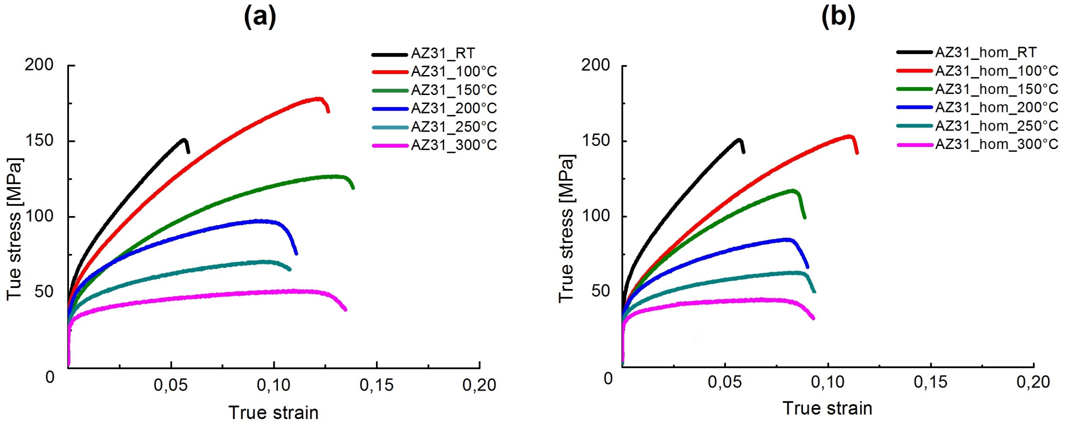

Figure 4.25: Stress-strain curves of AC AZ31 specimens strained at temperature range from RT to 300 °C: a) as-cast AC samples and b) AC samples after homogenization annealing at 450 °C for 10 hours.

Fig. 4.26a,b shows, respectively, stress-strain curves of the as-cast and aged TRC samples strained in RD. The behavior of the TRC material is entirely different when compared with the one of AC. The ductility of TRC samples significantly increases after homogenization and reaches 34 % at 300 °C. Also in this specimen a decrease of the ductility at 200 °C occurs.

Similar results were obtained also during straining of TRC specimen in TD (Fig. 4.26c,d). Slight increase of ductility with increasing temperature is observed up to 150 °C in TRC specimens followed by a significant decrease down to 7 % of elongation at 200 °C. Subsequent temperature growth leads, similarly as in specimens deformed in RD, to the increase of the ductility to about 12 % at 300 °C. Also homogenization of these specimens contributes to a significant decrease of ductility, nevertheless, the ductility anomaly (ductility decrease) is suppressed in this sample.

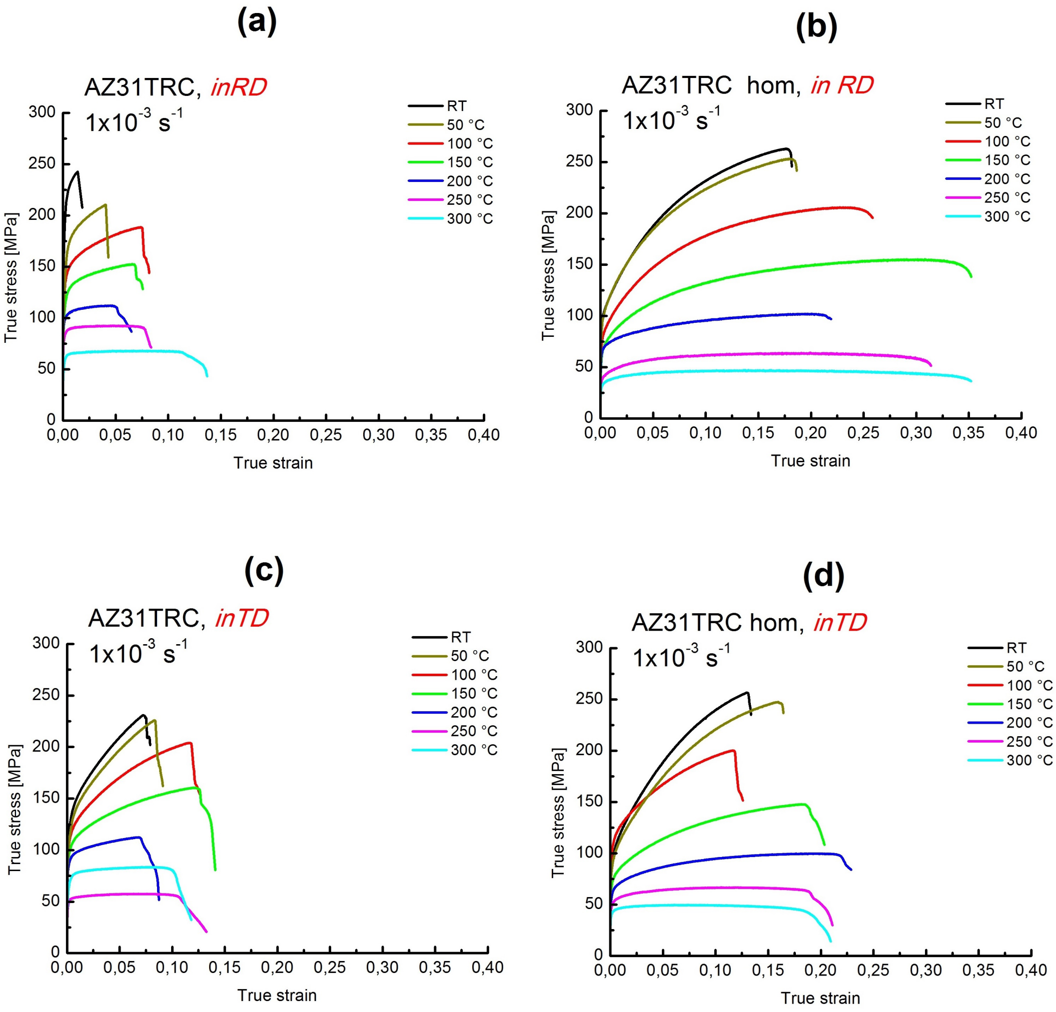

Figure 4.26: Stress-strain curves for TRC AZ31 magnesium alloys during straining at temperature range from RT to 300 °C: a) as-cast in RD, b) after homogenization annealing at 450 °C for 10 hours in RD, c) as-cast in TD, d) after homogenization in TD.

The above mentioned results are summarized in Fig. 4.27. Except for a homogenized TRC specimen strained in TD all samples repeatedly exhibit a drop of the ductility at 200 °C (150 °C in case of homogenized AC specimen).

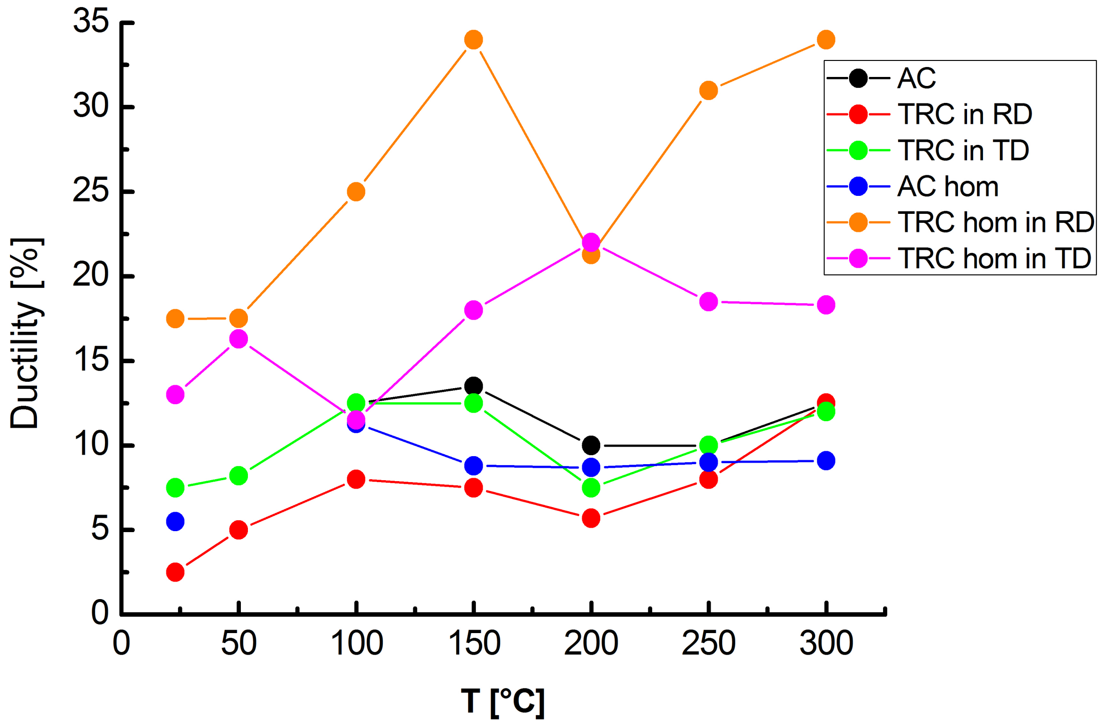

Figure 4.27: Temperature dependence of the elongation of AC and TRC magnesium alloys during straining at temperature range from RT to 300 °C.

Strong anisotropy of YS and UTS typical for rolled sheets is suppressed in both as-cast and homogenized TRC materials. Moreover, YS and UTS are superior in TRC materials when compared with AC ones (Fig. 4.28).

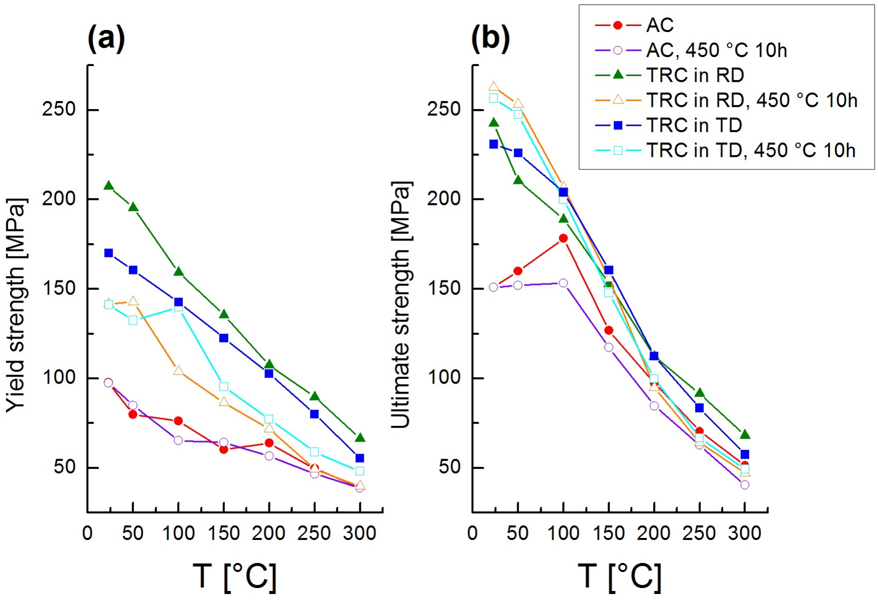

Figure 4.28: Temperature dependence of the yield stress and ultimate tensile strength of AZ31 magnesium alloy during straining at temperature range from RT to 300 °C tested in RD and TD.

4.2.8 Additional measurements

The drop of ductility near 200 °C described above has initiated a set of additional experiments necessary for the understanding of processes occurred in the materials in this temperature range. Samples were directly monitored using high-speed HR camera during straining and analyzed by LOM, AFM and SEM after the fracture.

Light optical microscopy

Fig. 4.29 shows inplain micrographs of regions near the fracture of TRC specimens deformed in RD at 100, 200 and 300 °C. A surface of the specimen deformed at 100 °C is rough and contain shear bands homogeneously distributed along the whole sample. They are tilted 45° towards the RD and their density is approximately 1.4 band/mm^2. Numerous twins are present in the sample in the direction perpendicular to shear bands (an example is indicated in Fig. 4.29b).

At 200 °C shear bands are more localized and distinct. Moreover, regions without any visible shearing are observed in this sample. The average shear bands density is approximately 0.9 band/mm^2 and grain boundaries between shear bands are less perceptible (Fig. 4.29c,d).

Increasing deformation temperature to 300 °C modifies features of bands. They are more uniformly distributed. Their density is about 1.1 band/mm^2. And finer grains can be distinguished in the interspace between the bands (Fig. 4.29) however, their area fraction is much higher than in previous cases. Fig. 4.29f shows that in the bulk of the sample finer grains can be distinguished.

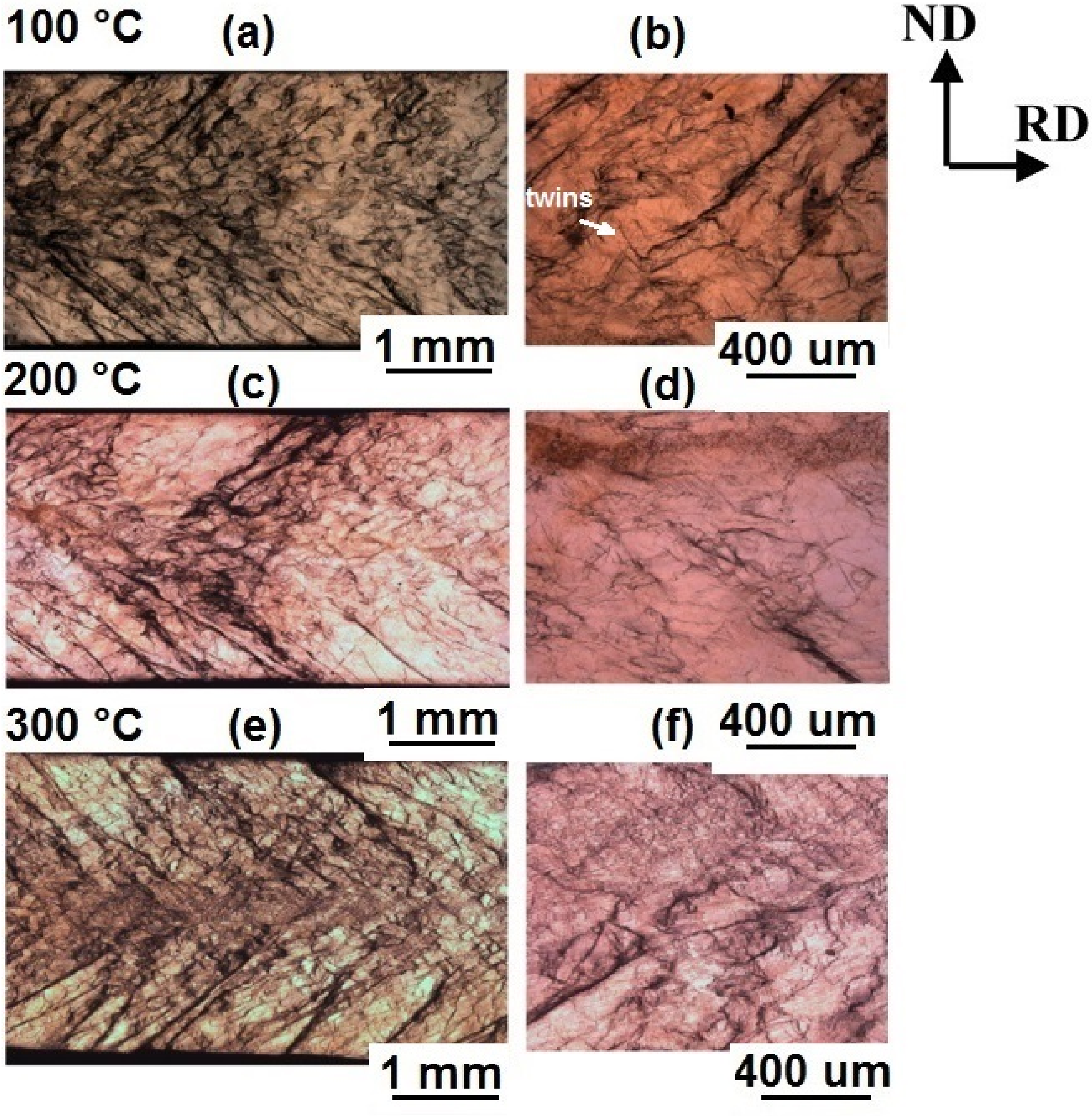

Figure 4.29: LOM images after tensile tests of TRC specimens deformed in RD at: a,b) 100 °C, c, d) 200 °C and e, f) 300 °C.

Surfaces of specimens deformed in TD are shown in Fig. 4.30. During deformation at 100 °C nearly no bands are formed. The surface of the sample is bumpy with a pronounced roughness. Deformation twins were not recognized by LOM (Fig. 4.30a,b). At 200 °C the formation of bands is more pronounced, however, they are spread through the specimen width with two prevailing directions crossing nearly at 90°. Fig . 4.30c,d shows that no twins or highly deformed grains are observed in the region between the bands. Bands are more dense at 300 °C, however, they are more shallow and do not spread into the material. Individual grains of about 200 µm exerted at the surface after straining can be distinguished as it is shown in Fig. 4.30e,f.

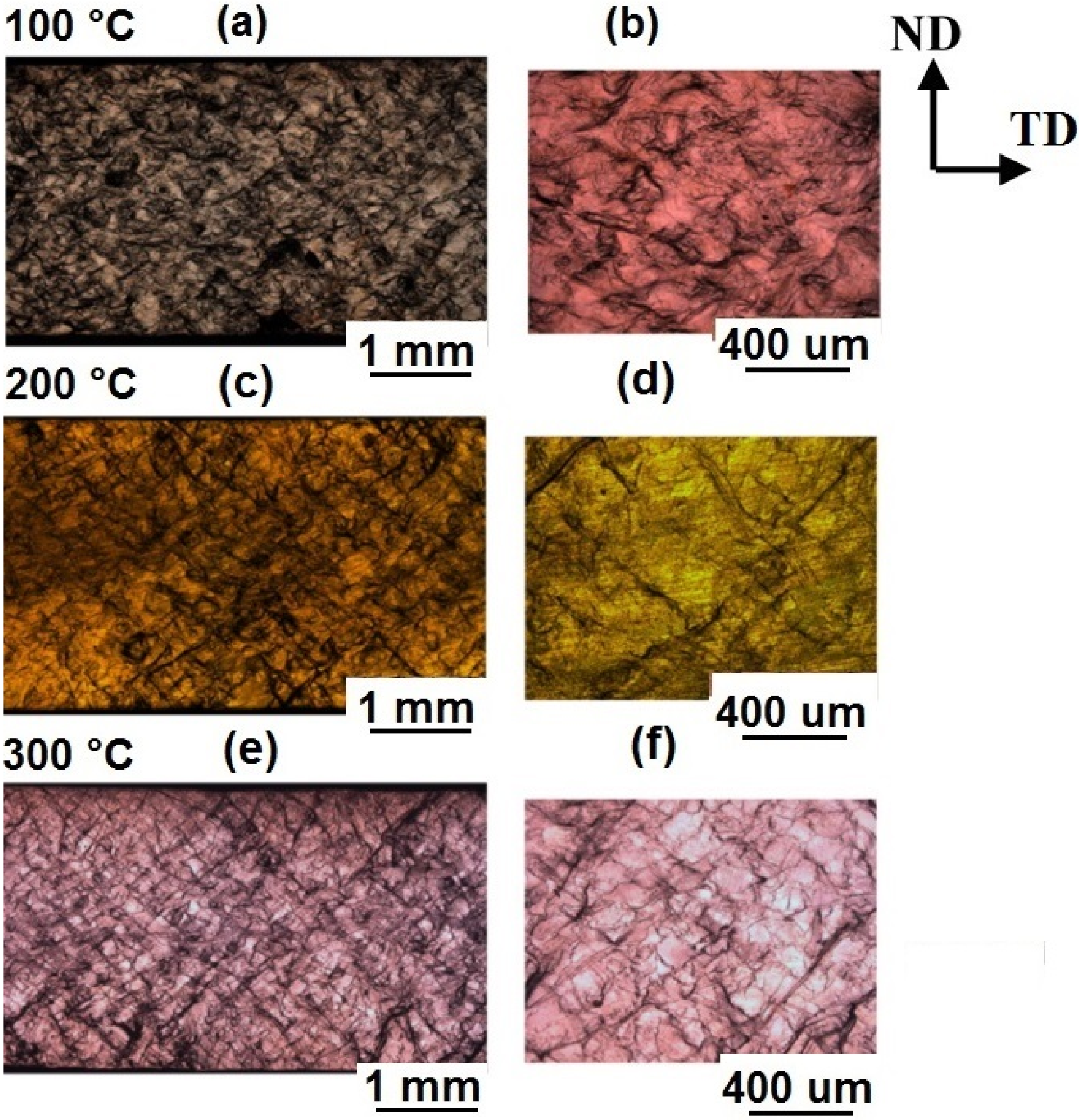

Figure 4.30: LOM images after tensile tests of TRC specimens deformed in TD at: a,b) 100 °C, c, d) 200 °C and e, f) 300 °C.

Video analysis

Video recording was performed during tensile tests of TRC specimens deformed in RD and TD. Fig. 4.31 shows the sequence of images obtained from the video with a step of 2 % of true strain. Full videos can be found on a CD attached to the thesis.

The video recording allows to follow a deformation progress and detect the nucleation of shear bands. In RD more pronounced shear bands are formed already at the beginning of straining in RD at all deformation temperatures. At 100 °C and 200 °C the bands are deeper and more localized along the samples, while at 300 °C the formation of bands occur homogeneously from early deformation stages. However, at 200 °C the localization of numerous bands in a narrow part of the specimen is more remarkable. Usually the failure occurs in such areas. Different behavior is observed in specimens deformed in TD. No visible shear bands forms during the whole deformation at 100 °C. The failure occurs in a random point different for different specimens from a testing set. At 200 °C shear bands are observed again unless they are more subtle than the ones observed in specimen deformed in RD. At 300 °C a similar homogeneous behavior as in the specimen deformed in RD is observed.

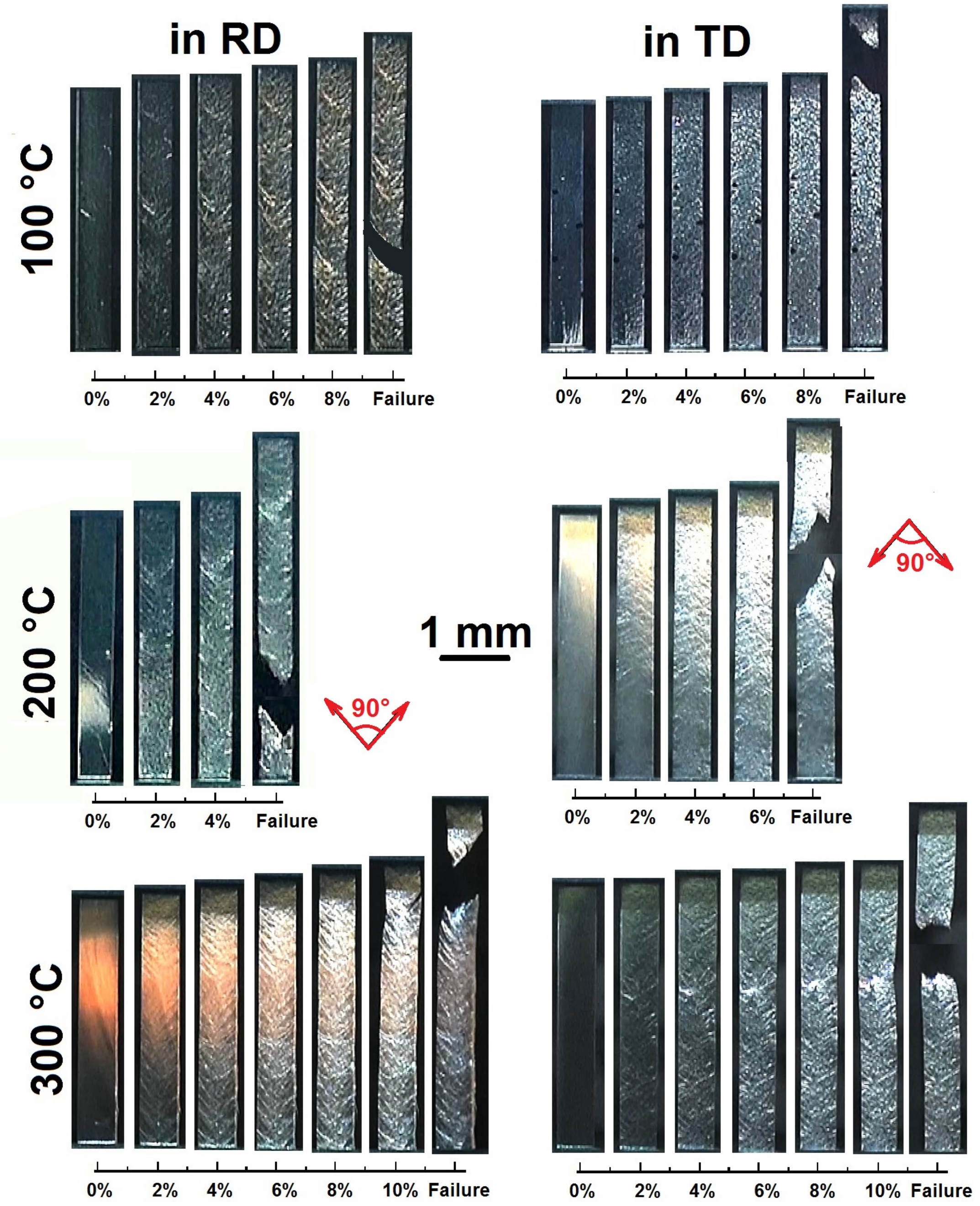

Figure 4.31: Sequence of images obtained from a video record during tensile tests performed in RD and TD at 100, 200 and 300 °C.

In addition a shape of a fracture tip differs at selected temperatures. At 100 °C the failure goes through the strip width in both types of specimens. On the other hand, the sharp tip with an angle about 90° is observed at 200 °C. A typical "necking" and ductile failure occur in TRC samples deformed at 300 °C.

SEM and EBSD

Samples after tensile tests were studied using EBSD measurements. Orientation maps of samples deformed in TD are shown in Fig. 4.32. Generally, no significant differences can be distinguished on the EBSD maps of samples deformed at 100, 200 and 300 °C. Deeper analyses of grain size distribution show a slight increase of the volume fraction of fine grains at grain boundaries formed during DRX at 200 °C than at 100 °C. At 300 °C (Fig. 4.32c) the fraction of finer grains produced by DRX is comparable or lower than in previous specimens, However, a fragmentation of unrecrystallized grains into individual subgrains seems to be more pronounced.

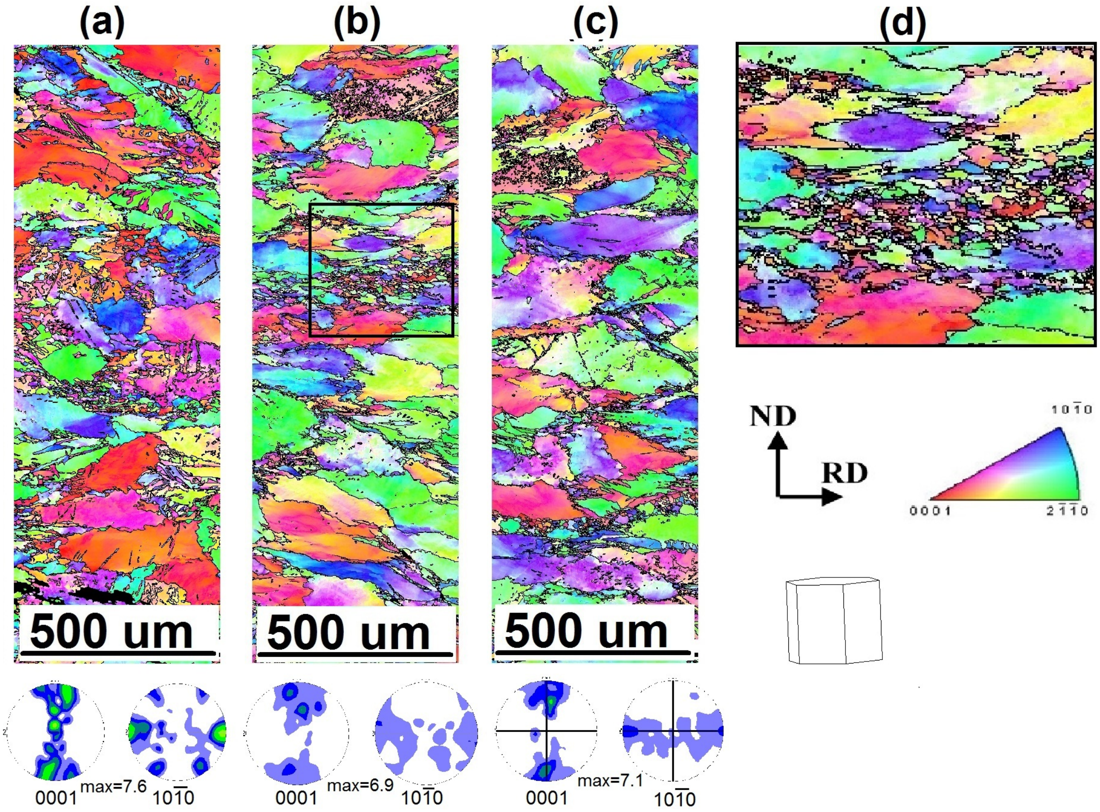

Figure 4.32: Orientation maps and PF of TRC samples after tensile tests deformed in RD at a) 100 °C, b), d) 200 °C and c) 300 °C.

TRC strip after homogenization treatment at 450 °C for 10 h exhibit more homogeneous structure with no strains inside grains. However, tensile tests of this material in RD also show the decrease of ductility at 200 °C. Fig. 4.33 shows BSE images of homogenized samples deformed in RD at 100, 200 and 300 °C captured using channeling contrast. The prevalence of twins inside the grains after deformation at 100 °C is observed, while only few of them are present in the sample deformed at 200 °C. At 300 °C no twins are observed, however, subgrain boundaries can be easily distinguished in this specimen using this type of contrast.

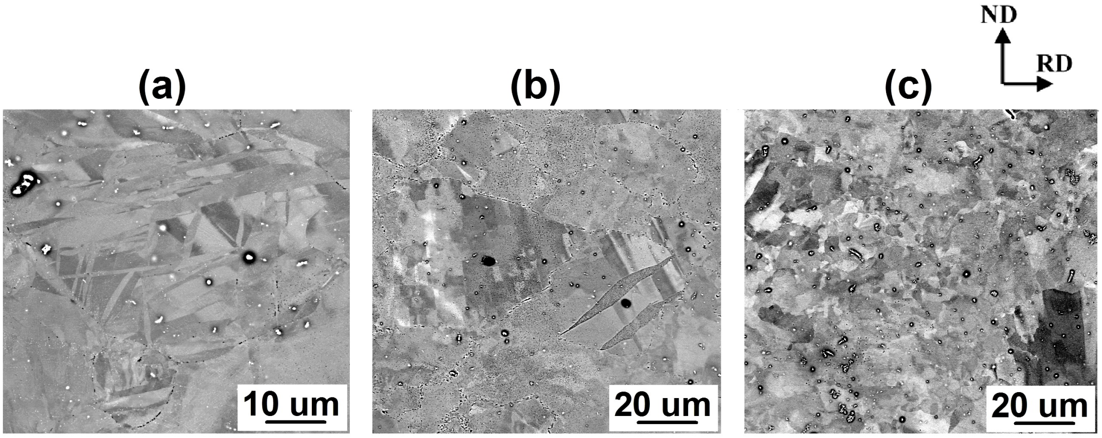

Figure 4.33: SEM channeling contrast images after tensile tests of homogenized TRC specimens deformed in RD at a) 100 °C, b) 200 °C and c) 300 °C.

Atomic force microscopy

In order to study a surface topography of samples after tensile tests AFM technique was used in a tapping mode. Selected regions of specimens deformed in RD and TD were scanned. The AFM maps 100 × 100 μm^2 of the TRC samples deformed in RD and TD are shown in Fig. 4.34 and 4.35, respectively.

Scanning of the deformed regions of the specimen tested at 100 °C in RD shows numerous slip bands of two slip systems where the one marked by the red arrow is more active (Fig. 4.34a). Both systems are tilted 45° to the RD. No recrystallized grains were observed using this technique. On the contrary, at 200 °C the recrystallized grains are present in some of the initial grains at original grain boundaries (Fig. 4.34b) and also grain boundary sliding is observed (Fig. 4.34c). Also at this temperature at least two slip systems are present, nevertheless, none of them exhibits a preferential activity and the height of slip traces is more shallow than in the specimen deformed at 100 °C. Fig. 4.34d shows a topography of an incidental region in the material, where only recrystallized grains are present. These grains do not contain any slip traces indicating a prevailing post-dynamic recrystallization instead of DRX. Likewise, developed recrystallized grain structure is observed all over the material deformed at higher temperature (300 °C) as it is illustrated in Fig. 4.34e. Moreover, these grains do not contain slip traces, straight lines observed in Fig. 4.34e are artifacts from polishing before the deformation.

Using AFM the differences of microstructure after tensile tests made in TD and RD can be distinguished (Fig. 4.35). Fine slip traces are homogeneously distributed on the surface on a background of broader wavy slip traces inclined 45° to the TD at 100 °C. At 200 °C slip system producing wavy slip traces is partially suppressed while the previously observed fine slip traces are more pronounced. Moreover, a subtle grain boundary sliding can also be observed in Fig. 4.35b. The image characterizing the microstructure of the specimen deformed at 300 °C contains onlly fine recrystallized grains Fig. 4.35c without any slip traces indicating the presence the post-dynamic recrystallization.

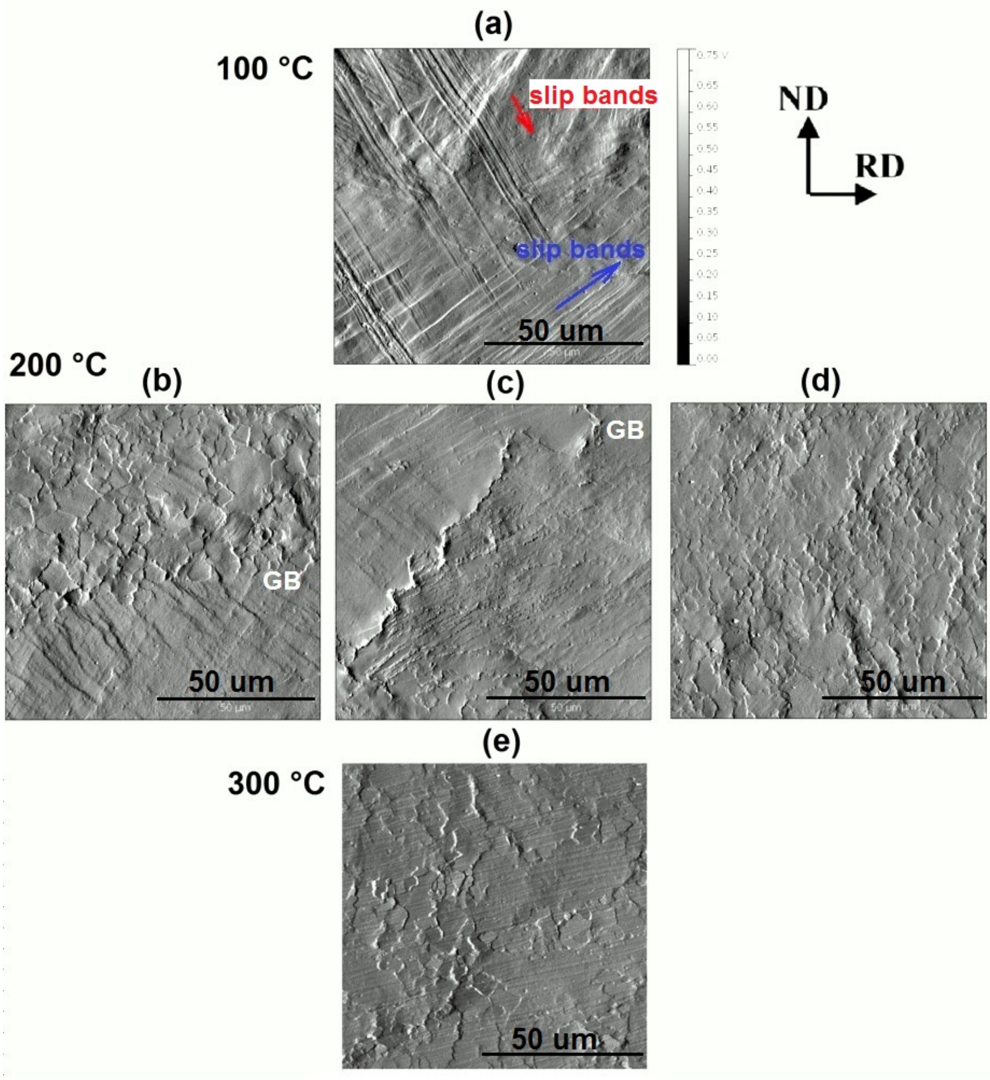

Figure 4.34: AFM images of the selected areas of TRC strip specimens after tensile tests performed in RD at: a) 100 °C, b-d) 200 °C and e) 300 °C. Arrows indicate glide planes of the most active slip systems.

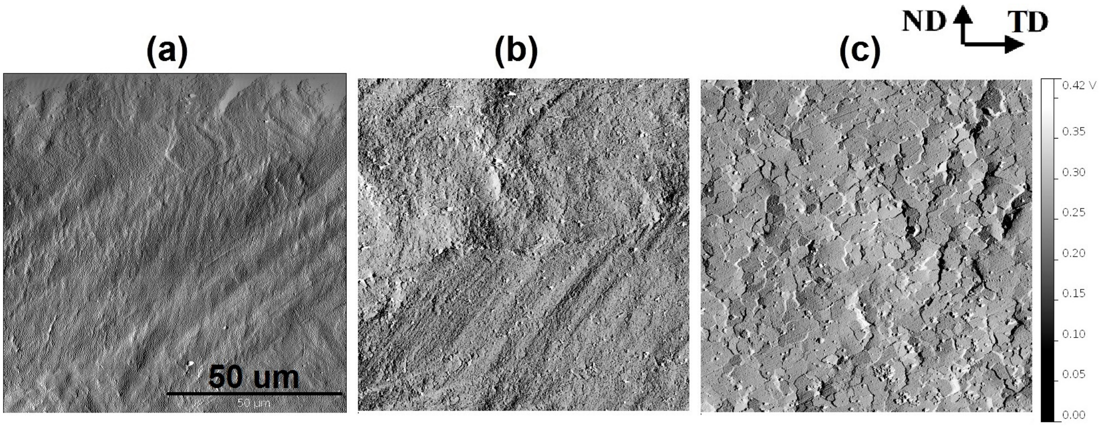

Figure 4.35: AFM images of the selected areas of TRC strip specimens after tensile tests performed in TD at: a) 100 °C, b) 200 °C and c) 300 °C.

4.3 Severe plastic deformation

4.3.1 Equal channel angular pressing

Microstructure

Specimens cut from AC ingot and TRC strip were subjected to a further SPD using ECAP. As it was described in Chapter 3 the effects of a pre-annealing as well as of the orientation of TRC samples on a resulting microstructure were studied.

EBSD orientation maps of the first set of AC samples in the initial state and after ECAP are shown in Fig. 4.36. In contrast to the as-cast material with the average grain size of 200 μm a significant refinement of microstructure occur after already two ECAP passes. High area fraction of new grains of less than 1 μm is observed. These grain are formed primarily at grain boundaries of initial grains as well as on subgrain boundaries. After four passes the refinement is more pronounced with increasing number of recrystallized grains of a size of about 1 μm and decreasing size of remaining unrecrystallized grains of the size of 20 μm. Homogeneous fine-grained structure is produced as late as after eight deformation passes with the average grain size of 1.5 μm.

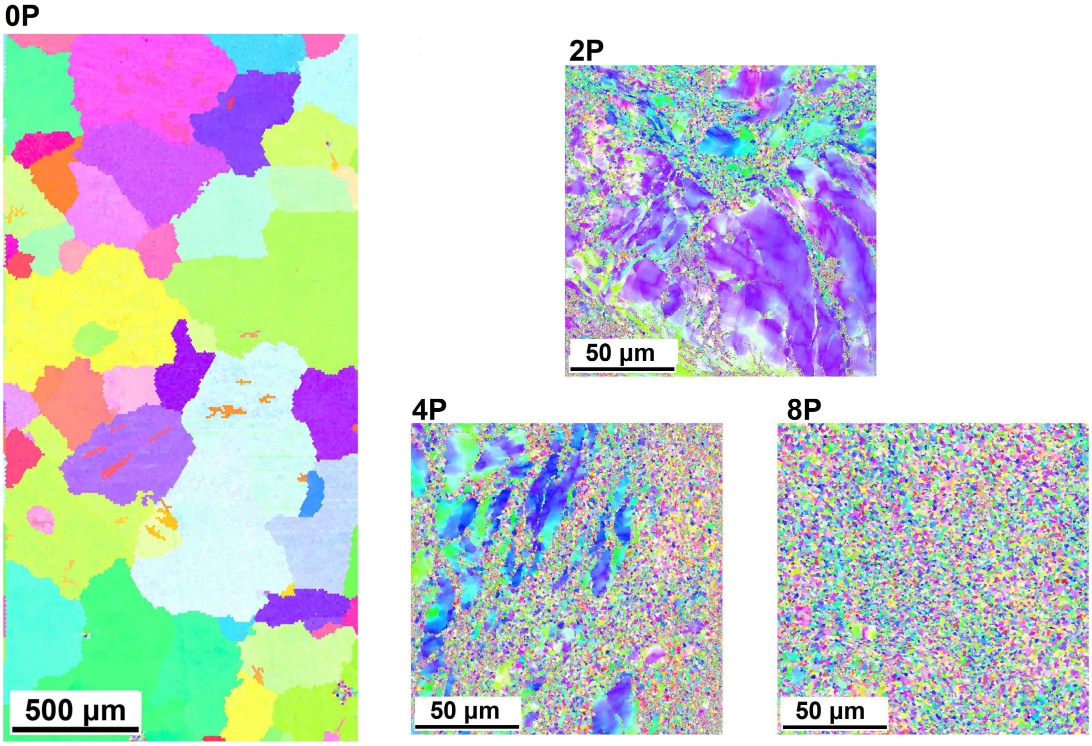

Figure 4.36: EBSD maps of AC samples after 0, 2, 4 and 8 ECAP passes.

Samples cut from the TRC strip were deformed in both RD and TD as it was described in Chapter 3 with the pressing direction perpendicular to the ND of the sample as it was described in Chapter 3.

Microstructure of TRC samples strained in RD after one, four and eight ECAP passes is shown in Fig. 4.37a. After one ECAP pass the microstructure has a "bimodal" feature. Numerous fine grains nucleate at grain boundaries of the coarser grains during ECAP. An average grain size of original unrecrystallized grains is about 30 µm while the grain size of newly formed ones is less than 3 µm. After four passes the bimodal structure still persists, however, the area fraction of finer grains is much higher (75 %) than that of larger ones. A further ECAP processing does not significantly contribute to a grain refinement of the material. Thus, after eight ECAP passes the grain size of finer grains of less than 1 µm remains the same as after four passes. However, the structure becomes homogeneous without the presence of coarse deformed grains.

Fig. 4.37b illustrates the microstructure of TRC samples pre-aged before ECAP at 450 °C for 10 h deformed in RD. One ECAP pass also forms a bimodal structure. Nevertheless, both recrystallized and original grains are larger than the those observed in the non-homogenized sample. The average grain size of newly formed grains is about 8 µm and of the deformed is about 40 µm. After the second ECAP pass the fraction of newly recrystallized grains increases (40 %) and their formation is nearly accomplished after four ECAP passes (area fraction of new grains is about 90 %). However, this recrystallization is accompanied by a slight grain coarsening of already recrystallized grains (the grain size increases from 3 to 5 µm). Deformation imposed by eight ECAP passes creates more homogeneous grain size distribution and slight decrease of the grain size down to 3 µm.

The behavior of TRC samples deformed in TD is very similar to the one observed in specimens processed in RD (Fig. 4.38). The only remarkable difference is a considerably higher grain size after eight ECAP passes of homogenized specimens (Fig. 4.38b).

Thus, it was shown that the full recrystallization and balancing of the microstructure in TRC samples regardless pressing direction occurs after four ECAP passes, however, the grain refinement is more pronounced in as-cast materials than in homogenized ones processed in both RD and TD directions.

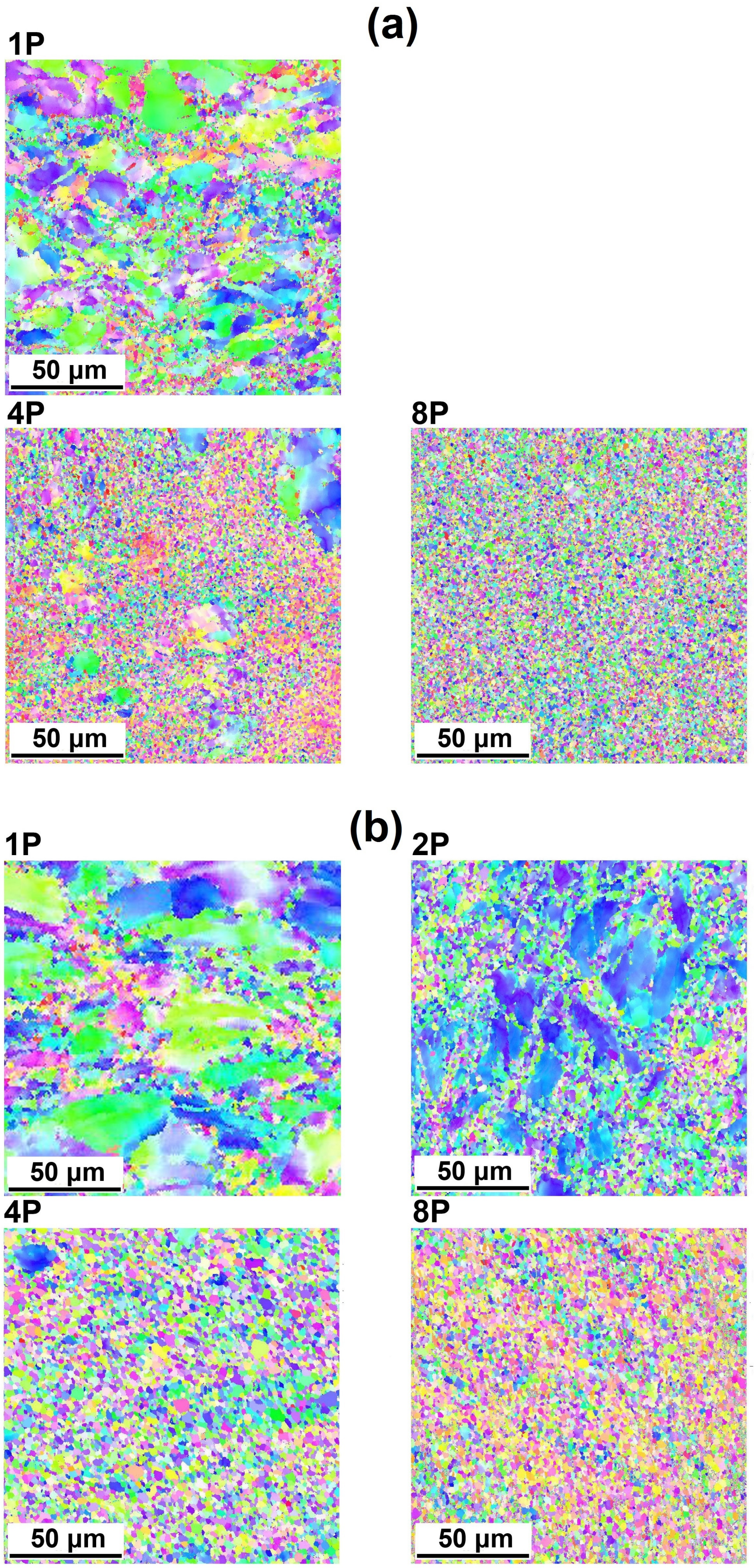

Figure 4.37: EBSD maps of TRC samples processed by ECAP in RD: a) as-cast, b) sample homogenized at 450 °C for 10 h.

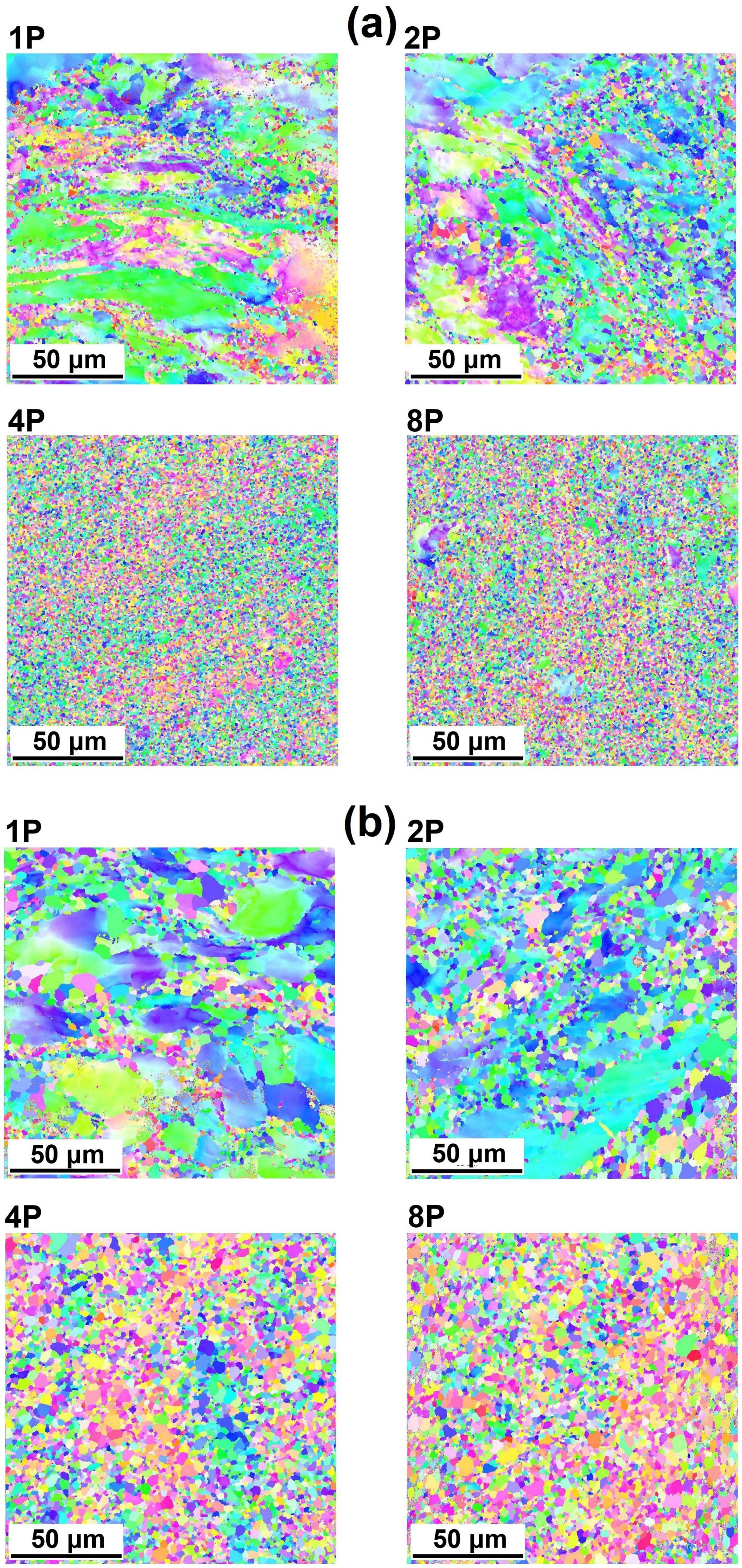

Figure 4.38: EBSD maps of TRC samples processed by ECAP in TD: a) as-cast, b) sample homogenized at 450 °C for 10 h..

Texture

EBSD texture analysis of the samples after ECAP processing was performed and the results are presented in a form of {0001 and 01$\bar{1}$0 pole figures in Fig. 4.39, 4.40 and 4.41.

The AC sample exhibits a partially random texture (Fig. 4.39 0P). As can be seen, no significant texture components can be detected; the crystallites are randomly oriented, as it is common in this type of cast magnesium alloys. ECAP processing results in a formation of a higly pronounced basal texture after two passes with basal plains tilted about 30° towards the deformation Y-axis. A weakening of the basal texture is observed after four and eight passes.

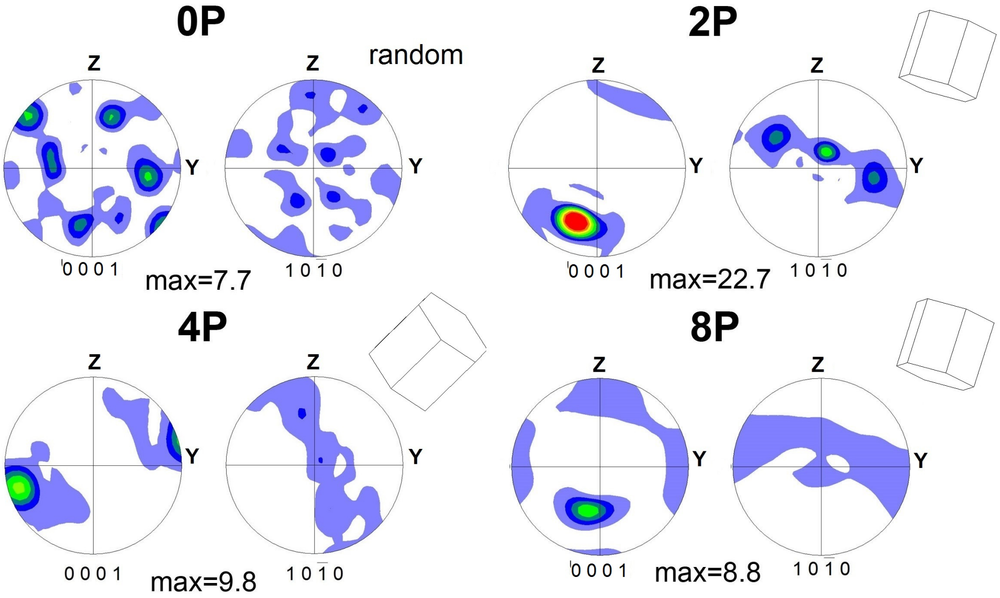

Figure 4.39: Pole figures of AC samples before ECAP and after 2, 4 and 8 ECAP passes.

Evolution of texture of the samples deformed in RD is illustrated in Fig. 4.40. Similarly to AC sample ECAP results in a strengthening of basal texture (Fig. 4.40a). After one pass c-axes of the majority of grains are perpendicular to the deformation X-axis. The rotation of the texture components 35° towards X-axis occurs after four passes. And slight weakening of the basal texture is observed after eight passes. The texture behavior of homogenized samples (Fig. 4.40b) after one ECAP pass is similar to the one in the as-cast sample. After two passes a noticeable randomization of the basal texture occurs. Nevertheless, the following ECAP passes (four and eight) again strengthen the basal texture and tilt the circumferential region of the 0001 PF by about 30°.

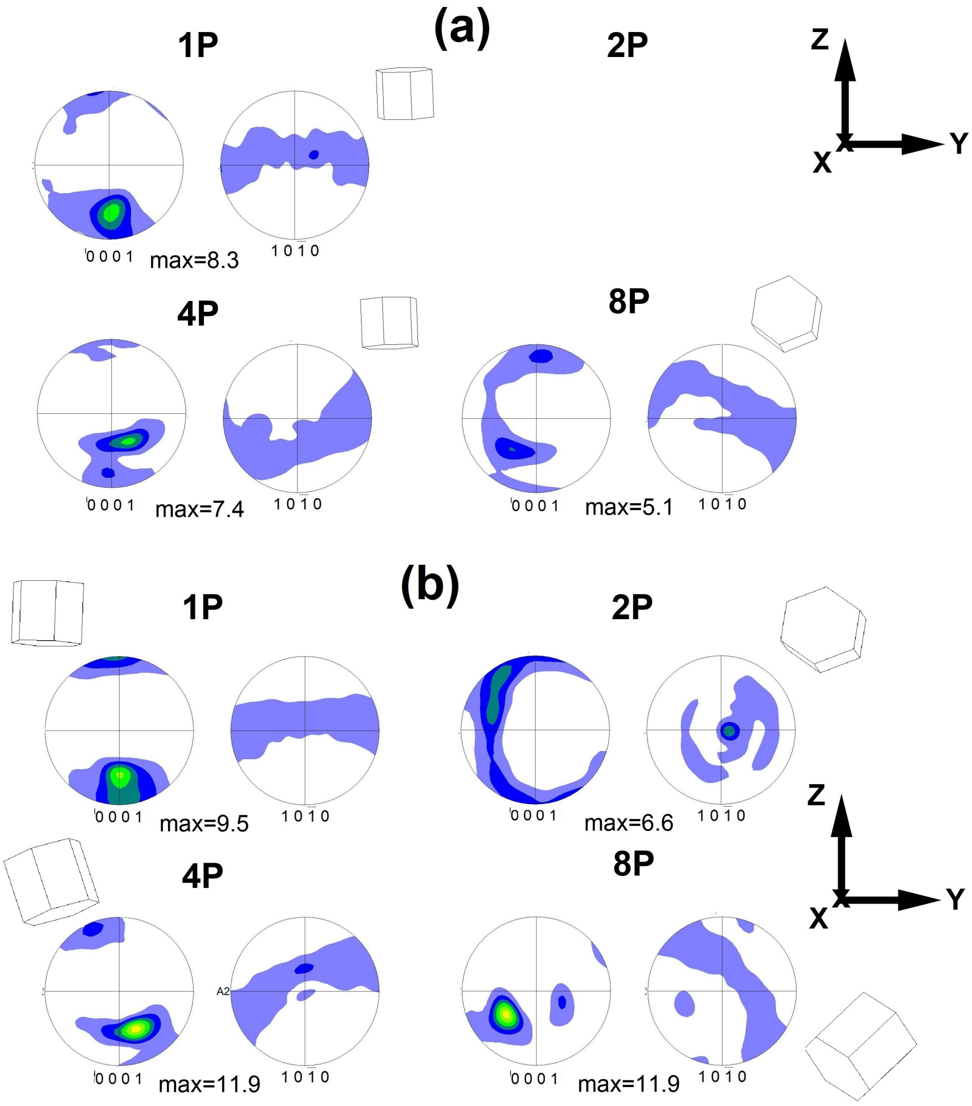

Figure 4.40: Pole figures of the TRC strip processed by 1, 2, 4 and 8 ECAP passes in RD: a) as-cast sample, b) sample homogenized at 450 °C for 10 h.

Fig. 4.41 illustrates PF obtained from the TRC samples ECAP processed in TD direction. No significant differences of the texture evolution between samples processed in this direction and in RD are observed.

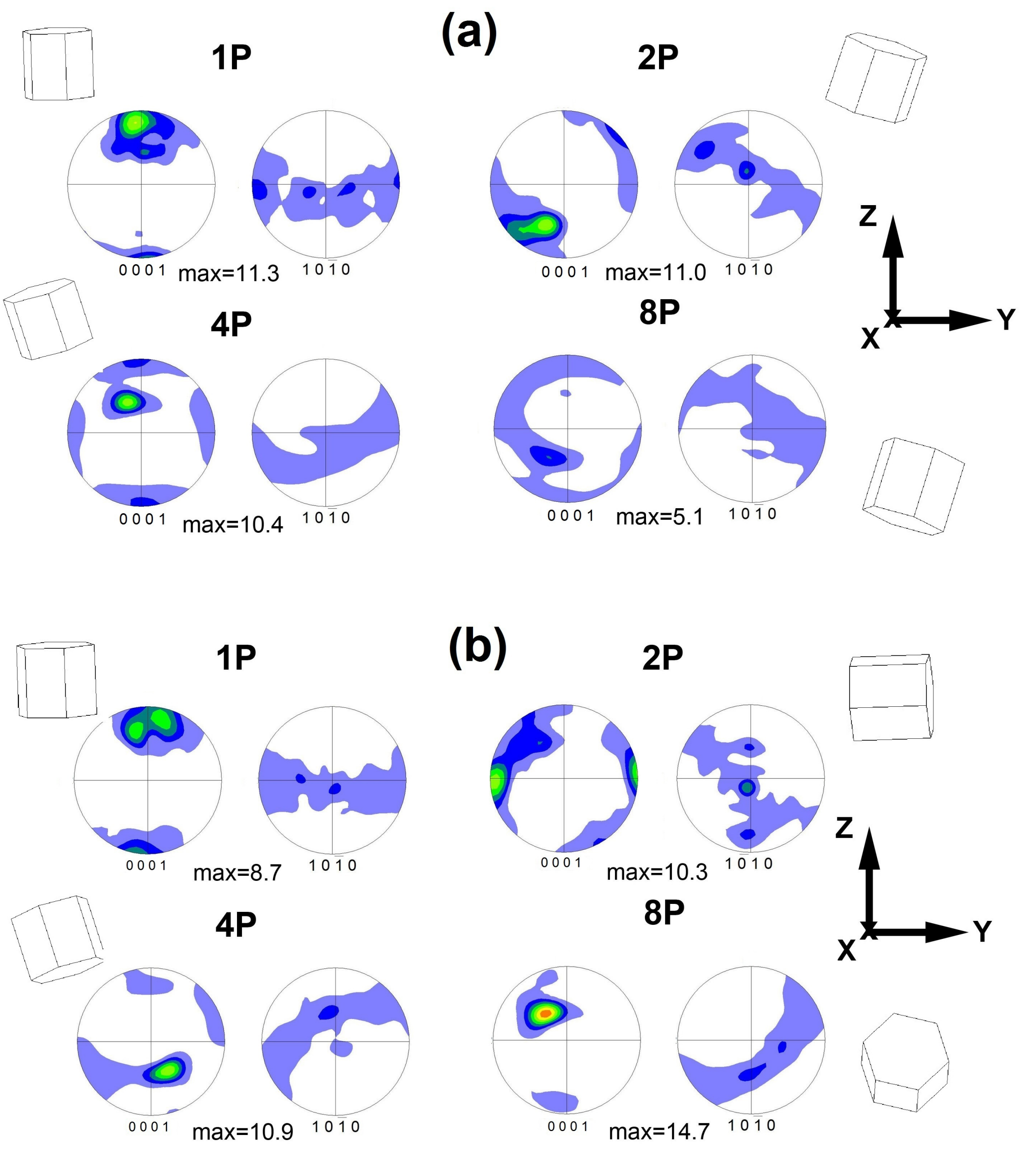

Figure 4.41: Pole figures of the TRC strip processed by 1, 2, 4 and 8 ECAP passes in TD: a) as-cast sample, b) sample homogenized at 450 °C for 10 h.

Heat treatment after ECAP

TRC samples subjected to one and eight ECAP passes were aged after the processing in order to study a thermal stability of the material. The microstructure BSE images are shown in Fig. 4.42. Additional aging at 450 °C for 5 h after ECAP processing results in a balancing of the microctructure of all samples. In the case of a sample after one ECAP pass originally exhibiting a bimodal microstructure before aging, the homogenization of the microstructure occurs resulting in a uniform distribution of coarser grains of the size of about 20 μm (Fig. 4.42a,b). The grain growth is also observed in samples after eight ECAP passes and the grain size increases up to 20 μm in all samples aged for 5 h (Fig. 4.42c,d). Nevertheless, after 10 h non-uniform coarsening occurs (Fig. 4.42e).

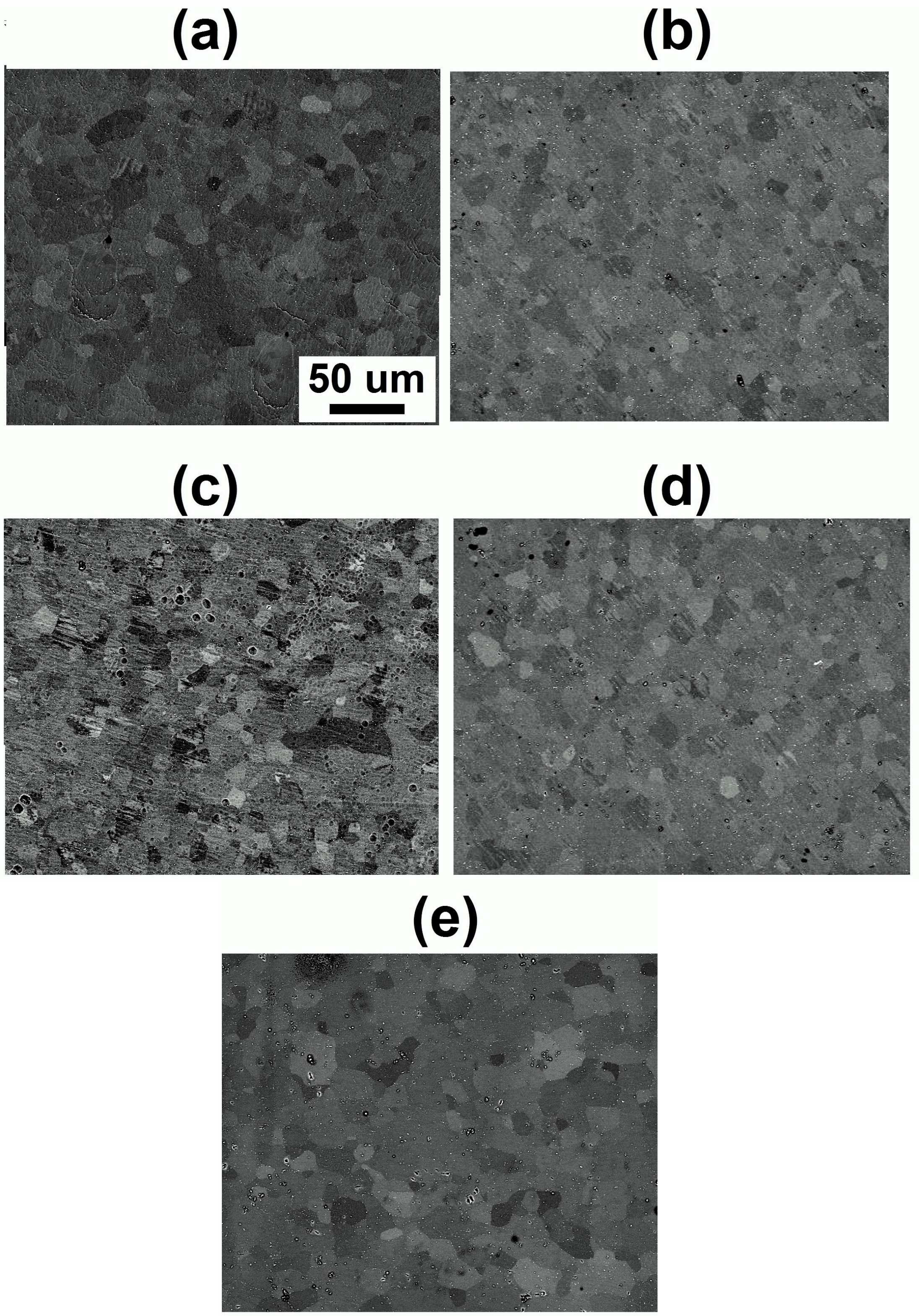

Figure 4.42: Microstructure of the TRC strip processed in TD using ECAP: a) homogenized and after 1P aged at 450 °C for 5 h, b) homogenized and after 8P aged at 450 °C for 5 h, c) as-cast and after 1P aged at 450 °C for 5 h, d) as-cast and after 8P aged at 450 °C for 5 h and e) as-cast and after 1P aged at 450 °C for 10 h.

The evolution of the texture of chosen samples deformed using ECAP and further artificially aged is shown in Fig. 4.43. The aging leads to a significant randomization of the texture in both homogenized and as-cast TRC materials. The above mentioned results indicate that SPD can be used as an effective tool for the elimination of the basal texture in TRC strips.

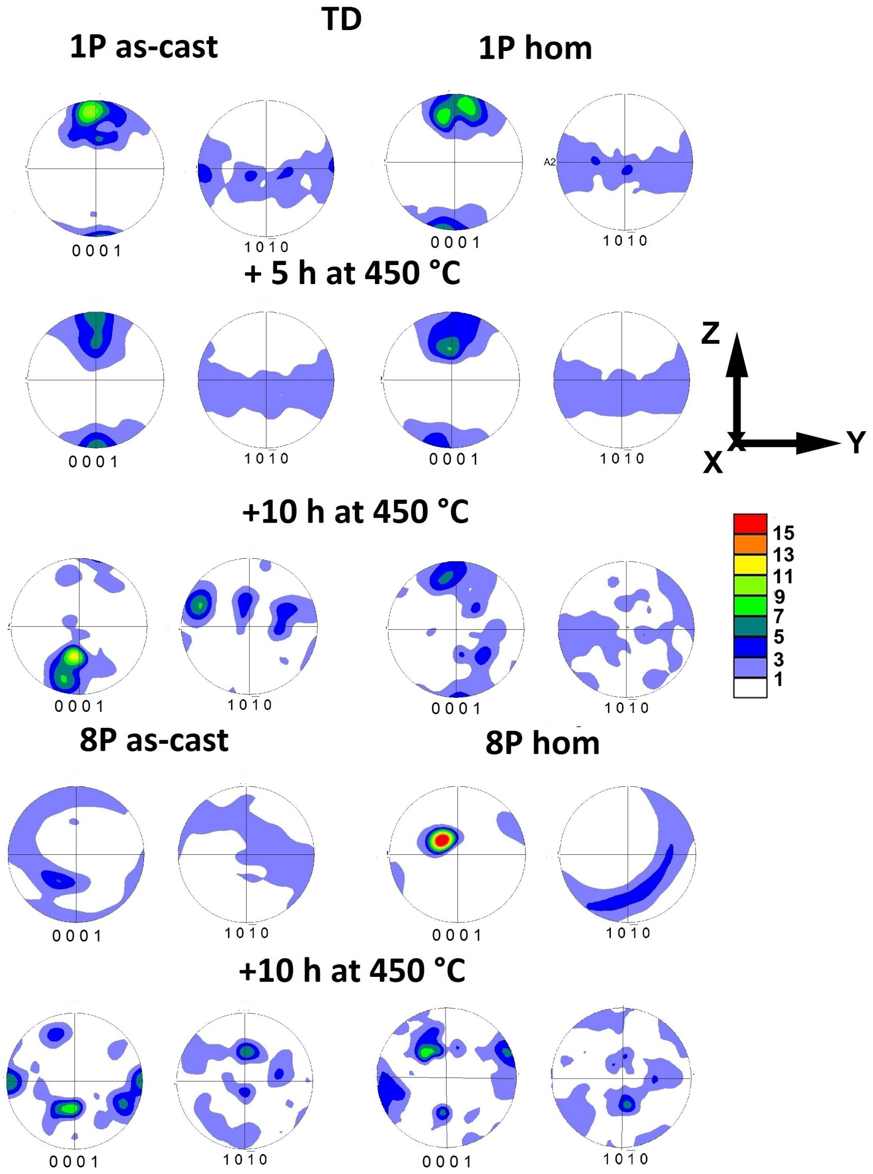

Figure 4.43: PF of TRC strip ECAP process in TD and aged at 450 °C for 5 h and 10 h.

Microhardness

Local mechanical properties of samples after ECAP were studied. Fig. 4.44 shows results of microhardness measurements performed on AC and TRC samples after ECAP processing and samples ECAP processed and aged at 450 °C. A significant increase of the microhardness is observed already after the first ECAP pass. Increasing number of passes leads to a saturation of microhardness values. The increase is more pronounced in AC samples and TRC samples without homogenization. Further aging at 450 for 5 h eliminates the differences in microhardness of all samples, the microhsardness drops to about 53 HV0.1, and aging for 10 h does not significantly change this value.

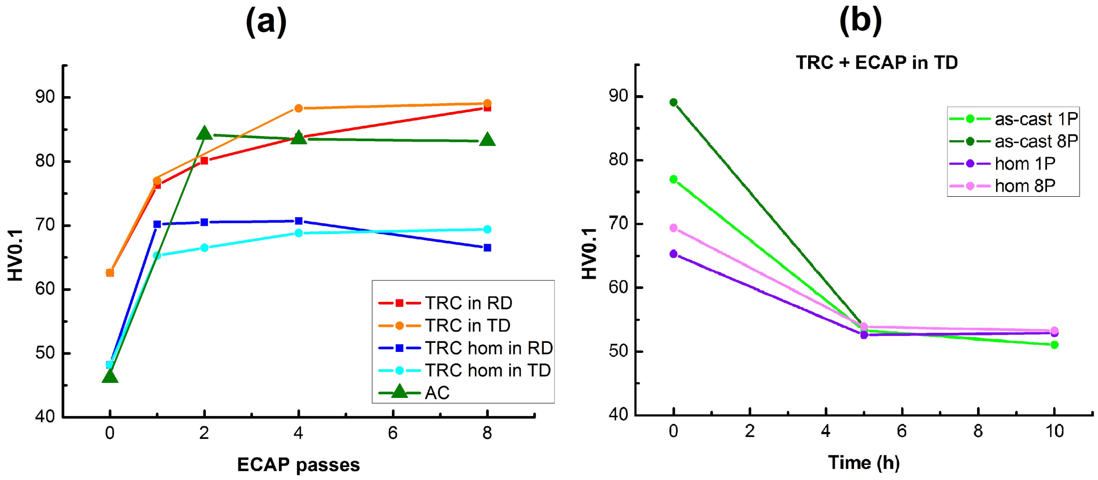

Figure 4.44: The dependence of the HV0.1 microhardness of AC and TRC samples processed by ECAP on a) the number of ECAP passes and b) additional annealing time.

4.3.2 Constrained groove pressing

Microstructure

Each CGP step was preceded by a pre-heating of specimens for 10 min at 450 °C. It provided non-recrystallized microstructure of the strip before deformation as is shown in Fig. 4.15a.

Fig. 4.45a shows the cross-section of the deformed CGP plate. Grain size varies from ten to hundreds of microns and three zones characterized by different grain size can be easily distinguished on the specimen cross-section (indicated by frames in Fig. 4.45b-d). Fig. 4.45b shows the most deformed area with the average grain size of about 10 μm. Another zones with the grain size of about 20 μm is located in a distance of 7 mm (Fig. 4.45d). Microstructure of the above mention two part of the sample is relatively homogeneous. Between them is a transition zone which is characterized by a bimodal microstructure with larger grains of the size of about 60 μm and smaller ones of about 8 μm. Only in this area large fraction of deformation twins is observed (Fig. 4.45c). The periodicity of these three regions is 14 mm representing a geometry of a die.

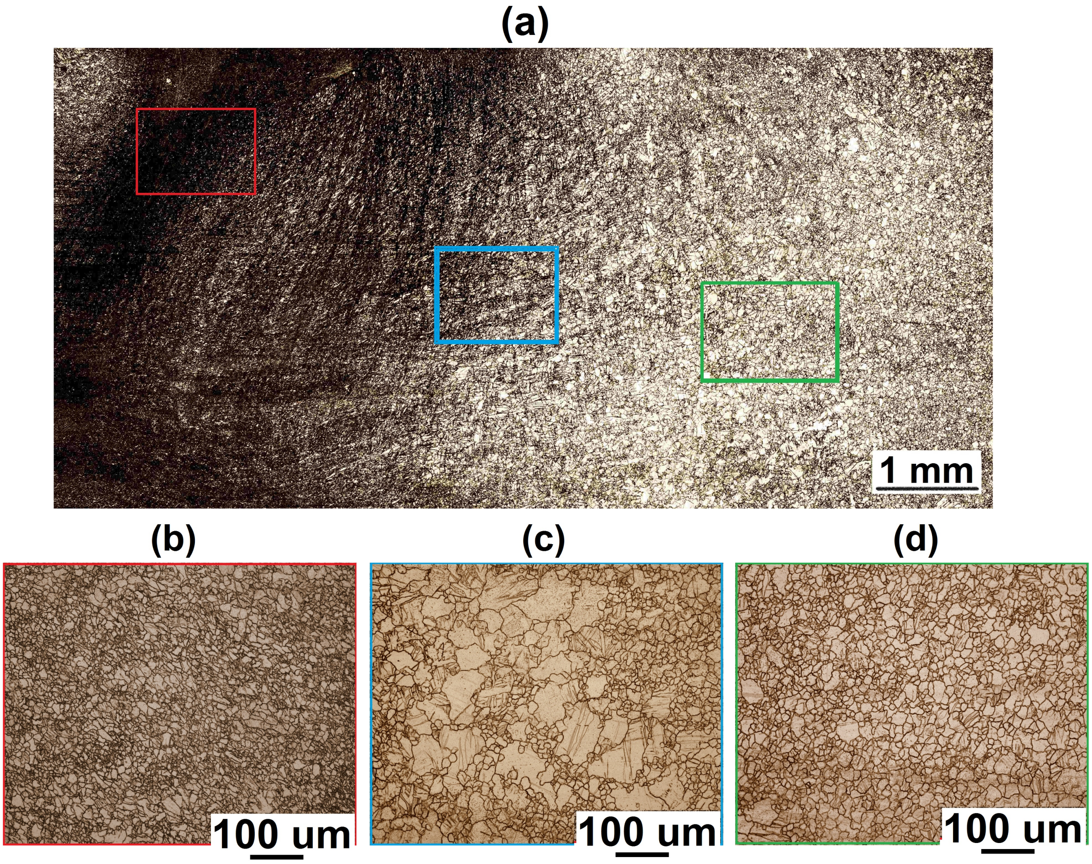

Figure 4.45: Microstructure images of the cross-section of the twin-roll cast strip after one cycle of constrained groove pressing: a) cross-section imaging at 50x, b) the most deformed zone, c) transition "bimodal" zone and d) bulk.

In order to examine the resistance of the CGP material to the thermal loading specimens were annealed up to 250, 350 and 400 °C. The microstructure passes through substantial changes resulting in a more homogeneous distribution of a grain size, but the three distinctive areas can be still well distinguished at all annealing temperatures as is present in Fig. 4.46. The microstructure after annealing at 250 °C is almost the same as the one observed in the as-deformed material. Further annealing results in the nucleation of new grains and pronounced decrease of the volume fraction of twins. At 350 °C and 400 °C the originally deformed grains are replaced by new finer ones. Their size is around 10 μm in the areas (a) and (c) and down to 40 μm in the transition area (b). No deformation twins were observed in specimens annealed up to 400 °C. The long-term high-temperature aging at 450 °C for 10 h shows that the CGP process promotes uniformity and refinement of the structure. The observed grain size was about 25 μm in the transition zones and about 10 μm in the rest of the material.

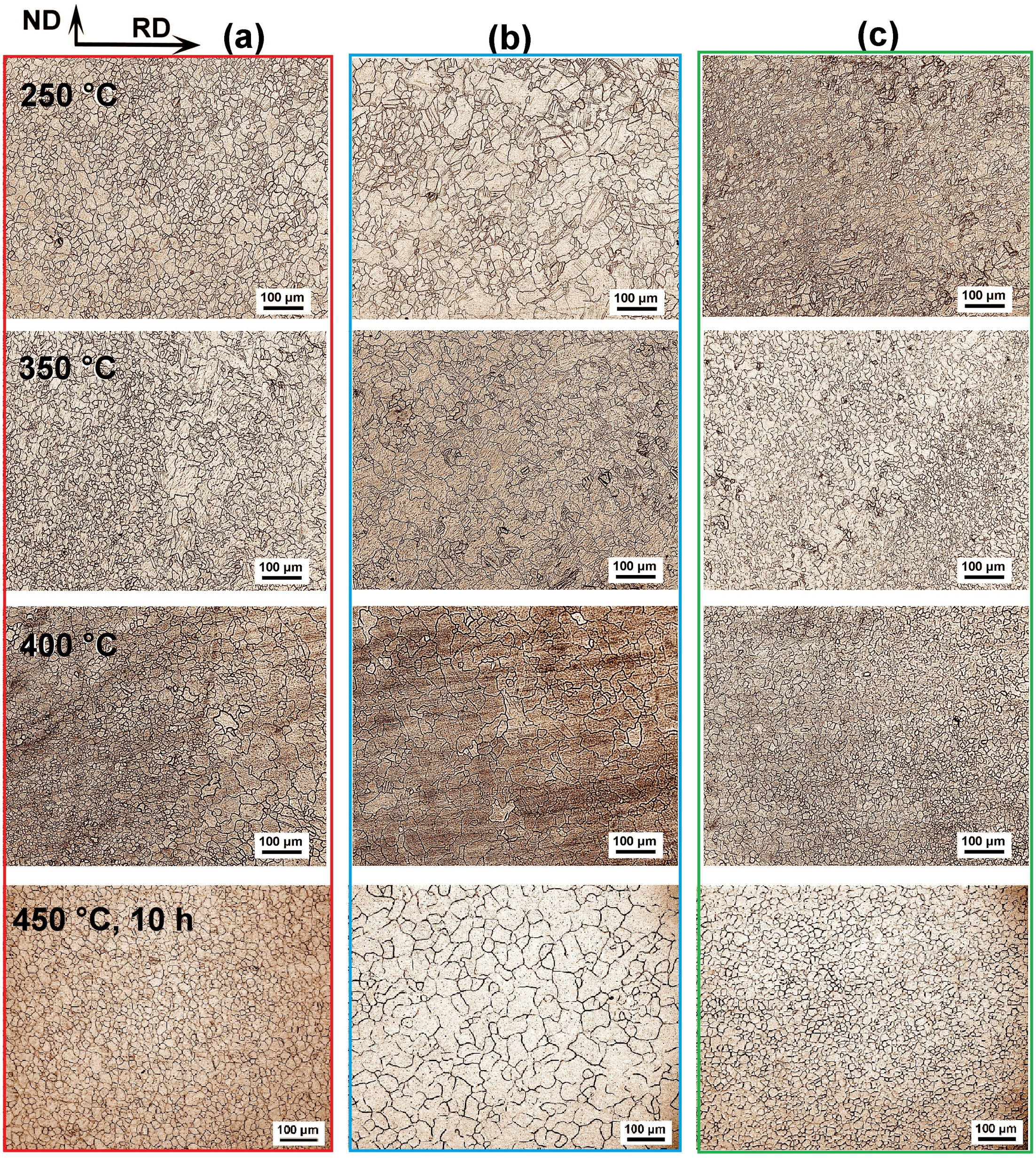

Figure 4.46: Microstructure of the AZ31 twin-roll cast strip after one CGP cycle and annealing at 250, 350, 400 °C and aging for 10 h at 450 °C: a) the most deformed zone, b) transition "bimodal" zone and c) bulk.

Fig. 4.47 shows the microstructure of the cross-section of the CGP material aged at 450 °C for 10 h and 30 h. 10 hours of aging leads to a partial recrystallization of the material accompanied by a grain growth (Fig. 4.47a). Nevertheless, smaller unrecrystallized grains still persist and a full recrystallization occurs after 30 h of annealing at 450 °C (Fig. 4.47b).

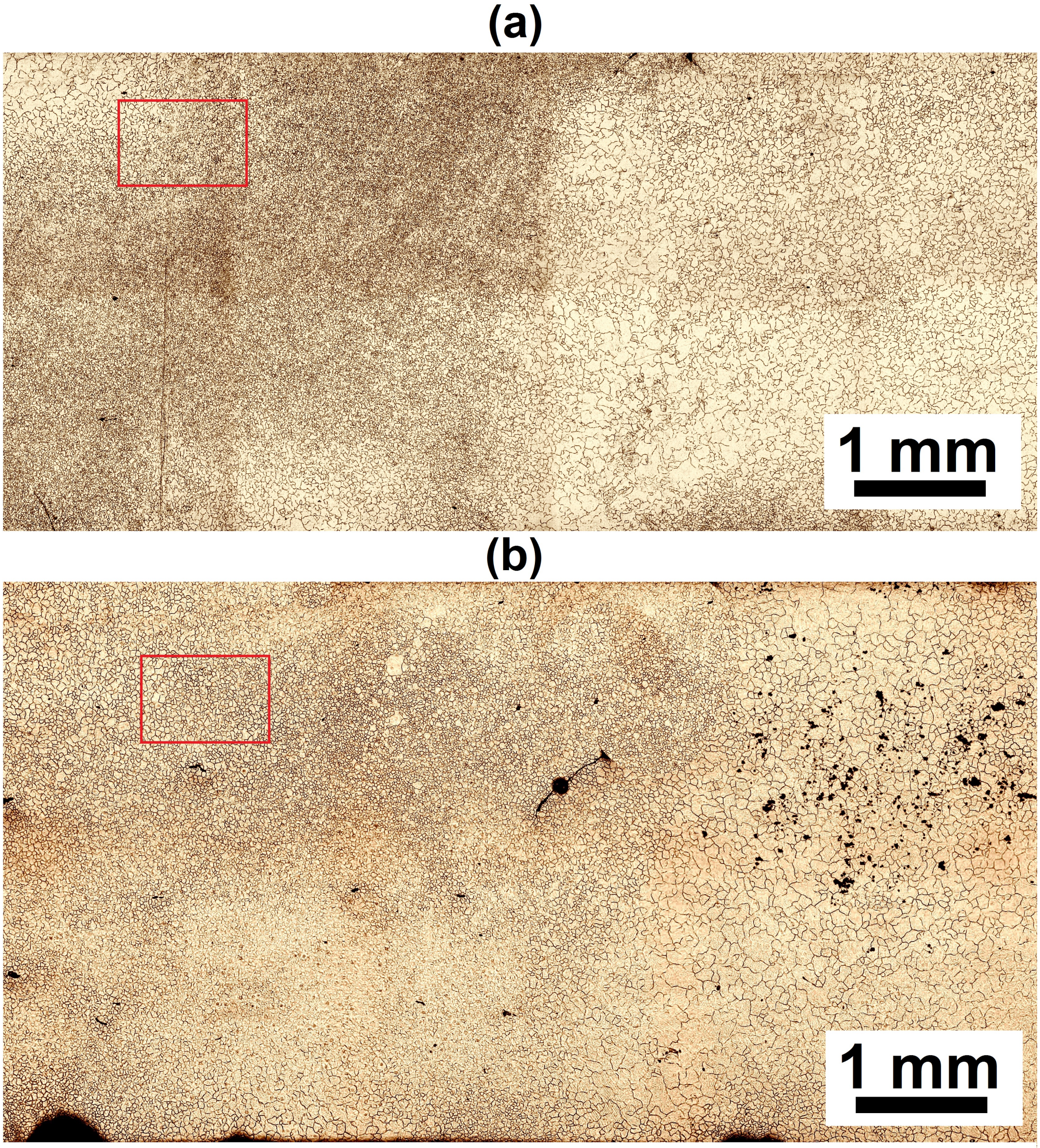

Figure 4.47: Microstructure of the TRC strip after one CGP cycle and aging at 450 °C for: a) 10 h and b) 30 h.

Texture

EBSD observations were performed in zones indicated by red boxes in Fig. 4.47. Fig. 4.48 shows orientation maps obtained in these areas in the material after one CGP cycle and further aging. The average grain size after one CGP step is about 18 µm and increases to 80 µm after 10 h at 450 °C and to 100 µm after 30 h at 450 °C.

Figures 4.48b,c show orientation maps of CGP specimens aged for 10 h and 30 h, respectively. In accordance with LOM a partial recrystallization occurs in the material after 10 h of aging and grain size increases up to 30 - 80 µm. Additional aging results in a full recrystallization and grain coarsening. The final average grain size in the area of intense deformation achieves 100 µm.

The texture of the AZ31 magnesium alloy strip is represented by PF in

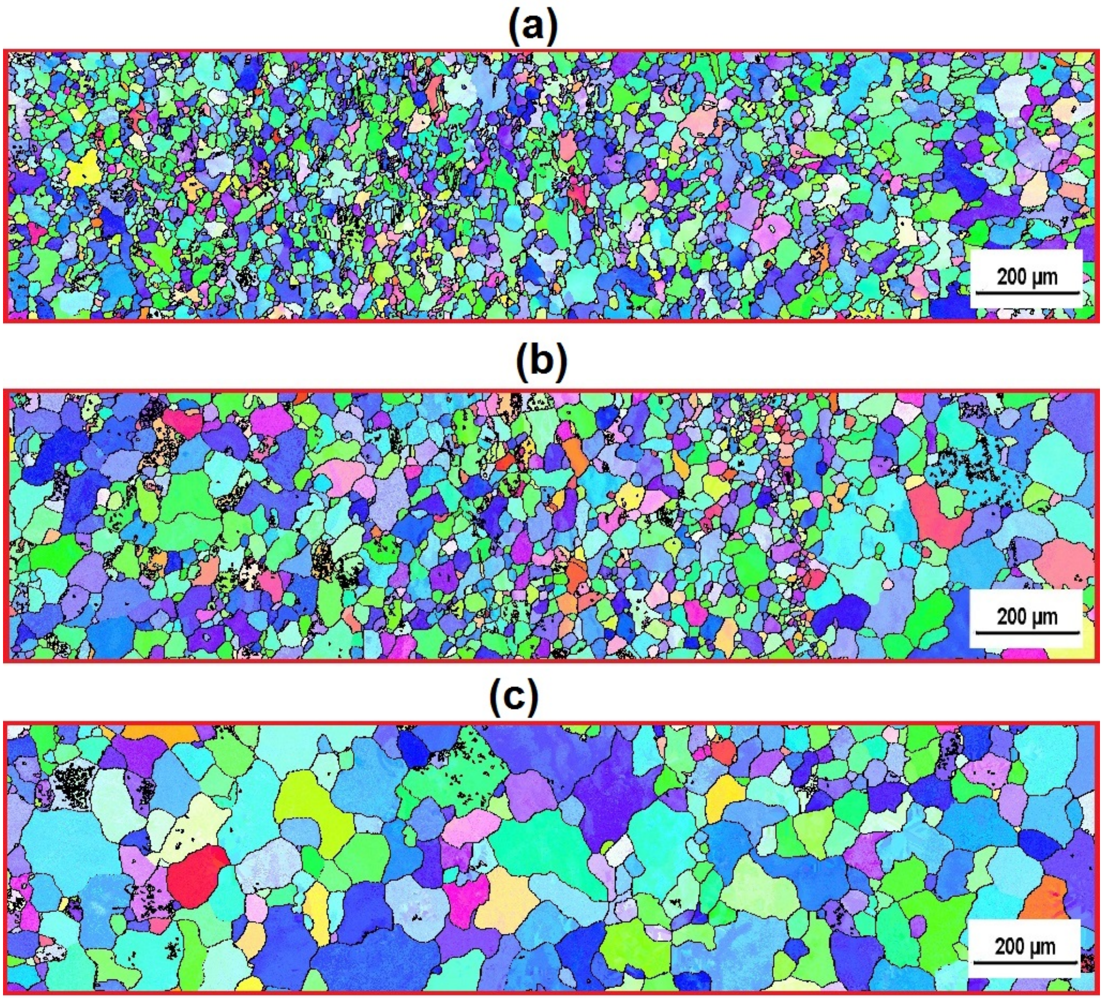

Figure 4.48: EBSD orientation maps of the cross-section of the TRC strip after one CGP cycle: a) without aging and aged at 450 °C for: b) 10 h and c) 30 h.

Fig. 4.49. EBSD measurements show the presence of basal texture in the TRC material after one CGP cycle (Fig. 4.49a) accompanied by a slight rotation of ⟨0001⟩ orientations towards the RD. The texture of the most deformed area of CGP strip is of {0001} basal type. Heat treatment does not significantly change a feature of the texure (Fig. 4.49b,c). Thus, in contrast to ECAP processed samples no weakening of the basal texture is observed.

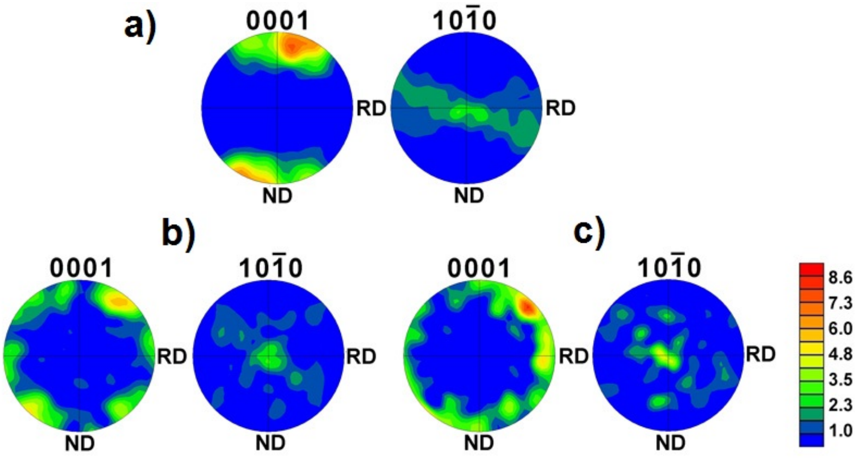

Figure 4.49: Texture evolution of the TRC strip after one CGP cycle: a) as-deformed state and after aging at 450 °C for: b) 10 h and c) 30 h.

Microhardness

Vickers microhardness mapping was made at the cross-section of samples in TD. In Fig. 4.50 changes in local mechanical properties after CGP are presented. The microhardness distribution reflects the geometry of the die. CGP material is heterogeneous along the RD and microhardness values reach the maximum in regions of the most intense plastic deformation.

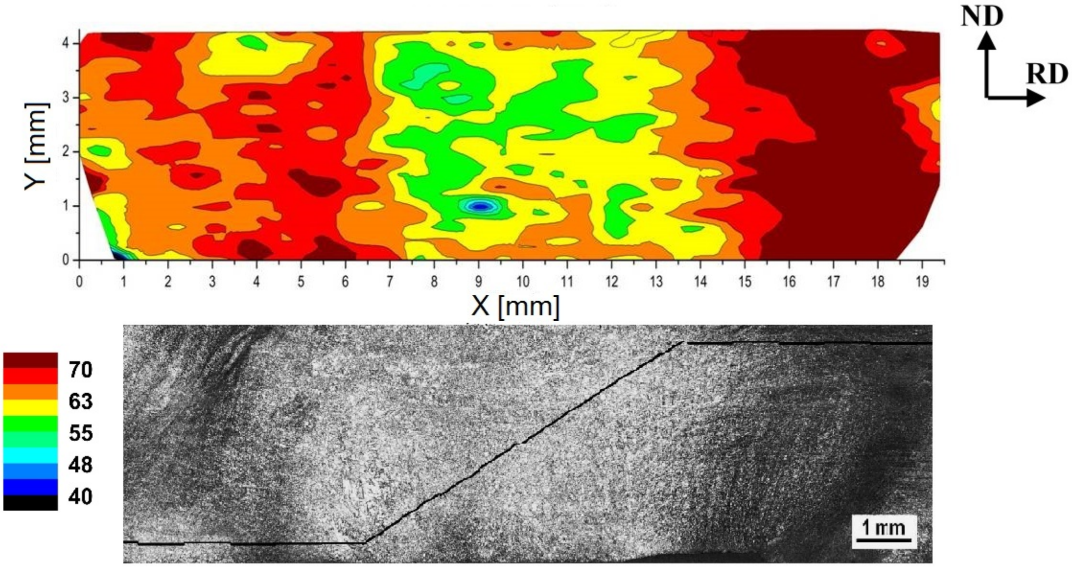

Figure 4.50: Microhardness the AZ31 TRC strip after one CGP cycle in a relation with the microstructure of the cross-section of the sample and a die geometry (black lines).

The evolution of microhardness during annealing in the CGP material is shown in Fig. 4.51 and 4.52. The 8 mm × 5 mm area containing different types of microstructures was measured. Slight softening of the material and elimination of the heterogeneity along the RD occurs with increasing annealing temperature.

The microhardness is relatively low and homogeneous after annealing at 400 °C. Average microhardness is about 55 HV0.1, which is comparable with the one observed in the as-cast material.

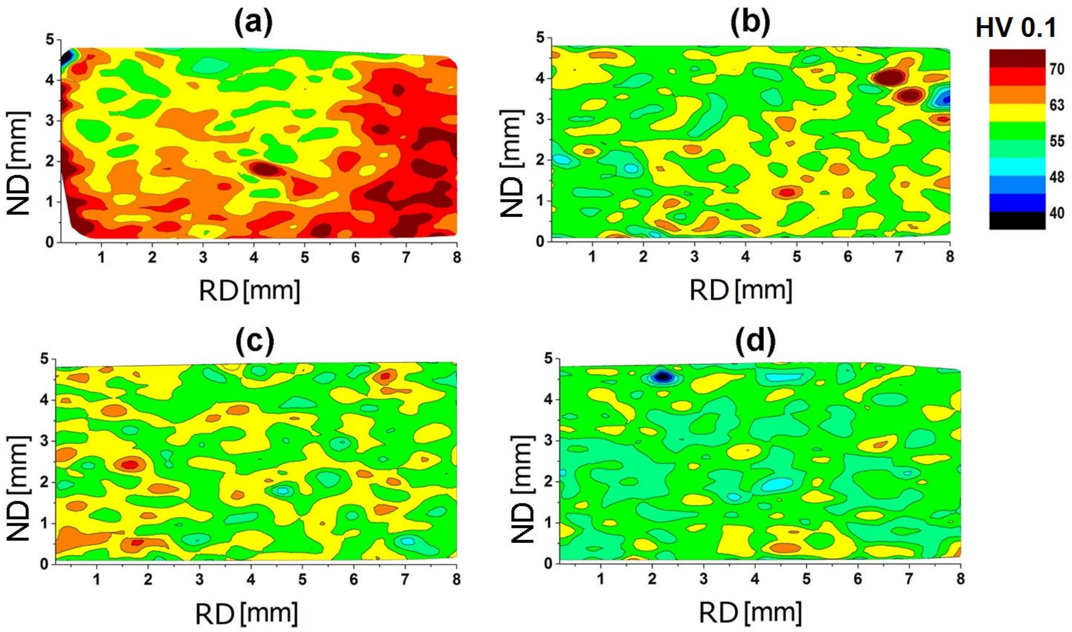

Figure 4.51: Microhardness maps of the TRC strip after a) one CGP cycle and annealing at: b) 250 °C, c) 350 °C and d) 400 °C.

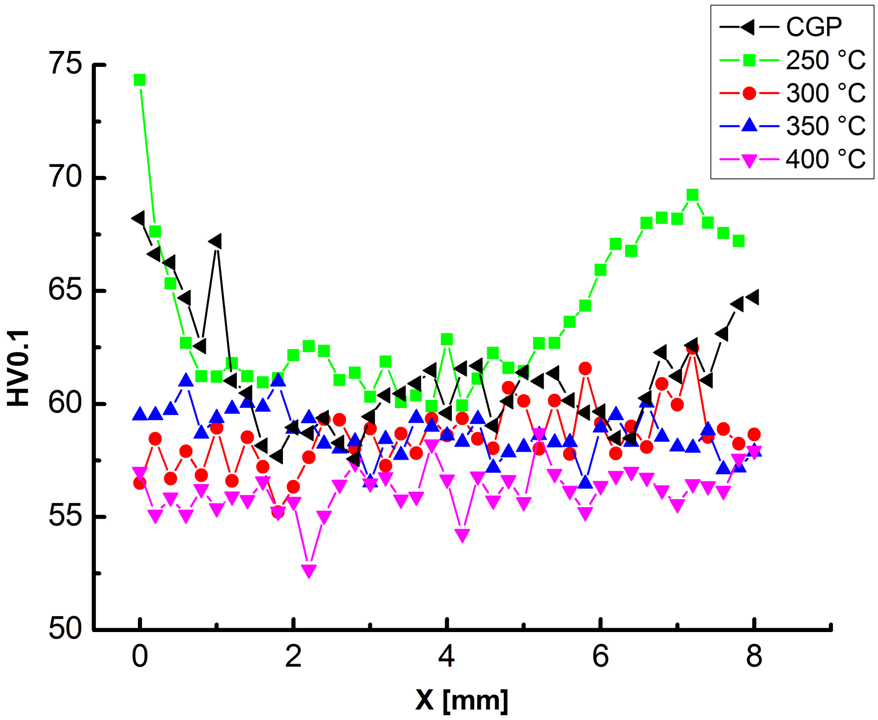

Figure 4.52: Plot summarizing the distribution of microhardness values along the TRC strip in RD processed by one CGP cycle and annealing at 250, 300, 350 and 400 °C.

Additional annealing at 450 °C accompanied by recrystallization and recovery results in a balancing of the distribution of the microhardness (Fig. 4.53b,d). Significant decrease of microhardness down to 55 HV0.1 occurs already after 10 h of aging. Further long-term annealing results in a subsequent slight decrease of microhardness down to 50 HV0.1 and an equalization of microhardness distribution along the strip (Fig. 4.53c,d).

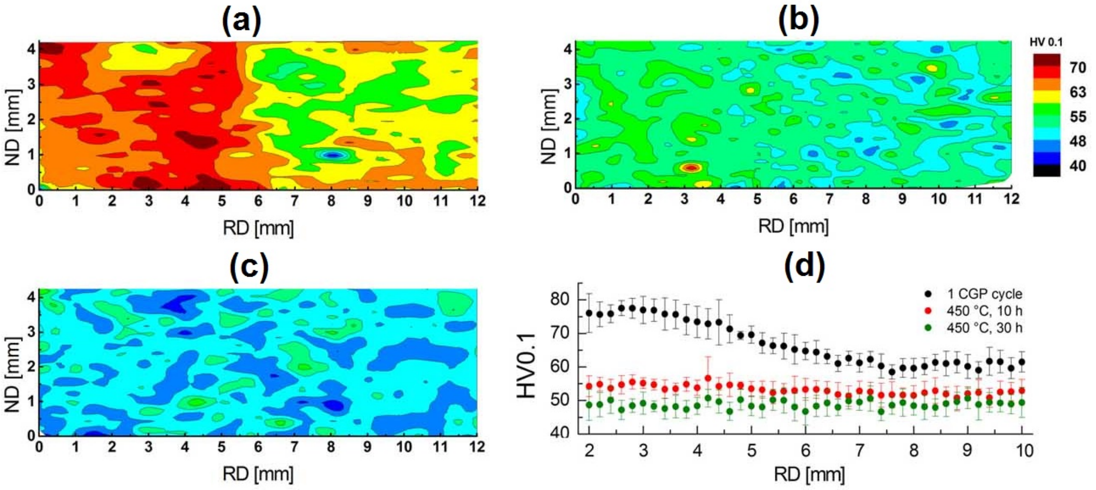

Figure 4.53: Microhardness evolution of the AZ31 TRC strip after one cycle of constrained groove pressing: a) without aging, aging at 450 °C for: b) 10 h and c) 30 h; d) plot summarizing the distribution of HV0.1 values along the strip in RD.

Tensile tests

Fig. 4.54 shows tensile properties of the TRC material after one CGP cycle. Tensile testing at elevated temperatures ranging from 50 to 300 °C was performed. At RT the fracture of CGP samples occurs when the true strain reaches about 2 %. Further increasing of the temperature up to 100 °C leads to a significant increase of ductility. A drop of the ductility at 200 °C similar as in SPD unprocessed TRC materials is observed. And again, at 300 °C the ductility increases up to 20 %.

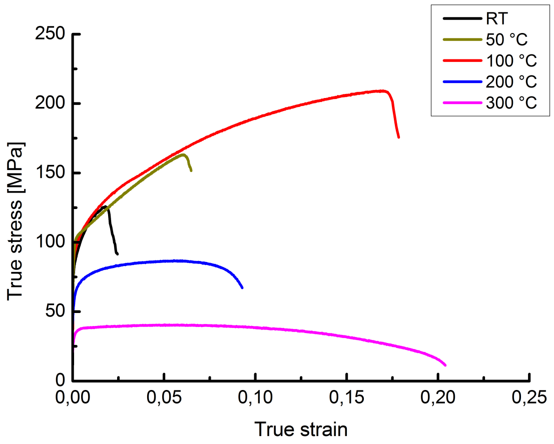

Figure 4.54: Stress-strain curves of CGP samples at indicated deformation temperatures.

LOM after tensile tests

Deformation curves of CGP samples exhibit ductility anomaly at 200 °C similar as in TRC samples. Therefore, LOM observations were done close to the fracture areas (Fig. 4.55). At RT chains of finer grains as well as twins inside larger grains are observed after the tensile test. Higher deformation temperature (100 °C) leads to an intensive twinning as is shown in Fig. 4.55b. At 200 °C much finer grains are present. As it is shown in Fig. 4.55c recrystallized small grains of about 1 µm in diameter are arranged in bands, however, the structure is still bimodal with coarser grains (30 µm). Tension at 300 ° leads to the formation of homogeneous structure with a grain size of about 30 µm (Fig. 4.55d).

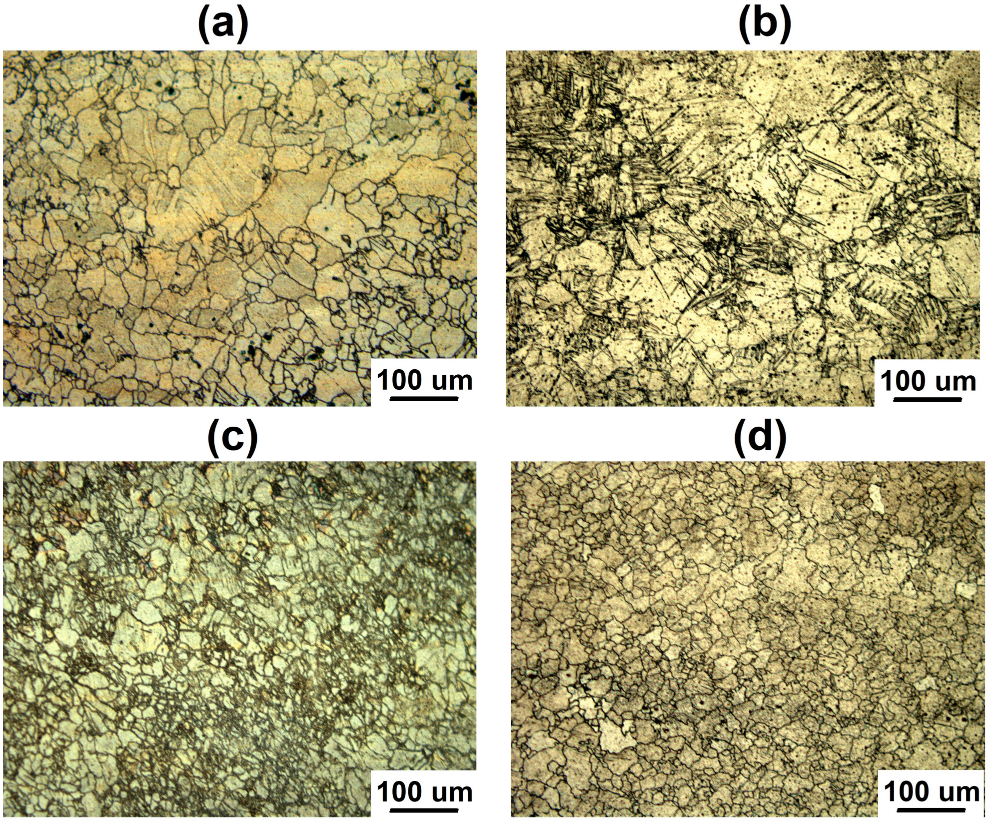

Figure 4.55: Microstructure of the TRC sample after one CGP cycle and tensile tests held at a) RT, b) 100 °C, c) 200 °C and d) 300 °C.

5. Discussion

Microstructure

Microstructural investigation of as-cast AZ31 alloy show that it consists mainly of α-Mg matrix, Al-Mn based intermetallics [203] and β-$Mg_{17}Al_{12}$ phases. The latter has relatively low melting point (approximately 458 °C) and α-Mn type structure. Higher cooling rates of TRC materials result in a formation of well-developed dendrite structure while only coarser β-$Mg_{17}Al_{12}$ particles are homogeneously distributed in a slowly cooled AC samples. Thanks to a high cooling rate also a grain size in TRC materials is remarkably smaller. However, high cooling rate imposes certain inhomogenities into in the TRC strip, such as large elongated grains in the bulk of the strip, finer grains in the area near the surface and central segregation, while AC material exhibits coarse homogeneous structure. Fig. 4.7 clearly shows that conditions used for TRC casting are not optimal. The periodicity of segregation zone (approximately 2 mm) is similar to the one described by Birol [204] for several aluminum alloys. Since segregated channels consist mainly of eutectic phases implying, thus, an enrichment of the liquid central fraction of the material during solidification, similar mechanism of their formation is expected. During the solidification between two-rolls the enriched mushy zone is squeezed between already solidified skins and forced to flow in the direction opposite to the casting direction. Finally, the liquid is trapped by the two skins when they weld together in some points close to the center of the strip leading to the formation of well-defined solute mid channels. The distribution of Al-Mn and $Mg_{17}Al_{12}$ intermetallic particles in segregated channels is not homogeneous along the RD, because small changes of the casting rate can evoke significant changes of the crystallization rate as is generally observed aluminium-magnesium alloys [76].

The redristribution of solute in segregation and in the whole material volume was studied by resistivity measurements during gradual annealing up to 560 °C. The results show that the behavior of AC and TRC alloys differs during heating while homogenization at 450 °C for 10 h leads to an equalization of the microstructure and, thus, resistivity curves of both homogenized materials are quite similar. Results of structural observations indicate that the first resistivity decrease above 120 °C (see Fig. 4.11) is most probably connected with a further depletion of the supersaturated solid solution and enrichment of existing primary phase particles with solutes. A partial precipitation of new particles unrecognizable by SEM could not be excluded. The following increase of resistivity, which starts 280 °C in TRC and 360 °C in AC samples, is generally attributed to the dissolution of existing particles. Different onset of the resistivity increase is probably awaken by different morphology of primary phase particles. A presence of a plateau on the resistivity curve of the TRC sample indicates the dissolution of two phases with different solution temperatures. For the identification of processes occurring during annealing estimations based on the Mathiessen rule (Eq. 3.3) were done. Resulting resistivity of an alloy is defined as a sum of a residual resistivity ρ_0 caused by scattering of electrons on defects and the ideal resistivity governed by scattering of charge carriers by phonons.

A contribution of each alloying element to the resulting resistivity of the alloy can be estimated using resistivity values of $\rho_0(Mg)$ in LN and contributions of other alloying elements (Al, Zn and Mn) to this value known from a literature [205, 206]. Table 5.1 shows contributions to the resistivity of elements present in AZ31 respecting their concentrations. An influence of Na and Fe is considered as negligible due to their low content. It is relatively complicated to find a value of Ca addition contribution to the resistivity of Mg-Al alloy, however, general assumptions based on resistance values of this metal at different temperatures found in a literature and related to its amount in the studied AZ31 alloy (0.034 wt.%) point that under this circumstances the contribution to ρ_0 in LN is possibly quite small and can be omitted in further estimations.

Table 5.1: Resistivity of individual elements contributed to the resulting resistivity of AZ31 alloy

Element	Al	Zn	Mn	Na	Ca	Fe	Mg
Content, wt.%	3.3	0.91	0.34	0.20	0.034	0.020	Rest
Resistivity, nΩm	60	6	4	0.0088		0.0006	5.5

A residual resistivity ρ_0 of Mg is equal to 5.5 nΩm [206]. Ying et al. [207] has calculated the contribution of Al, Zn and Mn to the resistivity of the solid solution in Mg matrix at a temperature range form 2 to 300 K. Using these data the resulting ρ_0 of the AZ31 magnesium alloy in LN can be calculated. If all alloying elements are in a solid solution a value of ρ_0 is present by the Eq. 5.1:

$$\rho_0(AZ31) = \rho_0(Mg) + \rho_0(3\ wt.\%\ Al) + \rho_0(1\ wt.\%\ Zn) + \rho_0(0.3\ wt.\%\ Mn). \quad (5.1)$$

If $\rho_0(Mg)$ is 5.5 nΩm, $\rho_0(3\ wt.\%\ Al)$ is 60 nΩm, $\rho_0(1\ wt.\%\ Zn)$ is 6 nΩm and $\rho_0(0.3\ wt.\%\ Mn)$ is 4 nΩm, the resulting $\rho_0(AZ31)$ is equal to 75.5 nΩm. This value should be considered as an approximate one.

In a case when Al and Mn are not in a solid solution and Zn is fully dissolved in a matrix, the contribution of Al to the relative changes of residual resistivity ρ_0 is:

$$\delta_{Al} = \frac{\rho_0(3.3\%\ Al)}{\rho_0(AZ31) - \rho_0(0.34\%\ Mn) - \rho_0(3.3\%\ Al)} \quad (5.2)$$

and is about 600 % increase of resistivity. This rough estimation shows that due to the rapid solidification large portion of Al remain in the supersaturated solid solution. Our measurements show that the maximum decrease of resistivity due to the particles dissolution is 20-24 % which corresponds to 0.4-0.7 wt.% of Al in the particles and the rest in the solid solution.

Results of resistivity measurements performed on the AZ31 alloy used in a present study show increase of resistivity in both AC and TRC alloys. EDS shows that Zn is dissolved in Mg matrix. Therefore, a 4 % decrease of resistivity starting at about 120 °C in both AC and TRC alloys is most probably caused by the precipitation of β-$Mg_{17}Al_{12}$ phase particles at grain boundaries. However, the reason for a plateau observed in TRC material at 400 °C is not so evident because β-phase Mg-Al particles are already almost dissolved. Earlier studies show the presence of $Al_{11}Mn_4$ and Al_4Mn phases in Mg alloys, which are very stable at elevated temperatures [208, 209]. Nevertheless, Ren et al. [209] has showed that at 400 °C Al-Mn compounds are metastable. According to Mg-Al-Mn phase diagram some of them can be dissolved at temperatures around 500 °C. Moreover, as was already mentioned, Mn and Al from these particles can have a large contribution to the resulting resistivity of AZ31. Thus, it is suggested that the further increase of resistivity at 400 - 540 °C can be attributed to a partially dissolution and transformations of Al-Mn phases.

No significant changes of a microhardness and grain structure were observed in AC material during annealing unless a slight decrease of microhardness of the homogenized AC material is outside an experimental error. The investigation of Hay et al. [210] showed, that the microhardness of β-$Mg_{17}Al_{12}$ phases is higher than the one of the α-Mg matrix and the composite contribution of the β-phase can prevail over the solid solution hardening in the homogenized AC specimen (Fig. 4.20). The homogeneous grain size distribution and coarser grains in AC sample are responsible for lower microhardness values than the ones in the TRC sample (Fig. 4.10). Moreover, the contribution to the dislocation strengthening due to a certain amount of plastic deformation imposed to the TRC material during casting might be significant.

The inhomogeneity of microharness of TRC sample with higher microhardness in regions near the surface and in the central zone of the strip and softer in the bulk of the strip appear as a result of non-equilibrium and non-uniform crystallization during the casting process. High solidification rate and stress imposed by the rolls generate fine grains near the surface. A presence of a large amount of deformation twins in this area confirms this fact. Higher microhardness values of the central zone can be explained by a presence of central segregation zone. During TRC central zone solidifies as the last one and, therefore, the additional deformation is imposed by the already solidified material during the motion of the strip in the gap between the rolls creating thus smaller grains in this region.

Unexpected increase of microhardness of TRC sample after annealing at 100 °C (compare Fig. 4.22 and 4.10) could not be explained by solute atoms redistribution (no change of resistivity were observed). Also an influence of grain structure changes is unlike. Such variations of mechanical properties should be attributed to modifications of dislocations configurations. In general, redistribution of dislocations in light-weight metals in this temperature interval (annihilation of dislocation, incorporating of dislocation in subgrain and grain boundaries, etc.) results in a microhardness decrease. Nevertheless, recent studies [211, 212] performed on fine-grained commercial purity aluminium and aluminium alloys show that annealing at relatively low annealing temperatures can induce a surprising slight increase of microhardness due to the exhaustion of dislocation sources by annihilation of dislocations in subgrain and grain boundaries. Similar process is most probably responsible for the observed increase of microhardness at 100 °C.

Isothermal annealing experiments performed at 450 °C on the TRC sample reflects the recrystallization process occuring in this sample. Annealing was conducted for time intervals from 10 min to 24 h. LOM studies show a presence of newly nucleated grains at the grain boundaries after 10 min of annealing. Growth of these fine grains and nucleation of new ones is observed with increasing annealing time. Fraction of a recrystallized material Y after a hold time t at a given temperature T can be described by Avrami equation (also known as the Jonson-Mehl-Avrami-Kolmogorov, or JMAK, equation) (Eq. 5.3) [213]:

$$Y = 1 - exp(-kt^n), k = \frac{\pi \dot{N} \dot{G}^3}{3}, \tag{5.3}$$

where $\dot{N}$ is a nucleation rate per unit volume and $\dot{G}$ is a rate of a growth, n is Avrami exponent. If a spherical growth considered n is equal to four. Eq. 5.3 can be rewritten into Eq. 5.4:

$$ln(-ln(1 - Y(t))) = lnk + lnn, \tag{5.4}$$

Constants n and k can be determined from a plot of $lnln(\frac{1}{1-Y})$ vs lnt. If the transformation follows the Avrami equation this results in a straight line with gradient n and intercept lnk.

Fig. 5.1 shows plots reflecting the relationship between Y and t during the annealing at 450 °C calculated from LOM micrographs in Fig. 4.15. Two areas of the TRC strip, a bulk and a center, were analyzed. Increasing of annealing time results in an increase of the fraction of new fine grains during static recrystallization (SRX). Evolution of Y as a function of an annealing time is shown in Fig. 5.1a. Typical S-shape curve is observed in both parts of the sample. The saturation takes place after 6 h of annealing. After 6 h of annealing it is relatively difficult to recognize unrecrystallized grains. Additional analysis of recrystallization processes was done using a transformation Eq. 5.4. Fig. 5.1b shows that the Avrami law is not fulfilled neither in the center nor in the bulk of the strip since the displayed points are not aligned along the straight line. The points representing recrystallization flow in the bulk part of the strip do not fulfill a linear fit. Fig. 4.15 indicates the reasons of such non-linear behavior. A nucleation and growth of newly recrystallized grains occur preferentially at grain boundaries resulting in bands of fine grains in the material. Boundaries of these bands are favorable sites for a further nucleation and SRX as is often observed in Mg alloys [214]. This result shows that processes that have not been taken into an account in Avrami analysis occur in the bulk part of the sample. To fulfill the Avrami equation a nucleation should occur randomly and homogeneously over the entire material, a grain growth occurs homogeneously in all directions and a growth rate is independent on the extent of transformation. Although, the above described conditions seem to be accomplished in the central part of the strip, most probably recovery of a dislocation substructure combined with a partial dissolution of the central segregation preceding a "pure" recrystallization are responsible for non-linear fit in Fig. 5.1b. Therefore, the calculation of Avrami coefficients would be formal and is not supported by any physical meaning.

LOM measurements of recrystallized volume fraction can not be carried out with a high accuracy. Therefore, similar analysis could be received from microhardness measurements. Since a driving force for recrystallization is an energy stored in the deformed matrix, the progress of recrystallization can be observed in terms of fractional softening X_H [215]. Thus, Vickers microhardness values from Fig. 4.23 were converted into X_H as defined below:

$$X_H = \frac{H_0 - H_i}{H_0 - H_r}, \tag{5.5}$$

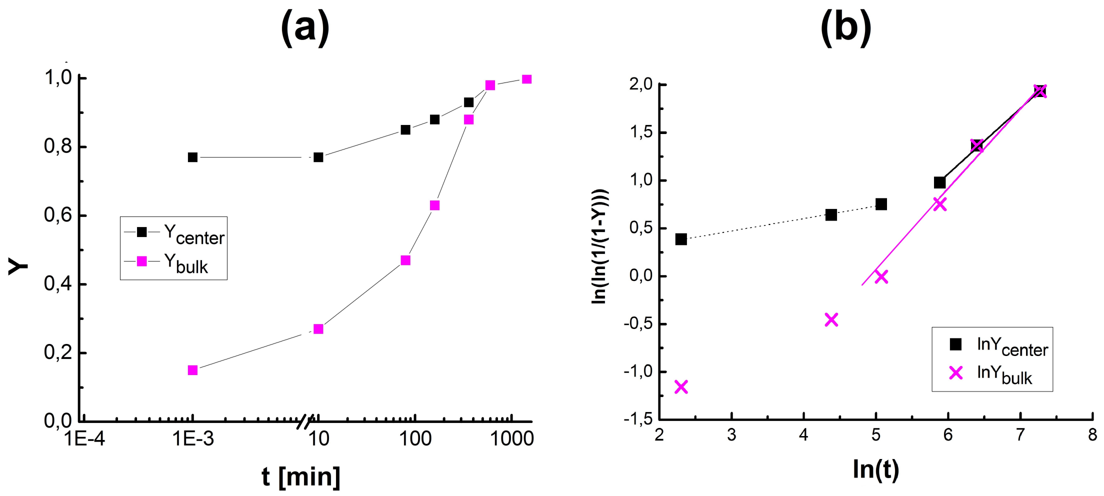

Figure 5.1: Avrami analysis of recrystallization processes occurring in the TRC strip during annealing at 450 °C.

where H_0 is the hardness of the as-cast material, H_i is the hardness measured during isothermal annealing and H_r is the hardness of a fully recrystallized material. The dependence of X_H on annealing time at 450 °C is shown in Fig. 5.2a and measured data are far from a S-shaped sigmoidal curve fit. Consequently a logarithmic plot $lnln(1/(1-X_H))$ against lnt shown in Fig. 5.2b also do not follow a liner fit and thus any coefficients obtained from this measurements should provide unreliable values.

The results obtained using two methods of Avrami coefficients evaluation clearly indicate that a formal application of these methods is not reliable in a case of heterogeneous materials such as TRC strip used in this study.

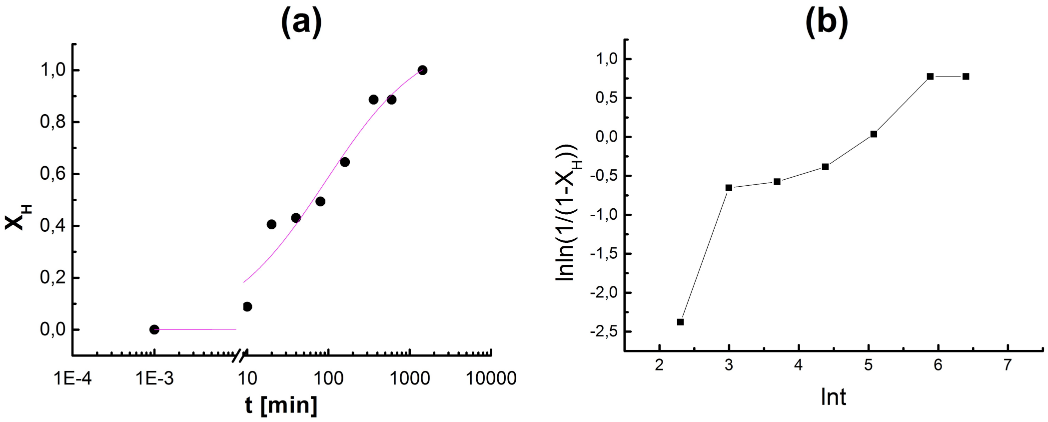

Figure 5.2: Avrami analysis of recrystallization processes occurring in the TRC strip during annealing at 450 °C calculated from microhardness measurements.

Mechanical properties

Tensile properties are usually greatly influenced by the microstructure of the original alloy [82, 128, 130]. Unless there are four deformation modes in magnesium described in the Chapter 1, a homogeneous deformation along c-axis can be provide by only two of them, such as $< c + a >$ slip $\{11\bar{2}2\}\langle 11\bar{2}3\rangle$ and tensile twinning $\{10\bar{1}2\}\langle 10\bar{1}1\rangle$ [15,161]. However, $< c + a >$ mode can not be activated at RT due to the high CRSS. Therefore, AC and TRC magnesium alloys show poor formability at RT.

One of the most important parameters which has an influence on a ductility is a grain size. Generally, coarser grains in hcp materials enhance the strain localization and the ductility decrease. In AC samples this effect is not so clear (Fig. 4.25) because the grain growth in AC sample during homogenization is limited. Therefore, the changes of the samples ductility at RT are negligible. However, a negative role of β-phase dissolution can not be excluded. On the other hand, homogenized TRC alloys exhibit higher formability in both tensile directions mostly due to a decreased grain size (about 50 µm, see Fig. 4.13f and 4.14f) after homogenization (Fig. 4.26).

It was shown by different authors [143,161] that the deformation temperature by as little as 50 °C above RT increases formability of Mg alloys and twins usually appear at temperatures below 150 °C. SEM and AFM observations performed in this study show higher twin activity in the TRC material at 100 °C. However, according to the earlier studies the twinning occurs only at early stages of plastic deformation [214]. Therefore, this mechanism can not be responsible for a substantial increase of the ductility of TRC samples at elevated temperatures. The $< a >$ basal dislocation slip is a dominant deformation mechanism at low deformation temperatures. However, CRSS decreases in non-basal slip systems with increasing deformation temperature enabling the activation of non-basal slip systems and improvement of formability [60]. The anomalous behavior at 200 °C is observed in all materials except homogenized TRC deformed in TD. The decrease of ductility at this temperature which is observed nearly in all samples is an unusual effect for magnesium alloys and will be discussed later in the following paragraph.

Anomalous behavior at 200 °C

Figures 4.25, 4.26 confirm well-known influence of deformation temperature on mechanical properties of magnesium alloys. While YS follows typical features observed in Mg alloys and decreases with increasing deformation temperature due to an activation of non-basal slip systems, an unusual behavior of ductility is observed in AC and TRC materials at about 200 °C. Described behavior is not typical for magnesium alloys. Nevertheless, Zhou et al. has mentioned a slight decrease of elongation at 200 °C in a commercial AZ31B alloy [216] during tension and compression occurring at only one strain rate. Such a behavior is explained by extent DRX occurring at this temperature. However, no significant increase of a volume fraction of DRXed grains is observed at 200 °C compared to 100 °C in this study (Fig. 4.32).

Since the processes responsible for premature failure usually take place in a material after the YS, the analysis of prevailing parts of deformation curves was performed. The Voce equation [217] in Kocks-Mecking approach [218] was used for this aim. The flow curve is assumed as a transient of stress from initial value to the value corresponding to the equilibrium at a given strain rate and temperature. Voce strain hardening equation for true stress σ and true strain ϵ with initial plastic strain $\epsilon_0 = 0$ is:

$$\sigma = \sigma_s - (\sigma_s - \sigma_0)\, exp\left(-\frac{\epsilon}{\epsilon_c}\right), \tag{5.6}$$

where σ_s is a saturation value of stress corresponding to equilibrium, σ_0 is an initial true plastic stress and ϵ_c is a constant.

According to the Kocks-Mecking approach only dislocation structure is responsible for a plastic flow while the twinning is not considered [219]. Work hardening is governed by producing, rearrangement and annihilation of dislocations. Thus, the decrease of work hardening rate Θ with increasing σ is expressed in a following form:

$$\Theta = \frac{d\sigma}{d\epsilon} = \Theta_0\left(1 - \frac{\sigma}{\sigma_s}\right), \tag{5.7}$$

where Θ_0 is an initial work hardening rate at $\sigma = 0$ and σ_s is a saturation stress where $\Theta = 0$.

Fig. 5.3 illustrates a procedure of work hardening rate evaluation using data from true stress (σ) - true strain (ϵ) curves. First, the values of Θ are found by derivation of the plastic part of $\sigma(\epsilon)$ curves at all temperatures at given strain rate (10^{-3} s^{-1}). After that an intercept Θ_0 and a slope $d\Theta/d\sigma$ of an linear fit are calculated as is shown in Fig. 5.3b.

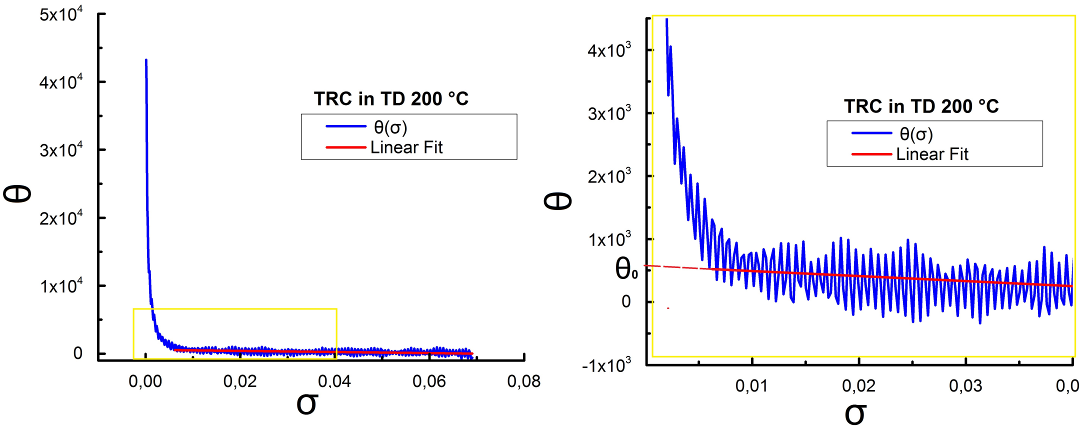

Figure 5.3: Illustration of a work hardening rate (Θ) evaluation procedure.

Temperature dependencies of the work hardening rate derivatives $-d\Theta/d\sigma$ are shown in Fig. 5.4. A pronounced anomaly of $-d\Theta/d\sigma$ at about 200 °C is clearly visible in all investigated samples except for the TRC material deformed in TD. This result clearly indicates a change in deformation mechanisms at this temperature.

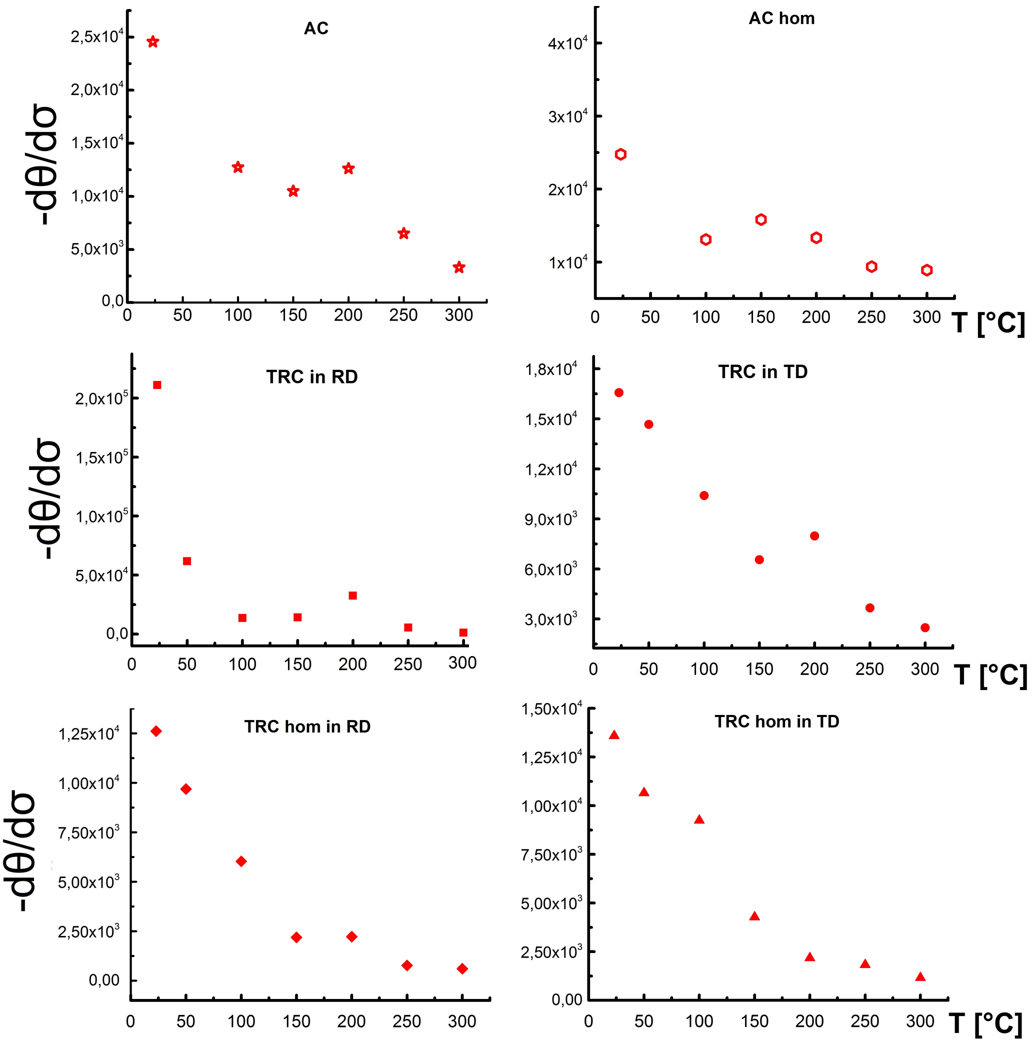

Figure 5.4: Temperature dependence of a work hardening coefficient for studied alloys.

Deeper analysis of deformation video records confirms that at 100 °C firstly only shallow slip traces appear originating most probably only from a prevailing basal slip. Very soon additional slip system is activated limiting the activity of the basal system. As a result a formation of fine shear bands occur homogeneously along the whole specimen gauge. This is confirmed also by AFM studies (Fig. 4.35a). The contribution of DRX and DRV to the plastic flow is considered as insignificant due to the limited fraction of DRXed grains observed at this temperature. Theoretical predictions of Zhou et al. [216] describes the influence of temperature on activity of basal and prismatic slip systems in Mg alloys. At 100 °C the activity of prismatic system increases with a maximal rate and start to prevail already at low strains. At 200 °C the rise of prismatic slip system activity is lower. At the same time the activity of basal slip systems at this temperature dominates till the failure. An influence of DRX and DRV which are favorable for the enhancement of ductility is still confined. The domination of the basal system lasts till 300 °C where its negative influence on ductility is compensated by enhanced DRV and DRX processes. Summarizing, at 200 °C unfavorable mechanisms – dominating basal slip, confined role of prismatic slip system, prevail above favorable ones – DRV and DRX, eventually grain boundary sliding. As a results a localization of strain occurs and ductility of the samples is significantly reduced. The localization was also confirmed by the direct video record and AFM scanning of specimen strained at 200 °C.

ECAP

ECAP was chosen in this study as a SPD technique effectively used for the refinement of magnesium alloys [62,160–162]. Its application on the TRC strip appears an interesting issue in a prospective of the grain refinement.

One ECAP pass leads to the formation of a bimodal microstructure which is in agreement with earlier studies [220]. Areas with high dislocation density, twin and grain boundaries posses much higher stored deformation energy than the rest of the matrix [221] and thus create more nucleation sites for the DRX. The role of the grain boundaries is superior. As a result fine grains of the size of about few microns are formed preferentially on high-angle boundaries of large elongated grains, and in a limited manner also at low-angle boundaries and on twin boundaries (Fig. 4.37). As-cast and homogenized TRC materials before ECAP processing exhibit different microstructure as it is illustrated in Fig. 4.3. Grains in the TRC materials are coarser (150 μm) while SRX occurring during homogenization forms finer dislocation-free grains (50 μm). During the first ECAP pass a higher stored energy in unhomogenized samples (higher dislocation density before ECAP and a presence of coarse β-phase particles) is a reason for the higher number of nucleation sites in this material. Therefore, significantly smaller grains are formed in the as-cast sample. Moreover, their growth is effectively retarded by a presence of $Mg_{17}Al_{12}$ primary particles and Al-Mn intermetallics (caused by Zener drag mechanism [131]) which density is much lower in the homogenized material. The first ECAP pass imposes large strain into both materials, however, recovery is inhibited by the particles in the as-cast sample and again the probability of nucleation of new grains is higher. Thus, the favorable higher number of the nucleation sites, retardation effect of primary particles on the recovery and grain growth result in a presence of smaller grains in as-cast sample after eight ECAP passes.

Fig. 5.5 summarizes microhardness values of samples after SPD of studied materials. Common feature of all those results is a superior microhardness in TRC samples without homogenization. The main contribution to microhardness arises from the grain boundary strengthening and from dislocations. The grain boundary strengthening reflects the grain size distribution in particular samples in accordance with H-P relation (Eq. (1.4)). The direct role of solute atoms and primary particles appears to be marginal.

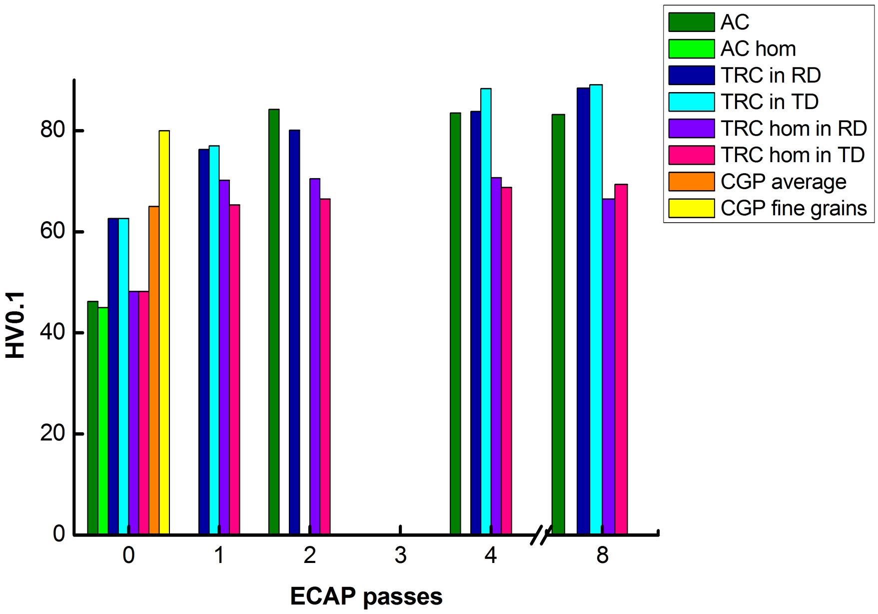

Figure 5.5: Microhardness of TRC alloy after ECAP processing.

However, heterogeneous materials investigated in the present study, where several strengthening mechanisms contribute to mechanical properties, could not be described by such simplified approach represented by H-P relation. This is documented in Fig. 5.6.

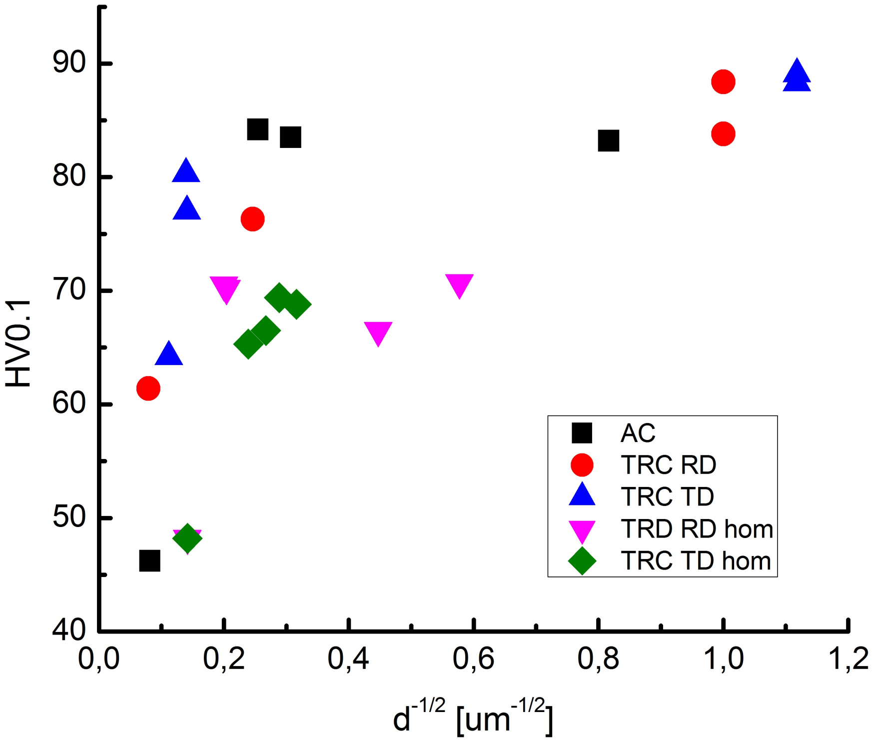

Figure 5.6: Hall-Petch relation curves applied on AZ31.

None of the studied materials fulfill H-P relation for several reasons. For example, for materials after lower number of ECAP passes the presumption of homogeneous grain size distribution is not accomplished. Furthermore, unrecrystallized grains contain numerous dislocations and their contribution should be subtracted before the analysis. The presence of numerous dislocations in unrecrystallized grains can be easily confirmed using KAM method. An example of such an analysis is performed on a TRC strip and on the same strip after ECAP (Fig. 5.7). In the as-cast TRC sample the density of dislocation is higher, which is indicated by higher average misorientation, while in the sample processed by ECAP the majority of grains contain minimal number of dislocations.

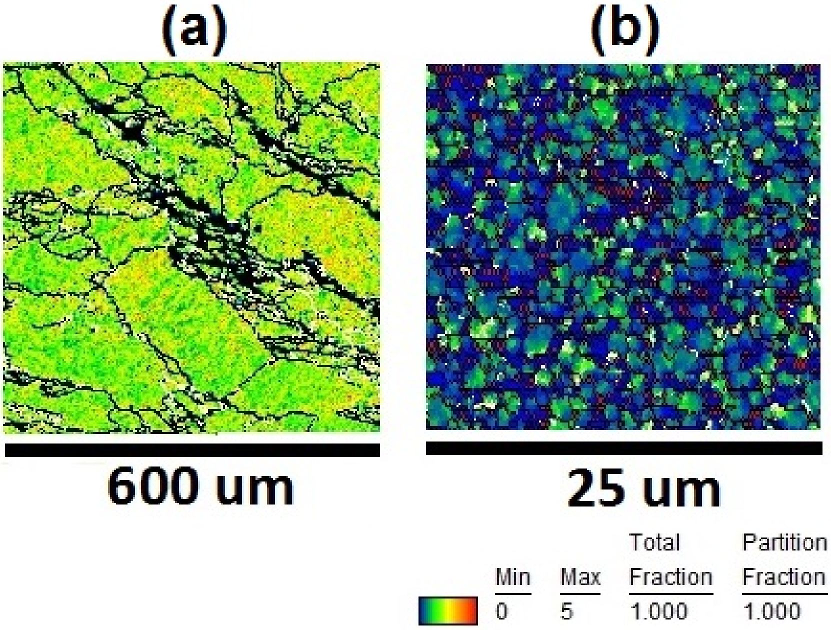

Figure 5.7: KAM maps of a selected bulk area of a) the TRC sample and b) the TRC strip after eight ECAP passes.

The microhardness values of homogenized TRC strip deformed in RD and TD do not significantly change after already one ECAP pass, which might be connected with the annihilation of the dislocation structure during pre-aging and DRV occurred in the heat treated material during SPD. KAM maps were built using EBSD data as is shown in Fig. 5.7. KAM of the selected area in the bulk of the TRC strip shows a presence a high amount of local strain (Fig. 5.7a) compared to the TRC sample after eight ECAP passes in TD of the strip. A majority of grains is fully recrystallized or partially recrystallized with low misorientation values. Nevertheless, misorientation of about 10 % of a volume is high, which means unfinished DRX during ECAP.

After four ECAP passes the microstructure is homogeneous in all TRC samples and the microhardness remains almost the same, except more pronounced increase in TRC sample deformed in RD connected with a slight grain refinement observed after eight ECAP passes.

According to the H-P relation between the grain size and strength (Eq. 1.4), where σ_y is a yield stress, d – average grain diameter, k_y and σ_0 – empirical constants, grain refinement observed in AZ31 alloy samples after ECAP will result in the improvement of mechanical properties. Grain size has an important role in an enhancement of mechanical properties. Fig. 5.6 illustrates H-P relation curves applied on AC and TRC alloys after ECAP. In homogeneous coarse-grained AC alloy low dislocation density is produced during casting. Thus, the contribution of the grain size hardening is significantly less pronounced during the first ECAP pass than the one of dislocations. Dislocations are formed in the material after one pass, which results also in a nucleation of fine grains at grain boundaries and chaining into bands as it was shown by EBSD orientation maps. These dislocations accelerate a nucleation of more grains and DRX after the second pass. Thus, after the second pass the grain boundaries can play an important role. The H-P relation is not accurately fulfilled because of the bimodal structure even after the fourth pass, which complicates evaluation of an average grain size. After eight passes the homogeneous UFG structure is observed, nevertheless, no hardening of AC material occurs due to a slight grain growth as a result of DRX.

TRC materials after ECAP in RD and TD have similar grain size dependence on hardness. Two hardening stages can be distinguieshed. First, a 20 % increase of microhardness after one ECAP pass is caused by the dislocation strengthening. Inhomogeneity and bimodality of the initial structure result in a presence of dislocations in the matrix. The decrease of the grain size down to less than 1 µm in TRC material after four and eight ECAP passes is accompanied by the increase of microhardness. Thus, after one ECAP pass the grain boundary strengthening becomes a main mode.

According to the previous textural studies of magnesium alloys after ECAP processing [64], a formation of a basal texture with maximum located at about 45° from pressing direction in AC sample is observed after already one pass (see Fig. 4.39). It indicates that basal planes are rotated parallel to a shear direction. A strengthening of the basal texture is observed in both as-cast and homogenized TRC specimens after ECAP. It is known, that the operating slip planes after the first ECAP pass are well oriented for a further processing and straining during next passes. Therefore, the texture remains almost unchanged even after eight ECAP passes in all investigated materials. Additional aging at 450 °C after one and eight passes results in an almost full recrystallization leading to the substantive reorientation of the grains and thus to suppression of the initial basal texture.

CGP

The CGP was successfully applied on TRC AZ31 magnesium alloy plate preheated at 450 °C for 10 min. It is shown that the distribution of grain sizes along the plate after one CGP cycle is heterogeneous and varies from 10 to 100 µm. Feng et al. [222] have shown that such a small grain size can be achieved in conventional magnesium alloys not before three ECAP passes at 350 °C and the microstructure of such materials is heterogeneous and four additional passes are necessary to balance the microstructure and make it uniform. On the other hand, instead of the homogeneous bimodality present after ECAP the microstructure observed after one CGP cycle is heterogeneous along the RD. Generally, it can be attributed to the differences in the equivalent strain and shearing given by the geometry of grooves as it is also often observed in Al-based materials [178, 179]. As a result three main areas with different grain sizes can be distinguished in CGP material.

The grain size of the transition area of CGP sample (30 µm) is comparable to the one of wrought magnesium alloys [223]. AZ31 magnesium sheets with grains of 27 μm size can be produced using hot rolling [224]. However, this method is always connected with the thickness reduction (30-35 %) and thus limits repeating treatment. While an insignificant thickness reduction after CGP appears only as an artifact of a small specimen size and subtle material flew at specimen edges.

The bimodal zone is similar to the one after two ECAP passes (Fig. 4.37 and 4.45) and is characterized by an average size of large grains of about 60 μm and 8 μm for the smaller grains. The presence of twins in this area is connected with a shear effect. When grooves press the sample, two areas of opposite surfaces start to be deformed more and the shearing occurs in the non-deformed area followed by the activation of DRX process. It was shown earlier by Figueiredo et al. [225] that such structure is typical for magnesium alloys after four ECAP passes when dynamic recrystallization occurs. On the contrary, in our study after four passes the uniform microstructure is achieved. The origin of such a difference is unlike initial microstructure (TRC in our case, extruded material in [225]).

The grain size of the most deformed area of the CGP plate is 10 μm which is significantly coarser than the one in the TRC sample after four ECAP passes. Obviously, more CGP cycles are necessary to achieve such a fine-grained structure.

The texture of TRC plate after one CGP cycle is of a basal type accompanied by a slight rotation of $\langle 00\bar{1}1\rangle$ orientations towards the RD. This is similar to the texture formed after one and two ECAP passes and is more pronounced than in the TRC material. Aging at 450 °C leads to the grain coarsening and a dispersion of orientations due to the reorientation of grains during SRX process as was shown in PF in Fig. 4.49. As it was discussed previously, the strain imposed after one CGP cycle is approximately equal to the one after one ECAP pass. However, due to the forward and backward straining during CGP the energy stored in the material is considered as lower than after one or more ECAP passes [180]. Consequently, DRX and DRV processes are not so intense during CGP as well as SRX during subsequent aging. That might lead to the fact that the basal texture can not be suppressed. More active recrystallization is expected to occur after more CGP cycles leading to a homogeneously recrystallized microstructure and weakening of the basal texture. A presence of areas with bimodal microstructure similar to ECAP can be considered as a sufficient presumption for expected more significant grain refinement. This assumption is based on results of CGP studies of aluminium, aluminium alloys and steels [178,180,183]. The bimodal structure was also found by Sunil et al. [185] in AZ31 alloy after one GP pass and was eliminated after further straining.

While the TRC material exhibits inhomogeneity of microhardness mainly in the ND of the strip, the CGP material is heterogeneous along the RD (Fig. 4.10 and 4.50). In TRC alloy higher values of microhardness are generally observed in the center of the strip and near both surfaces, i.e. in areas with significantly finer grains. On the contrary, the highest microhardness values in CGP material are observed in the most deformed zone with the grain size of about 10 μm. The microhardness reflects the inhomogeneity of the microstructure and increases after CGP up to 80 HV0.1 in regions of the most intensive deformation, which is comparable with the saturated value of the microhardness after several ECAP passes. The microhardness distribution correlates with observed microstructure and reflects the geometry of the grooved die. Increasing temperature leads to the initiation of SRX, resulting in a slow softening of the material and elimination of the heterogeneity along the RD. The microhardness is relatively low and homogeneous after annealing at 450 °C. Significant decrease of microhardness occurs after 10 h at 450 °C of annealing (Fig. 4.23e and 4.53). Average microhardness of the CGP material is almost 55 HV0.1 while the one for TRC after the same aging time is 45 HV0.1. Thus, thanks to the reduction of the grain size during CGP process and a subsequent aging homogeneous material with the microhardness by almost 20 % higher (when compared with the TRC material) without significant dimension reduction can be received. Further long-term annealing results in a slight decrease of microhardness connected with the grain growth and the secondary recrystallization of the microstructure.

Tensile tests at elevated temperatures show a typical increase of a ductility with the increasing temperature up to 100 °C. At 200 °C a similar anomalous decrease of the ductility as in TRC samples was observed (see Fig. 4.26 and 4.54). Detailed investigation of samples after tensile tests showed that at this temperature the band of finer grains are observed in the CGP sample (Fig. 5.8). A "necklace" grain structure induced by DRX can reduce internal stresses and activate a grain boundary sliding and thus better accommodate plastic strains and increase the ductility of the material. Nevertheless, the coarse-grained structure prevails at this temperature resulting in a presence of unfavorable processes observed also in the TRC material (dominating activity of the basal slip system and limited of the prismatic one) resulting in the low ductility at 200 °C. At higher deformation temperatures DRX and DRV dominate resulting in an increase of ductility.

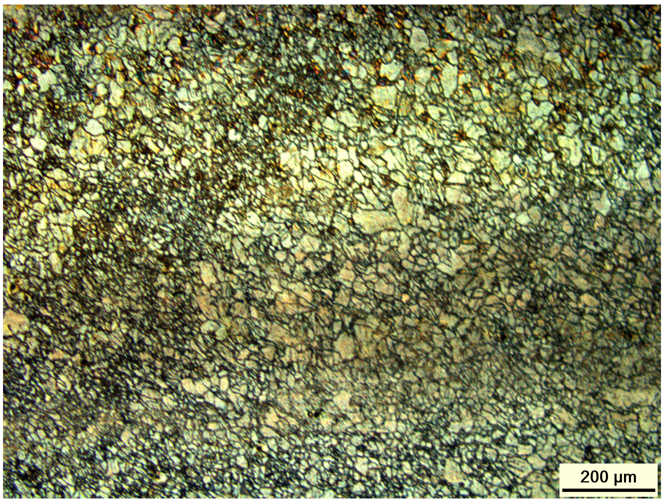

Figure 5.8: "Necklace" bands of finer grains in CGP plate after tensile test at 200 °C.

Conclusion

The present study deals with the investigation of AZ31 magnesium alloy produced by a relatively new TRC technique previously successfully applied on aluminium alloys. The microstructure and mechanical properties of the 5.6 mm thin strip were studied using LOM, SEM, AFM, X-ray diffraction and computed tomography. Microhardness and tensile testing were made in order to study mechanical properties of the strip. Relationships between microstructural features and mechanical properties were examined as well as the influence of the casting direction on the mechanical behavior. The results were compared with the ones obtained on the conventionally cast ingot of a master alloy. In order to modify the initial microstructure, especially the basal texture, two different SPD techniques applied on the TRC strip were tested. This chapter presents main conclusions, achievements of this study and recommendations for a further work on this subject.

- Microstructural study of AC ingot showed a coarse-grained homogeneous microstructure. On the contrary, a heterogeneous structure with large elongated grains tilted along the RD was observed in TRC strip. Due to the deformation imposed by the rotating rolls finer grains are formed in the surface area. Uneven solidification along the strip thickness results in the central segregation zone distributed periodically along the RD of the strip. CLS is responsible for a presence of finer grains also in the center of the TRC strip. 3D X-ray computed tomography revealed that the segregation occurs in a form of bands distanced about 2 mm far from each other.

- Effect of heat treatment on mechanical properties of the strip were studied. Increasing of the temperature up to 100 °C is accompanied by a slight hardening of the TRC material, while further annealing at higher temperatures and aging lead to a softening of the structure as a result of SRX. Tensile test showed that the ductility of the TRC strip is superior in comparison with AC alloy. Homogenization at 450 °C for 10 h deteriorates the ductility of the AC material due to the grain coarsening. On the contrary, the TRC material exhibits an increase of ductility after homogenization caused by the annihilation of dislocation structure, recrystallization and balancing of the microstructure.

- A significant grain refinement was achieved by ECAP processing. The bimodal microstructure in TRC materials (in both RD and TD) vanished after four ECAP passes. In the case of the AC ingot eight passes are necessary to achieve a homogeneous microstructure. Samples homogenized at 450 °C for 10 h before ECAP exhibit coarser microstructure than the ones without pre-heating. Local mechanical properties (microhardness) are improved after ECAP and a favorable suppression of a basal texture after aging is observed.

- The CGP was for the first time successfully applied on a TRC alloy plate. One full CGP cycle was accomplished on a sample with the RD parallel to grooves. A reduction of the thickness after CGP was insignificant. Heterogeneity of the microstructure along the ND of the TRC material typical for this technique is replaced by the heterogeneity along the RD. This inhomogeneity can be eliminated by a subsequent aging. Nevertheless, tensile properties are not significantly improved by CGP, initial basal texture is stronger and can not be weakened by a further heat treatment.

- Anomalous tensile behavior of TRC samples and samples after CGP was observed at 200 °C and confirmed using Kocks-Mecking approach. Decrease of the ductility was associated with the change of deformation mechanisms in the materials. Namely, a dominated basal slip is less confined by a prismatic slip, which becomes less active with increasing deformation temperature. On the contrary, a favorable contribution of DRV and DRX prevailing at higher temperatures is not sufficient to overcome the above mentioned negative influence of basal slip system.

Future work

- Further CGP processing is believed to eliminate a heterogeneity of the microstructure of the CGP plate and improve mechanical properties. The suppression or weakening of the basal texture is also expected with more CGP cycles.
- More detailed study of nucleation processes and DRX during CGP and their influence on the resulting microstructure and texture appears to be a prospective subject for the further investigation of innovative SPD technique, which, as it was shown in this thesis, can be easily applied to magnesium strip to achieve a variety of new UFG materials.

Bibliography

[1] https://www.webelements.com/magnesium/history.html, “Magnesium: historical information, webelements.”

[2] B. Mordike and T. Ebert, “Magnesium,” *Materials Science and Engineering: A*, vol. 302, no. 1, pp. 37–45, 2001.

[3] I. M. Association, “Desulfurizing steel: Magnesium is the reagent of choice,” *Mg showcase*, vol. 19, pp. 1–4, 2012.

[4] J. C. W. Gerd Lütjering, *Titanium.* Springer Berlin Heidelberg, 2007.

[5] M. M. Avedesian, H. Baker, *et al.*, “Asm specialty handbook: magnesium and magnesium alloys,” *ASM International, Materials Park, OH*, p. 15, 1999.

[6] H.-l. Zhao, Z.-x. Zhou, X.-d. Liu, and S.-k. Guan, “Influence of mg 3 n 2 powder on microstructures and mechanical properties of az31 mg alloy,” *Journal of Central South University of Technology*, vol. 15, pp. 459–462, 2008.

[7] S. Schumann and H. E. Friedrich, “Current and future use of magnesium in the automobile industry,” in *Materials Science Forum*, vol. 419, pp. 51–56, Trans Tech Publ, 2003.

[8] A. A. Luo, “Recent magnesium alloy development for automotive powertrain applications,” in *Materials Science Forum*, vol. 419, pp. 57–66, Trans Tech Publ, 2003.

[9] G. Faraji, O. Dastani, and S. A. Mousavi, “Microstructures and mechanical properties of al2o3/az91 surface nanocomposite layer produced by friction stir processing,” *Proceedings of the Institution of Mechanical Engineers, Part B: Journal of Engineering Manufacture*, vol. 225, no. 8, pp. 1331–1345, 2011.

[10] D. Vojtěch, V. Knotek, and P. Novák, “Electrochemical hydriding of mg-based alloys,” in *Defect and Diffusion Forum*, vol. 312, pp. 882–887, Trans Tech Publ, 2011.

[11] A. A. Luo and B. R. Powell, “Tensile and compressive creep of magnesium-aluminum-calcium based alloys,” *Magnesium Technology 2001*, pp. 137–144, 2001.

[12] E. Aghion and B. Bronfin, “Magnesium alloys development towards the 21st century,” in *Materials Science Forum*, vol. 350, pp. 19–30, Trans Tech Publ, 2000.

[13] R. Gehrmann, M. M. Frommert, and G. Gottstein, “Texture effects on plastic deformation of magnesium,” *Materials Science and Engineering: A*, vol. 395, no. 1–2, pp. 338 – 349, 2005.

[14] H. Wang, P. Wu, and M. Gharghouri, “Effects of basal texture on mechanical behaviour of magnesium alloy az31b sheet,” *Materials Science and Engineering: A*, vol. 527, no. 15, pp. 3588–3594, 2010.

[15] Y. Wang and J. Huang, “Texture analysis in hexagonal materials,” *Materials Chemistry and Physics*, vol. 81, no. 1, pp. 11 – 26, 2003.

[16] M. Furukawa, Z. Horita, M. Nemoto, and T. Langdon, “Review: Processing of metals by equal-channel angular pressing,” *Journal of Materials Science*, vol. 36, no. 12, pp. 2835–2843, 2001.

[17] G. V. Raynor, *The physical metallurgy of magnesium and its alloys*, vol. 5. Pergamon, 1959.

[18] K. U. Kainer and F. Kaiser, “Magnesium alloys and technology,” 2003.

[19] J. Koike, T. Kobayashi, T. Mukai, H. Watanabe, M. Suzuki, K. Maruyama, and K. Higashi, "The activity of non-basal slip systems and dynamic recovery at room temperature in fine-grained AZ31B magnesium alloys," *Acta Materialia*, vol. 51, no. 7, pp. 2055–2065, 2003.

[20] A. Akhtar and E. Teghtsoonian, "Solid solution strengthening of magnesium single crystals— the effect of solute on the ease of prismatic slip," *Acta Metallurgica*, vol. 17, no. 11, pp. 1351 – 1356, 1969.

[21] S. Graff, "Micromechanical modeling of the deformation of hcp metals (vom promotionsausschuss der fakultat v: Verkehrs-und maschinensysteme der technischen universitat berlin im jahr 2007 als dissertation angenommene arbeit)," *GKSS FORSCHUNGSZENTRUM GEESTHACHT GMBH-PUBLICATIONS-GKSS*, vol. 1, no. 1, pp. ALL–ALL, 2007.

[22] A. Luque, M. Ghazisaeidi, and W. Curtin, "Deformation modes in magnesium (0001) and (01-11) single crystals: simulations versus experiments," *Modelling and Simulation in Materials Science and Engineering*, vol. 21, no. 4, p. 045010, 2013.

[23] S. Liu, L. Liu, and L. Kang, "Refinement role of electromagnetic stirring and strontium in az91 magnesium alloy," *Journal of Alloys and Compounds*, vol. 450, no. 1, pp. 546–550, 2008.

[24] H. K. Lim, D. H. Kim, J. Y. Lee, W. T. Kim, and D. H. Kim, "Effects of alloying elements on microstructures and mechanical properties of wrought mg–mm–sn alloy," *Journal of Alloys and Compounds*, vol. 468, no. 1, pp. 308–314, 2009.

[25] Y. Huang, H. Dieringa, N. Hort, T. A. Leil, K. U. Kainer, and Y. Liu, "Effects of segregation of primary alloying elements on the creep response in magnesium alloys," *Scripta Materialia*, vol. 58, no. 10, pp. 894–897, 2008.

[26] K. Hirai, H. Somekawa, Y. Takigawa, and K. Higashi, "Effects of ca and sr addition on mechanical properties of a cast az91 magnesium alloy at room and elevated temperature," *Materials Science and Engineering: A*, vol. 403, no. 1, pp. 276–280, 2005.

[27] Y.-l. Cheng, T.-w. Qin, H.-m. Wang, and Z. Zhang, "Comparison of corrosion behaviors of az31, az91, am60 and zk60 magnesium alloys," *Transactions of Nonferrous Metals Society of China*, vol. 19, no. 3, pp. 517–524, 2009.

[28] Y. Chino, T. Hoshika, and M. Mabuchi, "Mechanical and corrosion properties of az31 magnesium alloy repeatedly recycled by hot extrusion," *Materials transactions*, vol. 47, no. 4, pp. 1040–1046, 2006.

[29] W. K. Miller, "Creep of die cast az91 magnesium at room temperature and low stress," *Metallurgical Transactions A*, vol. 22, no. 4, pp. 873–877, 1991.

[30] E. F. Emley, "Principles of magnesium technology," 1966.

[31] P. Cao, M. Qian, and D. H. StJohn, "Effect of manganese on grain refinement of mg–al based alloys," *Scripta Materialia*, vol. 54, no. 11, pp. 1853 – 1858, 2006.

[32] O. Lunder, T. K. Aune, and K. Nisancioglu, "Effect of mn additions on the corrosion behavior of mould-cast magnesium astm az91," *Corrosion*, vol. 43, no. 5, pp. 291–295, 1987.

[33] Y. Tamura, Y. Kida, H. Tamehiro, N. Kono, H. Soda, and A. McLean, "The effect of manganese on the precipitation of mg17al12 phase in magnesium alloy az 91," *Journal of Materials Science*, vol. 43, no. 4, pp. 1249–1258, 2008.

[34] A. Luo and M. Pekguleryuz, "Cast magnesium alloys for elevated temperature applications," *Journal of Materials Science*, vol. 29, no. 20, pp. 5259–5271, 1994.

[35] M. Qian and A. Das, "Grain refinement of magnesium alloys by zirconium: Formation of equiaxed grains," *Scripta Materialia*, vol. 54, no. 5, pp. 881 – 886, 2006. Viewpoint set no. 39: Statistical mechanics and coarse graining of dislocation behavior for continuum plasticity.

[36] G. Foerster, "Improved magnesium die casting alloys," in *Eight international die casting exposition and congress. Detroit*, 1975.

[37] E. E. Schmid, K. von Oldenburg, and G. Frommeyer, "Microstructure and properties of as-cast intermetallic mg2si-al alloys," *Zeitschrift für Metallkunde*, vol. 81, no. 11, pp. 809–815, 1990.

[38] S. Beer, G. Frommeyer, E. Schmid, *et al.*, "Magnesium alloys and their applications," *DGM Informationsgesellschaft mbH, Oberusel*, vol. 317, 1992.

[39] A. K. Dahle, Y. C. Lee, M. D. Nave, P. L. Scha, and D. H. Stjohn, "Development of the as-cast microstructure in magnesium ± aluminium alloys," *Journal of Light Metals*, vol. 1, pp. 61–72, 2001.

[40] I. J. Polmear, "Light alloys- metallurgy of the light metals//((book))," *London and New York, Edward Arnold, 1989, 288*, 1989.

[41] Q. Han, B. K. Kad, and S. Viswanathan, "Design perspectives for creep-resistant magnesium die-casting alloys," *Philosophical Magazine*, vol. 84, no. 36, pp. 3843–3860, 2004.

[42] M. Dargusch, G. Dunlop, and K. Pettersen, "Prot: Conf. on magnesium alloys and their applications. werkstoff-informationsgesellschaft mbh," *Wolsburg. Germany*, pp. 77–82, 1998.

[43] A. A. Luo, "Recent magnesium alloy development for elevated temperature applications," *International materials reviews*, vol. 49, no. 1, pp. 13–30, 2004.

[44] H. Haferkamp, F. Bach, V. Kaese, K. Möhwald, M. Niemeyer, H. Schreckenberger, P.-T. Tai, *et al.*, "Magnesium corrosion–processes, protection of anode and cathode," *Magnesium-Alloys and Technology*, pp. 226–241, 2003.

[45] B. L. Mordike and P. Lukáč, "Physical metallurgy," in *Magnesium Technology*, pp. 63–107, Springer Berlin Heidelberg, 2006.

[46] S. Zhang, X. Zhang, C. Zhao, J. Li, Y. Song, C. Xie, H. Tao, Y. Zhang, Y. He, Y. Jiang, and Y. Bian, "Research on an mg–zn alloy as a degradable biomaterial," *Acta Biomaterialia*, vol. 6, no. 2, pp. 626 – 640, 2010.

[47] C. P. Luo, J. W. Liu, and H. W. Liu, "Effects of al/zn ratio on the microstructure and strengthening of mg-al-zn alloys," in *Materials Science Forum*, vol. 488, pp. 205–210, Trans Tech Publ, 2005.

[48] J. L. Murray, "The al- mg (aluminum- magnesium) system," *Bulletin of Alloy Phase Diagrams*, vol. 3, no. 1, pp. 60–74, 1982.

[49] J. Park and L. Wyman, "Phase relationships in magnesium alloys. period covered: December 1954 to august 1957," tech. rep., National Bureau of Standards, Washington, DC, 1957.

[50] P. Gunde, A. Hänzi, A. Sologubenko, and P. Uggowitzer, "High-strength magnesium alloys for degradable implant applications," *Materials Science and Engineering: A*, vol. 528, no. 3, pp. 1047–1054, 2011.

[51] B. Zhang, Y. Hou, X. Wang, Y. Wang, and L. Geng, "Mechanical properties, degradation performance and cytotoxicity of mg–zn–ca biomedical alloys with different compositions," *Materials Science and Engineering: C*, vol. 31, no. 8, pp. 1667–1673, 2011.

[52] P. Kurze, H. Friedrich, and B. Mordike, “Magnesium technology, metallurgy, design data, applications,” *by HE Friedrich and BL Mordike, Springer-Verlag, Berlin*, 2006.

[53] L. Gao, R. Chen, and E. Han, “Effects of rare-earth elements gd and y on the solid solution strengthening of mg alloys,” *Journal of Alloys and Compounds*, vol. 481, no. 1–2, pp. 379 – 384, 2009.

[54] L. Wei, G. Dunlop, and H. Westengen, “Development of microstructure in cast mg–ai–rare earth alloys,” *Materials Science and Technology*, vol. 12, no. 9, pp. 741–750, 1996.

[55] I. Polmear, “Magnesium alloys and applications,” *Materials science and technology*, vol. 10, no. 1, pp. 1–16, 1994.

[56] Y. Lü, Q. Wang, X. Zeng, W. Ding, C. Zhai, and Y. Zhu, “Effects of rare earths on the microstructure, properties and fracture behavior of mg–al alloys,” *Materials Science and Engineering: A*, vol. 278, no. 1–2, pp. 66 – 76, 2000.

[57] L. Wei and G. Dunlop, “The solidification behaviour of mg-al-rare earth alloys,” *Journal of Alloys and Compounds*, vol. 232, no. 1–2, pp. 264 – 268, 1996.

[58] R. Armstrong, “The influence of polycrystal grain size on several mechanical properties of materials,” *Metallurgical and Materials Transactions*, vol. 1, no. 5, pp. 1169–1176, 1970.

[59] N. N. Aung and W. Zhou, “Effect of grain size and twins on corrosion behaviour of az31b magnesium alloy,” *Corrosion Science*, vol. 52, no. 2, pp. 589–594, 2010.

[60] A. Jain, O. Duygulu, D. Brown, C. Tomé, and S. Agnew, “Grain size effects on the tensile properties and deformation mechanisms of a magnesium alloy, az31b, sheet,” *Materials Science and Engineering: A*, vol. 486, no. 1, pp. 545–555, 2008.

[61] H. Watanabe, T. Mukai, M. Kohzu, S. Tanabe, and K. Higashi, “Effect of temperature and grain size on the dominant diffusion process for superplastic flow in an az61 magnesium alloy,” *Acta materialia*, vol. 47, no. 14, pp. 3753–3758, 1999.

[62] T. Mukai, M. Yamanoi, H. Watanabe, and K. Higashi, “Ductility enhancement in az31 magnesium alloy by controlling its grain structure,” *Scripta Materialia*, vol. 45, no. 1, pp. 89–94, 2001.

[63] H. Somekawa and T. Mukai, “Effect of grain refinement on fracture toughness in extruded pure magnesium,” *Scripta materialia*, vol. 53, no. 9, pp. 1059–1064, 2005.

[64] J. Del Valle, F. Carreño, and O. A. Ruano, “Influence of texture and grain size on work hardening and ductility in magnesium-based alloys processed by ecap and rolling,” *Acta Materialia*, vol. 54, no. 16, pp. 4247–4259, 2006.

[65] D. Song, A. Ma, J. Jiang, P. Lin, D. Yang, and J. Fan, “Corrosion behavior of equal-channel-angular-pressed pure magnesium in nacl aqueous solution,” *Corrosion Science*, vol. 52, no. 2, pp. 481 – 490, 2010.

[66] N. Birbilis, K. Ralston, S. Virtanen, H. Fraser, and C. Davies, “Grain character influences on corrosion of ecaped pure magnesium,” *Corrosion Engineering Science and Technology*, vol. 45, no. 3, pp. 224–230, 2010. cited By 44.

[67] H. Watanabe, A. Takara, H. Somekawa, T. Mukai, and K. Higashi, “Effect of texture on tensile properties at elevated temperatures in an AZ31 magnesium alloy,” *Scripta Materialia*, vol. 52, no. 6, pp. 449–454, 2005.

[68] Y. Tamura, Y. Kida, H. Tamehiro, N. Kono, H. Soda, and A. McLean, “The effect of manganese on the precipitation of mg17al12 phase in magnesium alloy az91,” *Journal of Materials Science*, vol. 43, no. 4, pp. 1249–1258, 2008.

[69] K. MIZUNO, S. FURUTANI, S. YOKOTA, and T. FUKUSAKO, “Effect of casting modulus on mechanical strength and dendrite arm spacing of ac4b flat aluminum alloy castings,” *Journal of Japan Institute of Light Metals*, vol. 46, no. 2, pp. 55–60, 1996.

[70] D. McCartney and J. Hunt, “Measurements of cell and primary dendrite arm spacings in directionally solidified aluminium alloys,” *Acta Metallurgica*, vol. 29, no. 11, pp. 1851–1863, 1981.

[71] M. Flemings, T. Kattamis, B. Bardes, *et al.*, “Dendrite arm spacing in aluminum alloys,” *AFS Transactions*, vol. 99, pp. 501–506, 1991.

[72] A. M. Samuel and F. H. Samuel, “Effect of alloying elements and dendrite arm spacing on the microstructure and hardness of an al-si-cu-mg-fe-mn (380) aluminium die-casting alloy,” *Journal of Materials Science*, vol. 30, no. 7, pp. 1698–1708.

[73] C. Do Lee and K. S. Shin, “Effects of precipitate and dendrite arm spacing on tensile properties and fracture behavior of as-cast magnesium-aluminum alloys,” *Metals and Materials International*, vol. 9, no. 1, pp. 21–27, 2003.

[74] K. Radhakrishna, S. Seshan, and M. Seshadri, “Dendrite arm spacing in aluminum alloy casting,” *AFS Transactions*, vol. 88, pp. 695–702, 1980.

[75] S. Lun Sin, A. Elsayed, and C. Ravindran, “Inclusions in magnesium and its alloys: a review,” *International Materials Reviews*, vol. 58, no. 7, pp. 419–436, 2013.

[76] S. Das, N. Lim, J. Seol, H. Kim, and C. Park, “Effect of the rolling speed on microstructural and mechanical properties of aluminum–magnesium alloys prepared by twin roll casting,” *Materials & Design*, vol. 31, no. 3, pp. 1633–1638, 2010.

[77] Q. Wang, D. Apelian, and D. Lados, “Fatigue behavior of a356-t6 aluminum cast alloys. part i. effect of casting defects,” *Journal of Light Metals*, vol. 1, no. 1, pp. 73–84, 2001.

[78] S. Thompson, “Mengsc thesis,” *The University of Queensland, Brisbane, Australia*, 1998.

[79] A. Dahle, S. Sannes, D. S. John, and H. Westengen, “Formation of defect bands in high pressure die cast magnesium alloys,” *Journal of Light Metals*, vol. 1, no. 2, pp. 99–103, 2001.

[80] S. S. Park, W.-J. Park, C. Kim, B. You, and N. J. Kim, “The twin-roll casting of magnesium alloys,” *JOM*, vol. 61, no. 8, pp. 14–18, 2009.

[81] J. Bae, M. Shim, B. Suh, D. Kim, S. Park, and N. J. Kim, “Segregation in twin-roll cast mg alloy and its suppression through alloy design,” *Materials Letters*, vol. 132, pp. 361–364, 2014.

[82] S. S. Park, G. Bae, D. Kang, I.-H. Jung, K. Shin, and N. J. Kim, “Microstructure and tensile properties of twin-roll cast mg–zn–mn–al alloys,” *Scripta Materialia*, vol. 57, no. 9, pp. 793–796, 2007.

[83] M. Ferry, *Direct strip casting of metals and alloys.* Woodhead Publishing, 2006.

[84] Z. Bian, I. Bayandorian, H. Zhang, G. Scamans, and Z. Fan, “Extremely fine and uniform microstructure of magnesium az91d alloy sheets produced by melt conditioned twin roll casting,” *Materials Science and Technology*, vol. 25, no. 5, pp. 599–606, 2009.

[85] A. Dahle and D. StJohn, “Rheological behaviour of the mushy zone and its effect on the formation of casting defects during solidification,” *Acta Materialia*, vol. 47, no. 1, pp. 31 – 41, 1998.

[86] A. Dahle and L. Arnberg, “Development of strength in solidifying aluminium alloys,” *Acta Materialia*, vol. 45, no. 2, pp. 547 – 559, 1997.

[87] C. Caceres and B. Selling, “Casting defects and the tensile properties of an al si mg alloy,” *Materials Science and Engineering: A*, vol. 220, no. 1, pp. 109–116, 1996.

[88] C. Do Lee, “Dependence of tensile properties of am60 magnesium alloy on microporosity and grain size,” *Materials Science and Engineering: A*, vol. 454, pp. 575–580, 2007.

[89] M. Surappa, E. Blank, and J. Jaquet, “Effect of macro-porosity on the strength and ductility of cast al 7si 0.3 mg alloy,” *Scripta Metallurgica*, vol. 20, no. 9, pp. 1281–1286, 1986.

[90] J. Weiler, J. Wood, R. Klassen, E. Maire, R. Berkmortel, and G. Wang, “Relationship between internal porosity and fracture strength of die-cast magnesium {AM60B} alloy,” *Materials Science and Engineering: A*, vol. 395, no. 1–2, pp. 315 – 322, 2005.

[91] A. Gokhale and G. Patel, “Origins of variability in the mechanical properties of am60 magnesium alloy castings,” pp. 195–199, 2001. cited By 2.

[92] S. K. Das and M. H. Skillingberg, *Aluminum 2002: Proceedings of the TMS 2002 Annual Meeting: Automotive Alloys, and AluminumSheet and Plate Rolling and Finishing Technology Symposia: Proceedings of Symposia: Held at the TMS 2002 Annual Meeting in Seattle, Washington, USA, February18-21, 2002.* Tms, 2002.

[93] C. Huang, C. Cheng, C. Chou, and F. Chen, “Hot cracking in az31 and az61 magnesium alloy,” *Journal of Materials Science & Technology*, vol. 27, no. 7, pp. 633–640, 2011.

[94] R. Lumley, T. Sercombe, and G. Schaffer, “Surface oxide and the role of magnesium during the sintering of aluminum,” *Metallurgical and Materials Transactions A*, vol. 30, no. 2, pp. 457–463, 1999.

[95] J. Hanawalt, C. Nelson, and J. Peloubet, “Corrosion studies of magnesium and its alloys,” *trans. AIME*, vol. 147, pp. 273–299, 1942.

[96] B. Xing, Y. Li, J. Feng, G. Hu, and C. Tang, “Rheo-cast microstructure and mechanical properties of am60 alloy produced by self-inoculation rheo-diecasting process,” *Metals*, vol. 6, no. 3, p. 69, 2016.

[97] S.-H. Kim, B.-S. You, C. D. Yim, and Y.-M. Seo, “Texture and microstructure changes in asymmetrically hot rolled {AZ31} magnesium alloy sheets,” *Materials Letters*, vol. 59, no. 29–30, pp. 3876 – 3880, 2005.

[98] M. Perez-Prado and O. Ruano, “Texture evolution during annealing of magnesium az31 alloy,” *Scripta materialia*, vol. 46, no. 2, pp. 149–155, 2002.

[99] H. T. Jeong and T. K. Ha, “Texture development in a warm rolled {AZ31} magnesium alloy,” *Journal of Materials Processing Technology*, vol. 187–188, pp. 559 – 561, 2007. 3rd International Conference on Advanced Forming and Die Manufacturing Technology.

[100] O. Kaibyshev, B. Rodionov, and R. Valiev, “Peculiarities of dislocation slip during superplastic deformation of zn-al alloys,” *Acta Metallurgica*, vol. 26, no. 12, pp. 1877–1886, 1978.

[101] H. E.O., “The deformation and ageing of mild steel: Iii discussion of results,” *Proceedings of the Physical Society. Section B*, vol. 64, no. 9, pp. 747–753, 1951. cited By 2676.

[102] N. Petch, “The cleavage strength of polycrystals,” *J. Iron Steel Inst.*, vol. 174, pp. 25–28, 1953.

[103] N. Hansen, “Hall–petch relation and boundary strengthening,” *Scripta Materialia*, vol. 51, no. 8, pp. 801–806, 2004. Viewpoint set no. 35. Metals and alloys with a structural scale from the micrometer to the atomic dimensions.

[104] G. J. Raab, R. Z. Valiev, T. C. Lowe, and Y. T. Zhu, “Continuous processing of ultrafine grained al by ecap–conform,” *Materials Science and Engineering: A*, vol. 382, no. 1, pp. 30–34, 2004.

[105] D. Hull and D. Bacon, “Chapter 9 - dislocation arrays and crystal boundaries,” in *Introduction to Dislocations (Fifth Edition)* (D. Hull and D. Bacon, eds.), pp. 171 – 204, Oxford: Butterworth-Heinemann, fifth edition ed., 2011.

[106] J. C. Li, “Petch relation and grain boundary sources,” *Transactions of the Metallurgical Society of AIME*, vol. 227, no. 1, p. 239, 1963.

[107] M. A. Meyersm and E. Ashworth, “A model for the effect of grain size on the yield stress of metals,” *Philosophical Magazine A*, vol. 46, no. 5, pp. 737–759, 1982.

[108] T. Gladman, “Precipitation hardening in metals,” *Materials science and technology*, vol. 15, no. 1, pp. 30–36, 1999.

[109] E. Orowan, “Zur kristallplastizität. iii,” *Zeitschrift für Physik*, vol. 89, no. 9-10, pp. 634–659, 1934.

[110] J. Robson, N. Stanford, and M. Barnett, “Effect of precipitate shape on slip and twinning in magnesium alloys,” *Acta materialia*, vol. 59, no. 5, pp. 1945–1956, 2011.

[111] J. Jain, W. Poole, C. Sinclair, and M. Gharghouri, “Reducing the tension–compression yield asymmetry in a mg–8al–0.5 zn alloy via precipitation,” *Scripta Materialia*, vol. 62, no. 5, pp. 301–304, 2010.

[112] B. Smola, I. Stulíková, J. Pelcová, F. von Buch, and B. L. Mordike, “Phase transformations due to isochronal annealing of mg–rare earth–sc–mn squeeze cast alloys: Dedicated to professor dr. otmar vöhringer on the occasion of his 65th birthday,” *Zeitschrift für Metallkunde*, vol. 94, no. 5, pp. 553–558, 2003.

[113] J. Nie and B. Muddle, “Characterisation of strengthening precipitate phases in a mg–y–nd alloy,” *Acta Materialia*, vol. 48, no. 8, pp. 1691–1703, 2000.

[114] X. Gao, S.-M. Zhu, B. Muddle, and J. Nie, “Precipitation-hardened mg–ca–zn alloys with superior creep resistance,” *Scripta materialia*, vol. 53, no. 12, pp. 1321–1326, 2005.

[115] C. R. Hutchinson, J.-F. Nie, and S. Gorsse, “Modeling the precipitation processes and strengthening mechanisms in a mg-al-(zn) az91 alloy,” *Metallurgical and Materials Transactions A*, vol. 36, no. 8, pp. 2093–2105, 2005.

[116] F. Czerwinski, *Magnesium injection molding*. Springer Science & Business Media, 2007.

[117] M. Regev, E. Aghion, A. Rosen, and M. Bamberger, “Creep studies of coarse-grained az91d magnesium castings,” *Materials Science and Engineering: A*, vol. 252, no. 1, pp. 6 – 16, 1998.

[118] L. Shepeleva and M. Bamberger, “Microstructure of high pressure die cast az91d modified with ca and ce,” *Materials Science and Engineering: A*, vol. 425, no. 1, pp. 312–317, 2006.

[119] J. Embury, A. Kelly, and R. Nicholson, “Strengthening methods in crystals,” *RB Nicholson and A. Kelly*, 1971.

[120] A. Chapuis and J. H. Driver, “Temperature dependency of slip and twinning in plane strain compressed magnesium single crystals,” *Acta Materialia*, vol. 59, no. 5, pp. 1986–1994, 2011.

[121] E. Kelley and W. HOSFORD, “Plane-strain compression of magnesium and magnesium alloy crystals,” *Trans Met Soc AIME*, vol. 242, no. 1, pp. 5–13, 1968.

[122] T. Obara, H. Yoshinga, and S. Morozumi, "{11-22}<1123> slip system in magnesium," *Acta Metallurgica*, vol. 21, no. 7, pp. 845–853, 1973.

[123] H.-M. Wang, Z.-H. Chen, H.-G. Yan, and Y.-K. Liu, "Heat treatment of magnesium alloys," *Jinshu Rechuli/Heat Treatment of Metals*, vol. 30, no. 11, pp. 49–54, 2005. cited By 19.

[124] D. Duly, J. Simon, and Y. Brechet, "On the competition between continuous and discontinuous precipitations in binary mg-al alloys," *Acta Metallurgica et Materialia*, vol. 43, no. 1, pp. 101 – 106, 1995.

[125] D. Porter and J. Edington, "Microanalysis and cell boundary velocity measurements for the cellular reaction in a mg-9% al alloy.," *Proc R Soc London Ser A*, vol. 358, no. 1694, pp. 335–350, 1978. cited By 5.

[126] Y. Li, Z. min Zhang, and Y. Xue, "Influence of aging on microstructure and mechanical properties of az80 and zk60 magnesium alloys," *Transactions of Nonferrous Metals Society of China*, vol. 21, no. 4, pp. 739 – 744, 2011.

[127] X. Liu, R. Chen, and E. Han, "Effects of ageing treatment on microstructures and properties of mg–gd–y–zr alloys with and without zn additions," *Journal of Alloys and Compounds*, vol. 465, no. 1, pp. 232–238, 2008.

[128] H. Liu, Y. Chen, Y. Tang, S. Wei, and G. Niu, "The microstructure, tensile properties, and creep behavior of as-cast mg–(1–10)% sn alloys," *Journal of Alloys and Compounds*, vol. 440, no. 1, pp. 122–126, 2007.

[129] S. Fatemi-Varzaneh, A. Zarei-Hanzaki, and M. Haghshenas, "A study on the effect of thermo-mechanical parameters on the deformation behavior of mg–3al–1zn," *Materials Science and Engineering: A*, vol. 497, no. 1, pp. 438–444, 2008.

[130] H. Abedi, A. Zarei-Hanzaki, S. Fatemi-Varzaneh, and A. A. Roostaei, "The semi-solid tensile deformation behavior of wrought az31 magnesium alloy," *Materials & Design*, vol. 31, no. 9, pp. 4386–4391, 2010.

[131] N. Hort, Y.-d. Huang, and K. U. Kainer, "Intermetallics in magnesium alloys," *Advanced Engineering Materials*, vol. 8, no. 4, pp. 235–240, 2006.

[132] N. R. Kumar, J. Blandin, C. Desrayaud, F. Montheillet, and M. Suéry, "Grain refinement in az91 magnesium alloy during thermomechanical processing," *Materials Science and Engineering: A*, vol. 359, no. 1, pp. 150–157, 2003.

[133] Z. Yang, Y. Guo, J. Li, F. He, F. Xia, and M. Liang, "Plastic deformation and dynamic recrystallization behaviors of mg–5gd–4y–0.5 zn–0.5 zr alloy," *Materials Science and Engineering: A*, vol. 485, no. 1, pp. 487–491, 2008.

[134] R. Cottam, J. Robson, G. Lorimer, and B. Davis, "Dynamic recrystallization of mg and mg–y alloys: crystallographic texture development," *Materials Science and Engineering: A*, vol. 485, no. 1, pp. 375–382, 2008.

[135] M. Marya, L. G. Hector, R. Verma, and W. Tong, "Microstructural effects of AZ31 magnesium alloy on its tensile deformation and failure behaviors," *Materials Science and Engineering A*, vol. 418, no. 1-2, pp. 341–356, 2006.

[136] H. Chao, H. Sun, W. Chen, and E. Wang, "Static recrystallization kinetics of a heavily cold drawn az31 magnesium alloy under annealing treatment," *Materials Characterization*, vol. 62, no. 3, pp. 312–320, 2011.

[137] L. Li, T.-m. Liu, Y. Liu, S. He, and C.-y. Sun, "Recrystallization kinetics of cold compressed az31 magnesium alloy [j]," *Materials for Mechanical Engineering*, vol. 11, p. 004, 2008.

[138] X.-y. YANG and Z.-y. SUN, "Static recrystallization of magnesium alloy az31 after severe deformation," *The Chinese Journal of Nonferrous Metals*, vol. 8, p. 003, 2009.

[139] H. McQueen and D. Bourell, "Hot workability of metals and alloys," *JOM*, vol. 39, no. 9, pp. 28–35, 1987.

[140] H. J. McQueen and D. L. Bourell, "Hot workability of metals and alloys," *JOM*, vol. 39, no. 9, pp. 28–35, 2012.

[141] S. S. Vagarali and T. G. Langdon, "Deformation mechanisms in hcp metals at elevated temperatures—i. creep behavior of magnesium," *Acta Metallurgica*, vol. 29, no. 12, pp. 1969–1982, 1981.

[142] S. Liang, Z. Liu, and E. Wang, "Microstructure and mechanical properties of mg–al–zn alloy sheet fabricated by cold extrusion," *Materials Letters*, vol. 62, no. 24, pp. 4009–4011, 2008.

[143] N. Stanford and M. R. Barnett, "Fine grained az31 produced by conventional thermomechanical processing," *Journal of alloys and compounds*, vol. 466, no. 1, pp. 182–188, 2008.

[144] E. Gutman, Y. Unigovski, M. Levkovich, Z. Koren, E. Aghion, and M. Dangur, "Influence of technological parameters of permanent mold casting and die casting on creep and strength of mg alloy az91d," *Materials Science and Engineering: A*, vol. 234, pp. 880–883, 1997.

[145] A. Kiełbus and T. Rzychoń, "The intermetallic phases in sand casting magnesium alloys for elevated temperature," in *Materials Science Forum*, vol. 690, pp. 214–217, Trans Tech Publ, 2011.

[146] S. Kleiner, O. Beffort, A. Wahlen, and P. Uggowitzer, "Microstructure and mechanical properties of squeeze cast and semi-solid cast mg–al alloys," *Journal of Light Metals*, vol. 2, no. 4, pp. 277–280, 2002.

[147] H. Watari, K. Davey, M. Rasgado, T. Haga, and S. Izawa, "Semi-solid manufacturing process of magnesium alloys by twin-roll casting," *Journal of Materials Processing Technology*, vol. 155, pp. 1662–1667, 2004.

[148] Y. Zuo, B. Jiang, Y. Zhang, and Z. Fan, "Grain refinement of dc cast magnesium alloys with intensive melt shearing," in *IOP Conference Series: Materials Science and Engineering*, vol. 27, p. 012043, IOP Publishing, 2012.

[149] K. Hu, A. Phillion, D. Maijer, and S. Cockcroft, "Constitutive behavior of as-cast magnesium alloy mgal3zn1 in the semi-solid state," *Scripta Materialia*, vol. 60, no. 6, pp. 427 – 430, 2009.

[150] H. Watari, R. Paisarn, T. Haga, K. Noda, K. Davey, and N. Koga, "Development of manufacturing process of wrought magnesium alloy sheets by twin roll casting," *Journal of Achievements in Materials and Manufacturing Engineering*, vol. Vol. 20, nr 1-2, pp. 515–518, 2007.

[151] G. Kurz, J. Bohlen, L. Stutz, D. Letzig, and K. Kainer, *Influence of Temperature and Rolling Speed on Twin Roll Cast Strip*, pp. 363–370. John Wiley & Sons, Inc., 2013.

[152] M. Yun, S. Lokyer, and J. Hunt, "Twin roll casting of aluminium alloys," *Materials Science and Engineering: A*, vol. 280, no. 1, pp. 116–123, 2000.

[153] C. Gras, M. Meredith, and J. Hunt, "Microdefects formation during the twin-roll casting of al–mg–mn aluminium alloys," *Journal of Materials Processing Technology*, vol. 167, no. 1, pp. 62–72, 2005.

[154] T. Mizoguchi and K.-i. Miyazawa, “Formation of solidification structure in twin roll casting process of 18cr-8ni stainless steel,” *ISIJ international*, vol. 35, no. 6, pp. 771–777, 1995.

[155] R. Tavares, M. Isac, and R. Guthrie, “Roll-strip interfacial heat fluxes in twin-roll casting of low-carbon steels and their effects on strip microstructure.,” *ISIJ international*, vol. 38, no. 12, pp. 1353–1361, 1998.

[156] Y. Nakaura and K. Ohori, “Properties of az31 magnesium alloy sheet produced by twin roll casting,” in *Materials Science Forum*, vol. 488, pp. 419–426, Trans Tech Publ, 2005.

[157] M. Zimina, P. Málek, J. Bohlen, D. Letzig, G. Kurz, and M. Cieslar, “Mechanical properties of homogenized twin-roll cast and conventionally cast az31 magnesium alloys,” *Materiálové Inzinierstvo*, vol. 22, no. 1, p. 8, 2015.

[158] M. J. Zehetbauer and Y. T. Zhu, *Bulk nanostructured materials.* John Wiley & Sons, 2009.

[159] K. Nakashima, Z. Horita, M. Nemoto, and T. G. Langdon, “Development of a multi-pass facility for equal-channel angular pressing to high total strains,” *Materials Science and Engineering: A*, vol. 281, no. 1, pp. 82–87, 2000.

[160] W. Kim, S. Hong, Y. Kim, S. Min, H. Jeong, and J. Lee, “Texture development and its effect on mechanical properties of an az61 mg alloy fabricated by equal channel angular pressing,” *Acta Materialia*, vol. 51, no. 11, pp. 3293 – 3307, 2003.

[161] S. Agnew, J. Horton, T. Lillo, and D. Brown, “Enhanced ductility in strongly textured magnesium produced by equal channel angular processing,” *Scripta Materialia*, vol. 50, no. 3, pp. 377 – 381, 2004.

[162] Y. Yoshida, L. Cisar, S. Kamado, and Y. Kojima, “Effect of microstructural factors on tensile properties of an ecae-processed az31 magnesium alloy,” *Materials Transactions*, vol. 44, no. 4, pp. 468–475, 2003.

[163] T. Mukai, M. Yamanoi, H. Watanabe, and K. Higashi, “Ductility enhancement in az31 magnesium alloy by controlling its grain structure,” *Scripta Materialia*, vol. 45, pp. 89–94, 2001.

[164] K. Matsubara, Y. Miyahara, Z. Horita, and T. G. Langdon, “Achieving enhanced ductility in a dilute magnesium alloy through severe plastic deformation,” *Metallurgical and Materials Transactions A*, vol. 35, no. 6, pp. 1735–1744, 2004.

[165] M. Eddahbi, J. Del Valle, M. T. Pérez-Prado, and O. A. Ruano, “Comparison of the microstructure and thermal stability of an az31 alloy processed by ecap and large strain hot rolling,” *Materials Science and Engineering: A*, vol. 410, pp. 308–311, 2005.

[166] M. Al-Maharbi, I. Karaman, I. J. Beyerlein, D. Foley, K. T. Hartwig, L. J. Kecskes, and S. N. Mathaudhu, “Microstructure, crystallographic texture, and plastic anisotropy evolution in an mg alloy during equal channel angular extrusion processing,” *Materials Science and Engineering: A*, vol. 528, no. 25, pp. 7616–7627, 2011.

[167] R. B. Figueiredo and T. G. Langdon, “Principles of grain refinement and superplastic flow in magnesium alloys processed by {ECAP},” *Materials Science and Engineering: A*, vol. 501, no. 1–2, pp. 105 – 114, 2009.

[168] K. Máthis, J. Gubicza, and N. Nam, “Microstructure and mechanical behavior of az91 mg alloy processed by equal channel angular pressing,” *Journal of Alloys and Compounds*, vol. 394, no. 1, pp. 194–199, 2005.

[169] M. Kai, Z. Horita, and T. G. Langdon, “Developing grain refinement and superplasticity in a magnesium alloy processed by high-pressure torsion,” *Materials Science and Engineering: A*, vol. 488, no. 1, pp. 117–124, 2008.

[170] Y. Harai, M. Kai, K. Kaneko, Z. Horita, and T. G. Langdon, “Microstructural and mechanical characteristics of az61 magnesium alloy processed by high-pressure torsion,” *Materials transactions*, vol. 49, no. 1, pp. 76–83, 2008.

[171] Y. Saito, N. Tsuji, H. Utsunomiya, T. Sakai, and R. Hong, “Ultra-fine grained bulk aluminum produced by accumulative roll-bonding (arb) process,” *Scripta materialia*, vol. 39, no. 9, pp. 1221–1227, 1998.

[172] Y. Saito, H. Utsunomiya, N. Tsuji, and T. Sakai, “Novel ultra-high straining process for bulk materials—development of the accumulative roll-bonding (arb) process,” *Acta materialia*, vol. 47, no. 2, pp. 579–583, 1999.

[173] X. Huang, N. Tsuji, N. Hansen, and Y. Minamino, “Microstructural evolution during accumulative roll-bonding of commercial purity aluminum,” *Materials Science and Engineering: A*, vol. 340, no. 1, pp. 265–271, 2003.

[174] J. Huang, Y. T. Zhu, D. J. Alexander, X. Liao, T. C. Lowe, and R. J. Asaro, “Development of repetitive corrugation and straightening,” *Materials Science and Engineering: A*, vol. 371, no. 1, pp. 35–39, 2004.

[175] Y. T. Zhu, H. Jiang, J. Huang, and T. C. Lowe, “A new route to bulk nanostructured metals,” *Metallurgical and materials transactions A*, vol. 32, no. 6, pp. 1559–1562, 2001.

[176] D. H. Shin, J.-J. Park, Y.-S. Kim, and K.-T. Park, “Constrained groove pressing and its application to grain refinement of aluminum,” *Materials Science and Engineering: A*, vol. 328, no. 1–2, pp. 98 – 103, 2002.

[177] J. Lee and J. Park, “Numerical and experimental investigations of constrained groove pressing and rolling for grain refinement,” *Journal of Materials Processing Technology*, vol. 130, pp. 208–213, 2002.

[178] M. Shantharaja, “Mechanical behaviour of pure aluminum processed by constrained groove pressing,” *Journal of Material Sciences & Engineering*, vol. 2013, 2013.

[179] F. Khakbaz and M. Kazeminezhad, “Work hardening and mechanical properties of severely deformed aa3003 by constrained groove pressing,” *Journal of Manufacturing Processes*, vol. 14, no. 1, pp. 20–25, 2012.

[180] J. Zrnik, T. Kovarik, Z. Novy, and M. Cieslar, “Ultrafine-grained structure development and deformation behavior of aluminium processed by constrained groove pressing,” *Materials Science and Engineering: A*, vol. 503, no. 1–2, pp. 126 – 129, 2009. International Symposium on Bulk Nanostructured Materials: from Fundamentals to Innovation, {BNM} 2007.

[181] A. Krishnaiah, U. Chakkingal, and P. Venugopal, “Applicability of the groove pressing technique for grain refinement in commercial purity copper,” *Materials Science and Engineering: A*, vol. 410, pp. 337–340, 2005.

[182] F. Khodabakhshi and M. Kazeminezhad, “The effect of constrained groove pressing on grain size, dislocation density and electrical resistivity of low carbon steel,” *Materials & Design*, vol. 32, no. 6, pp. 3280 – 3286, 2011.

[183] F. Khodabakhshi, M. Kazeminezhad, and A. Kokabi, “Constrained groove pressing of low carbon steel: nano-structure and mechanical properties,” *Materials Science and Engineering: A*, vol. 527, no. 16, pp. 4043–4049, 2010.

[184] A. Thirugnanam, T. S. Kumar, and U. Chakkingal, “Tailoring the bioactivity of commercially pure titanium by grain refinement using groove pressing,” *Materials Science and Engineering: C*, vol. 30, no. 1, pp. 203–208, 2010.

[185] B. R. Sunil, A. A. Kumar, T. S. Kumar, and U. Chakkingal, "Role of biomineralization on the degradation of fine grained az31 magnesium alloy processed by groove pressing," *Materials Science and Engineering: C*, vol. 33, no. 3, pp. 1607 – 1615, 2013.

[186] G. G. Niranjan and U. Chakkingal, "Deep drawability of commercial purity aluminum sheets processed by groove pressing," *Journal of Materials Processing Technology*, vol. 210, no. 11, pp. 1511–1516, 2010.

[187] P. Apps, M. Berta, and P. Prangnell, "The effect of dispersoids on the grain refinement mechanisms during deformation of aluminium alloys to ultra-high strains," *Acta materialia*, vol. 53, no. 2, pp. 499–511, 2005.

[188] HyperPhysics, "Band theory of solids," 2016.

[189] Wikipedia, "Electrical resistivity and conductivity — wikipedia, the free encyclopedia," 2016.

[190] M. Hájek, J. Veselý, and M. Cieslar, "Precision of electrical resistivity measurements," *Materials Science and Engineering: A*, vol. 462, no. 1–2, pp. 339 – 342, 2007. International Symposium on Physics of Materials, 2005.

[191] A. J. Schwartz, M. Kumar, B. L. Adams, and D. P. Field, *Electron backscatter diffraction in materials science*, vol. 2. Springer, 2009.

[192] W. Mai, 2016.

[193] E. N. Landis and D. T. Keane, "X-ray microtomography," *Materials characterization*, vol. 61, no. 12, pp. 1305–1316, 2010.

[194] S. R. Stock, *Microcomputed tomography: methodology and applications*. Crc Press, 2008.

[195] H. Dunsmuir, P. B. Vandiver, R. Chlanelll, H. Deckman, and J. Hardenbergh, "X-ray microtomography of ceramic artifacts," in *MRS Proceedings*, vol. 352, p. 73, Cambridge Univ Press, 1995.

[196] F. Buyens, S. Legoupil, and A. Vabre, "Metallic foams characterization using x-ray microtomography,"

[197] H. Rashed, J. Robson, P. Bate, and B. Davis, "Application of x-ray microtomography to analysis of cavitation in az61 magnesium alloy during hot deformation," *Materials Science and Engineering: A*, vol. 528, no. 6, pp. 2610–2619, 2011.

[198] V. Kovalevski, "Herman, gt, image reconstruction from projections. the fundamentals of computerized tomography. new york-london, academic press 1980. xii, 316 s. isbn 0-12-342050-4," *ZAMM-Journal of Applied Mathematics and Mechanics Zeitschrift für Angewandte Mathematik und Mechanik*, vol. 63, no. 2, pp. 141–142, 1983.

[199] J. Kastner, S. Zaunschirm, S. Baumgartner, G. Requena, H. Pinto, and G. Garces, "3d-microstructure characterization of thermomecanically treated mg-alloys by high resolution x-ray computed tomography," *Proceedings ECNDT, Prague*, 2014.

[200] D. Kopeliovich, "Hardness test methods," 2014.

[201] E. Pavlina and C. Van Tyne, "Correlation of yield strength and tensile strength with hardness for steels," *Journal of Materials Engineering and Performance*, vol. 17, no. 6, pp. 888–893, 2008.

[202] K.-m. Braszczynska, "Precipitates of γ –Mg17Al12 Phase in AZ91 Alloy," *Magnesium Alloys - Design, Processing and Properties*, pp. 95–112, 2011.

[203] L. Wang and H. Liu, “The microstructural evolution of al12mg17 alloy during the quenching processes,” *Journal of Non-Crystalline Solids*, vol. 352, no. 26–27, pp. 2880 – 2884, 2006.

[204] Y. Birol, “Analysis of macro segregation in twin-roll cast aluminium strips via solidification curves,” *Journal of Alloys and Compounds*, vol. 486, no. 1, pp. 168–172, 2009.

[205] R. Blanc and M. Belzons, “Resistance studies of low-temperature deposited alloy-films of mg-fe,” *Solid State Communications*, vol. 27, no. 11, pp. 1137–1139, 1978.

[206] G. T. Meaden, *Electrical resistance of metals*. Springer, 2013.

[207] T. Ying, H. Chi, M. Zheng, Z. Li, and C. Uher, “Low-temperature electrical resistivity and thermal conductivity of binary magnesium alloys,” *Acta Materialia*, vol. 80, pp. 288 – 295, 2014.

[208] M. Asgar-Khan and M. Medraj, “Thermodynamic description of the mg-mn, al-mn and mg-al-mn systems using the modified quasichemical model for the liquid phases,” *Materials transactions*, vol. 50, no. 5, pp. 1113–1122, 2009.

[209] Y. Ren, G. Qin, W. Pei, H. Zhao, Y. Guo, H. Li, M. Jiang, and S. Hao, “Isothermal section of the mg–al–mn ternary system at 400° c,” *Journal of Alloys and Compounds*, vol. 479, no. 1, pp. 237–241, 2009.

[210] J. Hay and P. Agee, “Mapping the mechanical properties of alloyed magnesium (AZ 61),” *Conference Proceedings of the Society for Experimental Mechanics Series*, vol. 5, no. Az 61, pp. 97–101, 2014.

[211] M. Cieslar and M. Poková, “Annealing effects in twin-roll cast aa8006 aluminium sheets processed by accumulative roll-bonding,” *Materials*, vol. 7, no. 12, pp. 8058–8069, 2014.

[212] X. Huang, N. Hansen, and N. Tsuji, “Hardening by annealing and softening by deformation in nanostructured metals,” *Science*, vol. 312, no. 5771, pp. 249–251, 2006.

[213] M. Avrami, “Kinetics of phase change. i general theory,” *The Journal of Chemical Physics*, vol. 7, no. 12, pp. 1103–1112, 1939.

[214] A. Levinson, R. K. Mishra, R. D. Doherty, and S. R. Kalidindi, “Influence of deformation twinning on static annealing of az31 mg alloy,” *Acta Materialia*, vol. 61, no. 16, pp. 5966–5978, 2013.

[215] J. Su, M. Sanjari, A. S. H. Kabir, J. J. Jonas, and S. Yue, “Static recrystallization behavior of magnesium az31 alloy subjected to high speed rolling,” *Materials Science and Engineering: A*, vol. 662, pp. 412–425, 2016.

[216] G. Zhou, M. K. Jain, P. Wu, Y. Shao, D. Li, and Y. Peng, “Experiment and crystal plasticity analysis on plastic deformation of az31b mg alloy sheet under intermediate temperatures: How deformation mechanisms evolve,” *International Journal of Plasticity*, vol. 79, pp. 19–47, 2016.

[217] E. Voce, “A practical strain-hardening function,” *Metallurgia*, vol. 51, no. 307, pp. 219–226, 1955.

[218] U. Kocks, “Laws for work-hardening and low-temperature creep,” *Journal of engineering materials and technology*, vol. 98, no. 1, pp. 76–85, 1976.

[219] G. Sainath, B. Choudhary, J. Christopher, E. I. Samuel, and M. Mathew, “Applicability of voce equation for tensile flow and work hardening behaviour of p92 ferritic steel,” *International Journal of Pressure Vessels and Piping*, vol. 132, pp. 1–9, 2015.

[220] R. B. Figueiredo and T. G. Langdon, “Grain refinement and mechanical behavior of a magnesium alloy processed by ECAP,” *Journal of Materials Science*, vol. 45, no. 17, pp. 4827–4836, 2010.

[221] M. Barnett, “A taylor model based description of the proof stress of magnesium az31 during hot working,” *Metallurgical and materials transactions A*, vol. 34, no. 9, pp. 1799–1806, 2003.

[222] X. Feng and T. Ai, “Microstructure evolution and mechanical behavior of az31 mg alloy processed by equal-channel angular pressing,” *Transactions of Nonferrous Metals Society of China*, vol. 19, no. 2, pp. 293 – 298, 2009.

[223] A. Muralidhar, S. Narendranath, and H. S. Nayaka, “Effect of equal channel angular pressing on az31 wrought magnesium alloys,” *Journal of Magnesium and Alloys*, vol. 1, no. 4, pp. 336–340, 2013.

[224] Q. Miao, L.-X. Hu, H.-F. Sun, and E.-D. Wang, “Grain refining and property improvement of az31 mg alloy by hot rolling,” *Transactions of Nonferrous Metals Society of China*, vol. 19, no. Supplement 2, pp. s326–s330, 2009.

[225] R. B. Figueiredo and T. G. Langdon, “Principles of grain refinement and superplastic flow in magnesium alloys processed by ecap,” *Materials Science and Engineering: A*, vol. 501, no. 1, pp. 105–114, 2009.

List of Figures

1.1 Slip and twinning systems in magnesium [22]. 6
1.2 Nominal chemical composition of certain important cast magnesium alloys [34]. 8
1.3 Phase diagrams of (a) Mg-Al [48] and (b) Mg-Zn systems [49]. . . 10
1.4 Optical micrographs of a) an oxide cluster in AZ91 alloy, b) a "snaky" oxide in AM50 alloy [75] and c) SEM image of hot tearing in AM60 alloy produced by liquid die casting [96]. 14
1.5 The $(10\bar{1}0)$, (0002), $(10\bar{1}1)$ and $(10\bar{1}2)$ pole figures of AZ31 magnesium alloy sheets produced by a) hot rolling and b)18 %, c) 30 %, d) 50 % warm rolling [99]. 15
1.6 Illustration of twin-roll casting process [151]: a) twin-roll caster and b) scheme of the twin-roll casting process. 21
1.7 Schematic illustration of equal-channel angular pressing [158]. . . 22
1.8 Illustration of possible equal-channel angular pressing routes [159]. 22
1.9 Illustration of constrained groove pressing process: a) grooved die, b) groove pressing, c) flat pressing, d) the specimen is rotated by 180° along the pressing direction and (e) the groove pressing stage is repeated, (f) specimen is flattened again [186]. 24

3.1 Picture of the AZ31 AC ingot of the master alloy and strip produced by TRC. 26
3.2 Illustration of the H-shape sample used for resistivity measurements. 28
3.3 Heterogeneous distribution of grain sizes in AZ31 magnesium alloy after CGP evaluated using the equivalent diameter method via NIS-lements AR 3.0 software. 29
3.4 Illustration of an operating scheme of atomic force microscope [192]. 32
3.5 Illustration of X-ray diffraction measurements using Shultz reflection method. 33
3.6 Schematic illustration of X-ray CT acquisition and reconstruction processes. The 3D map is typically presented as a series of 2D slice images [193]. 33
3.7 Illustration of the Vickers hardness method [200]. 34
3.8 Dog-bone shaped specimen for tensile tests. 35
3.9 Illustration of the sample orientation during ECAP. 36
3.10 Illustration of the constrained groove pressing facility: a) pressing machine, b)grooves, c), d) geometry of the die and grooves. 37
3.11 TRC samples subjected to 1/4 of CGP cycle, an arrow indicates the RD of the strip. 37

4.1 LOM image of the as-cast ingot of master AZ31 Mg alloy. 38
4.2 Light optical microscopy imaging of cross-sections of TRC strip in a) TD, b) RD and c) the surface of twin-roll cast AZ31 Mg alloy in ND. 39
4.3 Light optical microscopy images of indicated parts of TRC AZ31 magnesium strip in a-c) TD and d-e) in RD. 39

4.4 Micrographs of the TRC alloy showing the distribution of primary particles along the strip in a) RD, b) TD and c) ND. 40
4.5 Back scatter electron images of the central region of the TRC strip in a) TD, b) RD and c) ND. 41
4.6 SEM images of the central region of the as-cast AZ31 magnesium alloy: a), b) BSE image of a "deer-shaped" segregation in the center of the strip, c) BSE imaging of dendrite arms and Al-Mn intermetallic particles, d), e) SE maps of Al and Mn collected from the region from Fig. d). 41
4.7 X-Ray microtomography 3D reconstructed patterns of central segregation in TRC AZ31 magnesium alloy in different perspectives: a) RD, b) TD, c) ND and d) general view. Scale is represented in millimeters. 43
4.8 EBSD map (a) and 0001 and $10\bar{1}0$ pole figures of TRC strip (b) (schematic drawing shows a prevailing crystal orientation). 44
4.9 EBSD orientation maps and 0001 and $10\bar{1}0$ pole figures of the selected regions of TRC strip: a) 1 - upper part of the bulk of the sample, b) 3 - lower part of the bulk, c) 2 - center of the strip in the TRC alloy (schematic drawing shows a prevailing crystal orientation). 44
4.10 Vickers microardness maps of a) AC and b) TRC alloys. 45
4.11 Evolution of resistivity during step-by-step annealing. 46
4.12 Evolution of the microstructure of AC AZ31 magnesium alloy during annealing up to: a) 250 °C, b) 350 °C, c), f) 400 °C, d), g) 450 °C for 10 h and e) cross-section of AC alloy before annealing. . . . 47
4.13 LOM micrographs of the bulk region of the TRC AZ31 strip in TD during annealing up to: a) 100 °C, b) 250 °C, c) 300 °C d) 350 °C, e) 400 °C, f) 450 °C for 10 h. 48
4.14 Cross-section of the TRC AZ31 strip in TD during annealing up to: a) 100 °C, b) 250 °C, c) 300 °C d) 350 °C, e) 400 °C, f) 450 °C for 10 h. 49
4.15 Thermal stability of the TRC alloy annealed at 450 °C: a) 10 min, b) 80 min, c) 160 min, d) 6 h and e) 24 h. 50
4.16 Microstructure of TRC alloy aged at: a) 300 °C for 7 days and b) 500 °C for 40 min. 51
4.17 Evolution of the microstructure of TRC AZ31 magnesium alloy strip in TD during annealing observed using back scatter electron imaging: a) as-cast, b) 250 °C, c) 300 °C d) 350 °C, e)400 °C, f) 450 °C for 10 h. 52
4.18 EBSD map (a) and 0001 and $10\bar{1}0$ pole figures (b) of TRC strip annealed at 450 °C for 10 h (schematic drawing shows a prevailing crystal orientation). 53
4.19 0001 and $10\bar{1}0$ PF of the bulk area of AZ31 TRC strip measured by XRD in: a) as-cast and b) homogenized states. 54
4.20 Microhardness mapping of AC AZ31 Mg alloy a) before and b) after aging at 450 °C for 10 h. 54
4.21 Microhardness mapping of TRC AZ31 Mg alloy after annealing at: a) 100 °C, b) 250 °C, c) 300 °C, d) 350 °C and e) 400 °C. 55

4.22 Distribution of microhardness of TRC alloy during annealing. . . 55
4.23 Distribution of microhardness of TRC alloy during aging at 450 °C for: a) 10 min, b) 80 min, c) 160 min, d) 6 h, e) 10 h and f) 24 h. 56
4.24 Vickers microhardness of TRC samples after annealing at a) 300 °C for 7 days and b) at 500 °C for 40 min. 56
4.25 Stress-strain curves of AC AZ31 specimens strained at temperature range from RT to 300 °C: a) as-cast AC samples and b) AC samples after homogenization annealing at 450 °C for 10 hours. 57
4.26 Stress-strain curves for TRC AZ31 magnesium alloys during straining at temperature range from RT to 300 °C: a) as-cast in RD, b) after homogenization annealing at 450 °C for 10 hours in RD, c) as-cast in TD, d) after homogenization in TD. 58
4.27 Temperature dependence of the elongation of AC and TRC magnesium alloys during straining at temperature range from RT to 300 °C. 59
4.28 Temperature dependence of the yield stress and ultimate tensile strength of AZ31 magnesium alloy during straining at temperature range from RT to 300 °C tested in RD and TD. 59
4.29 LOM images after tensile tests of TRC specimens deformed in RD at: a,b) 100 °C, c, d) 200 °C and e, f) 300 °C. 61
4.30 LOM images after tensile tests of TRC specimens deformed in TD at: a,b) 100 °C, c, d) 200 °C and e, f) 300 °C. 62
4.31 Sequence of images obtained from a video record during tensile tests performed in RD and TD at 100, 200 and 300 °C. 63
4.32 Orientation maps and PF of TRC samples after tensile tests deformed in RD at a) 100 °C, b), d) 200 °C and c) 300 °C. 64
4.33 SEM channeling contrast images after tensile tests of homogenized TRC specimens deformed in RD at a) 100 °C, b) 200 °C and c) 300 °C. 65
4.34 AFM images of the selected areas of TRC strip specimens after tensile tests performed in RD at: a) 100 °C, b-d) 200 °C and e) 300 °C. Arrows indicate glide planes of the most active slip systems. 66
4.35 AFM images of the selected areas of TRC strip specimens after tensile tests performed in TD at: a) 100 °C, b) 200 °C and c) 300 °C. 66
4.36 EBSD maps of AC samples after 0, 2, 4 and 8 ECAP passes. . . . 67
4.37 EBSD maps of TRC samples processed by ECAP in RD: a) as-cast, b) sample homogenized at 450 °C for 10 h. 69
4.38 EBSD maps of TRC samples processed by ECAP in TD: a) as-cast, b) sample homogenized at 450 °C for 10 h.. 70
4.39 Pole figures of AC samples before ECAP and after 2, 4 and 8 ECAP passes. 71
4.40 Pole figures of the TRC strip processed by 1, 2, 4 and 8 ECAP passes in RD: a) as-cast sample, b) sample homogenized at 450 °C for 10 h. 72
4.41 Pole figures of the TRC strip processed by 1, 2, 4 and 8 ECAP passes in TD: a) as-cast sample, b) sample homogenized at 450 °C for 10 h. 73

4.42 Microstructure of the TRC strip processed in TD using ECAP: a) homogenized and after 1P aged at 450 °C for 5 h, b) homogenized and after 8P aged at 450 °C for 5 h, c) as-cast and after 1P aged at 450 °C for 5 h, d) as-cast and after 8P aged at 450 °C for 5 h and e) as-cast and after 1P aged at 450 °C for 10 h. 74
4.43 PF of TRC strip ECAP process in TD and aged at 450 °C for 5 h and 10 h. 75
4.44 The dependence of the HV0.1 microhardness of AC and TRC samples processed by ECAP on a) the number of ECAP passes and b) additional annealing time. 76
4.45 Microstructure images of the cross-section of the twin-roll cast strip after one cycle of constrained groove pressing: a) cross-section imaging at 50x, b) the most deformed zone, c) transition "bimodal" zone and d) bulk. 77
4.46 Microstructure of the AZ31 twin-roll cast strip after one CGP cycle and annealing at 250, 350, 400 °C and aging for 10 h at 450 °C: a) the most deformed zone, b) transition "bimodal" zone and c) bulk. 78
4.47 Microstructure of the TRC strip after one CGP cycle and aging at 450 °C for: a) 10 h and b) 30 h. 79
4.48 EBSD orientation maps of the cross-section of the TRC strip after one CGP cycle: a) without aging and aged at 450 °C for: b) 10 h and c) 30 h. 80
4.49 Texture evolution of the TRC strip after one CGP cycle: a) as-deformed state and after aging at 450 °C for: b) 10 h and c) 30 h. 81
4.50 Microhardness the AZ31 TRC strip after one CGP cycle in a relation with the microstructure of the cross-section of the sample and a die geometry (black lines). 81
4.51 Microhardness maps of the TRC strip after a) one CGP cycle and annealing at: b) 250 °C, c) 350 °C and d) 400 °C. 82
4.52 Plot summarizing the distribution of microhardness values along the TRC strip in RD processed by one CGP cycle and annealing at 250, 300, 350 and 400 °C. 82
4.53 Microhardness evolution of the AZ31 TRC strip after one cycle of constrained groove pressing: a) without aging, aging at 450 °C for: b) 10 h and c) 30 h; d) plot summarizing the distribution of HV0.1 values along the strip in RD. 83
4.54 Stress-strain curves of CGP samples at indicated deformation temperatures. 83
4.55 Microstructure of the TRC sample after one CGP cycle and tensile tests held at a) RT, b) 100 °C, c) 200 °C and d) 300 °C. 84

5.1 Avrami analysis of recrystallization processes occurring in the TRC strip during annealing at 450 °C. 89
5.2 Avrami analysis of recrystallization processes occurring in the TRC strip during annealing at 450 °C calculated from microhardness measurements. 89
5.3 Illustration of a work hardening rate (Θ) evaluation procedure. . . 91

5.4 Temperature dependence of a work hardening coefficient for studied alloys. 92
5.5 Microhardness of TRC alloy after ECAP processing. 94
5.6 Hall-Petch relation curves applied on AZ31. 94
5.7 KAM maps of a selected bulk area of a) the TRC sample and b) the TRC strip after eight ECAP passes. 95
5.8 "Necklace" bands of finer grains in CGP plate after tensile test at 200 °C. 98

List of Tables

1.1 ASTM designation of some alloying elements (RE - rear earth). . 6
1.2 Basic heat treatment designation of magnesium alloys [5]. 7

3.1 Chemical composition of AZ31 alloy, wt.%. 26

5.1 Resistivity of individual elements contributed to the resulting resistivity of AZ31 alloy 86

List of Abbreviations

AC - as-cast
AFM - Atomic Force Microscopy
ARB - Accumulative Roll Bonding
ASTM - American Society for Testing and Materials
BSE - Back-Scattered Electrons
CGP - Constrained Groove Pressing
CLS - Center Line Segregation
CRSS - Critical Resolve Shear Stress
CT - Computed Tomography
DAS - Dendrite Arm Spacing
DC - Die Casting
DRV - Dynamic Recovery
DRX - Dynamic Recrystallization
EBSD - Electron Back Scatter Diffraction
ECAE - Equal-Channel Angular Extrusion
ECAP - Equal-Channel Angular Pressing
EDS - Energy Dispersive Spectroscopy
EDX - Energy Dispersive X-ray analysis
EN - European Standard
GBS - Grain Boundary Sliding
GP - Groove Pressing
G-P zones - Guinier-Preston zones
hcp - hexagonal close-packed
H-P - Hall-Petch
HPT - High Pressure Torsion
HV - Vickers Microhardness
KAM - Kernel Average Misorientation
LN - Liquid Nitrogen
LOM - Light Optical Microscopy
ND - Normal Direction
PF - Pole Figure
RCS - Repetitive Corrugation and Straitening
RD - Rolling Direction
RE - Rare Earth
RT - Room Temperature
SE - Secondary Electrons
SEM - Scanning Electron Microscopy
SPD - Severe Plastic Deformation
SRX - Static Recrystallization
TD - Transverse Direction
TRC - Twin-roll Casting
UFG - Ultrafine-grained
UTS - Ultimate Tensile Strength
XRD - X-ray Diffraction
YS - Yield Strength